POLITECNICO DI TORINO

Master of Science in
Aerospace Engineering

Tesi di Laurea Magistrale

Modeling and Design for the Attitude Control Phase of the LISA drag-free mission

Supervisors :

  Prof. Carlo Novara (DET)

  Dr.ssa Elisa Capello (DIMEAS)

Candidate :

    Francesco Basile

March 2019

L'universo è silenzioso qui

Summary

The Laser Interferometer Space Antenna (LISA) is a Space mission led by ESA now entering its phase A. LISA will be the first observatory in space to explore the Gravitational Universe. It will gather revolutionary information about the dark universe. The new LISA mission envisaged as a joint ESA-NASA mission to observe astrophysical and cosmological sources of low frequency gravitational waves.

The primary objective of the LISA mission is to detect and observe gravitational waves emitted from massive black holes and galactic binaries in the low-frequency band which ranges from $0.1mHz$ up to $1Hz$ with a goal of extending the measurements down to $30\mu Hz$. The underlying measurement principle is a laser interferometry system built up with three satellites that are flying in a triangular constellation with an edge length of $2.5Mkm$. These will detect low frequency gravitational waves through the measurement of changes in the length of the optical path between the two reflective proof masses of one arm of the interferometer relative to the other arm.

In order to ensure that the test masses are flying in a disturbance-free motion along their geodesics, so that an extremely small displacement due to the passage of gravitational waves is detectable, challenging performance requirements with respect to internal and external disturbance rejection must be satisfied by an overall Drag-Free-System. This provides the relatively undisturbed environment for the test-masses which form the references for the measurement of the gravitational waves. Without it the effect of gravitational waves would be not detectable.

This thesis is written in the context of the space mission Laser Interferometer Space Antenna (LISA) and its technology demonstration precursor mission LISA Pathfinder. The research carried out led to the development of a simulator and a preliminary control model of the LISA attitude control system to assess its feasibility. Technological risk assessment in general, as well as that associated with the LISA mission, is also considered.

The main focus of this thesis is the modeling and control of the drag free LISA scenario. The first part of the work brought to a set up of nonlinear equations of the overall system dynamics in order to produce a simulator for the LISA spacecraft complete dynamic. The mathematical modeling allowed to better understand the behavior of the system and the related interaction within the scope of the mission. The effects of gravitational waves on any system are incredibly small, even for a system designed to detect them. For this reason disturbance effects which could, in any other system, be disregarded, must be taken into account as they may produce unacceptable noise levels. Therefore, a fundamental part of the modeling phase has been the characterization of noises and disturbances from sensors, actuators and environment.

The second part applies a preliminary study on the control system structure needed to meet the requirements of the mission. General considerations about the modes in which the spacecraft must work are made in a control design perspective. The general study of the plants is then followed by the first controller applied on the attitude of the satellite.

The designed control system even if simple, demonstrates to meet the requirements of the phases simulated. Extensive simulations are performed to verify the effectiveness of the proposed approach.

Acknowledgements

*If you want something you've never had,
you've got to do something you've never done before.
Thomas Jefferson*

Contents

List of Tables

List of Figures

Chapter 1

Introduction

The present thesis work takes place as a part of an official project conducted by the Politecnico di Torino as prime contractor in response to ESA Invitation To Tender (ITT) *"Assessment and preliminary prototyping of a drag free control system for the L3 gravity wave observatory"*. The study aims at trade-off different control system architectures and control design methodologies to satisfy the challenging mission requirements based on drag free control system. In this context, the thesis presents some of the activities carried on in the project.

As a matter of fact, the feasibility of a drag-free satellite is the central point of the overall work. The drag free control can be considered as a new concept among the space mission. The feasibility of a drag-free satellite was first considered in the 60s and then tested in the TRIAD mission in 1972. Many activities have been led in order to test the drag free concept, but it is necessary to remark that these activities are hardly applicable for several science programme missions.

It is expected that the control system for the L3 mission will need to control several degrees of freedom with different actuators at different frequencies, yielding a tightly coupled, *Multiple-Input Multiple-Output* (MIMO) system. Even though the *LISA Pathfinder* (LPF) mission has proven some of the control system technologies required to achieve this, the architecture of the LPF *Drag-Free Attitude Control System* (DFACS) has been designed to best fit the motion equations and requirements of LPF, which are less challenging than those for L3. For this reason, an in depth theoretical investigation of the possible control system architectures and control design methodologies for L3 is required. The drag free control architecture for this mission is key for its performance and therefore an in depth trade-off at mathematical-theory level, aided by simulations shall be prototyped. This activity is proposed as a bridging phase between the activities executed for the design, development, and early operations of the control system of the LPF mission and those for L3. It will allow

to gather the results and lessons learnt from LPF project and inject this knowledge quickly into the early phases of the design and development of the control system for the L3 mission. In this perspective, has been mandatory to survey the state of the art and then firstly define the elementary equations of motion for the L3 mission. After the initial definition, has been necessary to account for the dynamics of the subsystems involved in the mission, i.e. sensors and actuators, and then enclose the disturbance sources with a focus on the sensitivity budget. Great effort was dedicated to these activities due to the delicate sensitivity of the mission. Accounting for a smaller disturbance can lead to an inadequate analysis. Moreover, a decoupling analysis has been done to study the dynamics and identify possible control system design simplifications. Different plant are involved in the study and a general assessment of the control system has been done.

1.1 Gravitational waves

Systems with very large masses, such as black hole binary systems at the centers of merging galaxies, produce *Gravitational Wave* (GW) at low frequencies. While ground observatories are very sensitive to high frequencies, they are inherently limited by natural and human-generated seismic noise. Only an advanced space observatory is capable of detecting
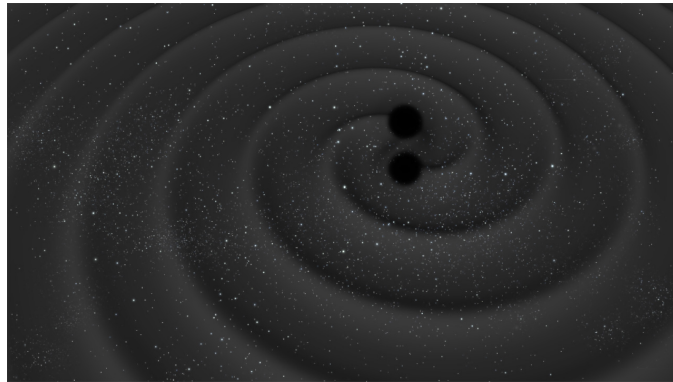
Figure 1.1. Impresion of black holes merging and fluctuations in the fabric of spacetime. Credit: ESA–C.Carreau.

gravitational waves with very low frequencies – too low to be observed above the random seismic noise, the vibrations, of the Earth. The answer is to go into space, away from such disturbances [1].
Many questions still remain about the origin and nature of gravity. Gravitational waves were first theorized by Albert Einstein [2] [3]. They are created during events such as supermassive black hole mergers, or collisions between two black holes that are billion times bigger than

our Sun. These collisions are so powerful that they create distortions in spacetime, known as gravitational waves. Gravitational waves detectable by the *Laser Interferometer Space Antenna* (LISA) mission could also come from other distant systems, including smaller stellar mass black holes orbiting supermassive black holes.

Gravitational waves are extremely difficult to detect, since they hardly interact with matter, and their presence, intensity and source can only be derived from the effects that they have on bodies around them. The first detection of the elusive gravitational waves was achieved on 4 September 2015 by the twin *Laser Interferometer Gravitational-wave Observatory* (LIGO) facilities in the United States. The LIGO scientists believe that the tiny ripples in spacetime were generated 1.3 billion light years away, when two massive black holes spiraled into each other and coalesced into a single, even more massive, spinning black hole. When these waves passed the Earth, 1.3 billion years later, they had weakened considerably: the disturbance in spacetime that LIGO measured was thousands of times smaller than an atomic nucleus [4]. Development of LISA Pathfinder began in 2004 and the *Spacecraft* (S/C) was completed over the next decade by European and US specialists. In order to test in orbit the concept of low-frequency gravitational wave measurement, the single spacecraft carried two test packages. The LISA Technology Package represented one 'arm' of the LISA interferometer, in which the separation of two *Test Mass* (TM) was reduced from $2.5Mkm$ to $35cm$ [5]. The identical test masses comprised 46 mm gold-platinum cubes, each floating in its own vacuum
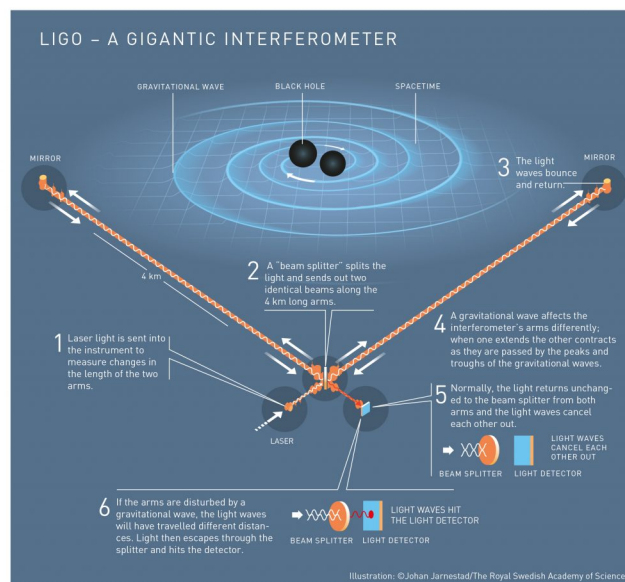
Figure 1.2.   LIGO interferometer system, Credit: Johan Jarnestad/The Royal Swedish Academy of Sciences.

container. The test masses fulfilled a double role, acting both as mirrors for the laser inter-ferometer and as inertial references for the drag-free control system. The second package was the Disturbance Reduction System, a NASA-supplied system that included two clusters of micro-propulsion thrusters and an electronic unit containing a computer with associated drag-free control software.
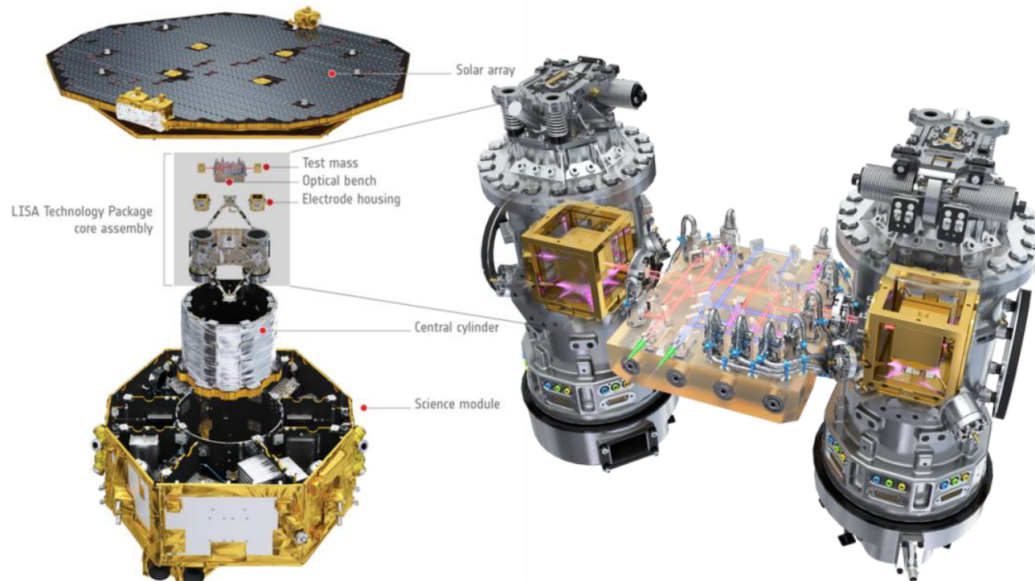
Figure 1.3.   Schematics of the LISA Technology Package (right) and its placement inside the LPF science module (left) with its μN cold gas thrusters [6].

The mission began with a launch on 3 December 2015. Over the next seven weeks, the spacecraft made its way to the L1 Lagrange Point, about 1.5 million km from Earth in the direction of the Sun. Scientific operations began in March 2016 and by June LISA Pathfinder had successfully demonstrated some of the advanced technologies required for a gravitational wave observatory in space. The results far exceeded expectations.

Figure 1.4 shows the residual relative acceleration of the two test masses on ESA's LISA Pathfinder as a function of frequency. LISA Pathfinder is a technology demonstrator mission that placed two test masses – a pair of identical, $2kg$, $46mm$ gold–platinum cubes – in the most precise freefall ever achieved, in order to test techniques to observe gravitational waves from space. The results shown are based on just two months of science operations with LISA Pathfinder. In the top central part of figure 1.4, the wedge-shaped area indicates the original requirements of LISA Pathfinder. Below it, the more stringent requirements for a future spaceborne observatory of gravitational waves are also indicated. The grey, red and
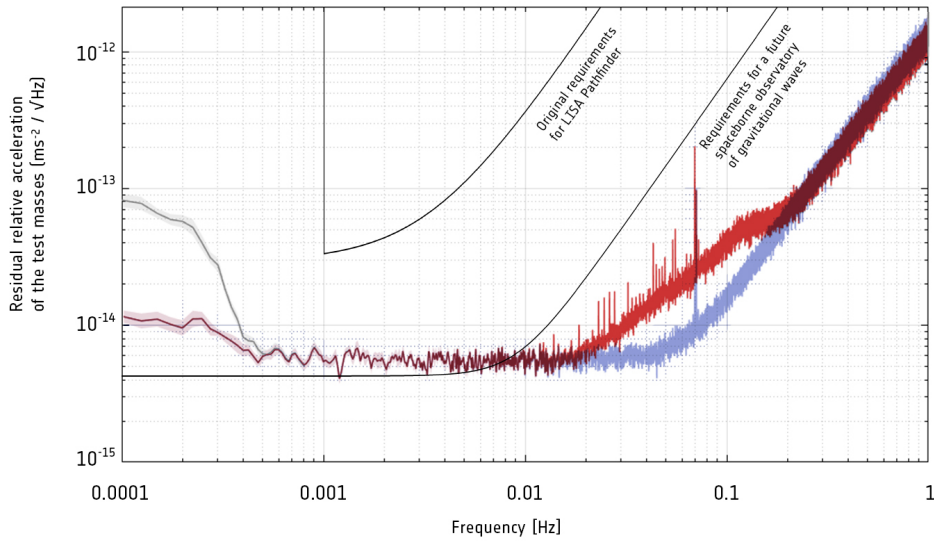
Figure 1.4.   LISA Pathfinder results. Credit: ESA/LISA Pathfinder Collaboration.

blue curves are based on the measurements performed with LISA Pathfinder, which achieved a precision more than five times better than originally required. The grey curve on the left shows the effect of a small centrifugal force acting on the cubes at the lowest frequencies probed by the experiment, below $1mHz$. This is caused by a combination of the shape of LISA Pathfinder's orbit and the effect of the noise in the signal of the star trackers that are used to orient the spacecraft. The red curve shows LISA Pathfinder's performance after the contribution of the centrifugal force has been subtracted; the source of the residual noise at low frequencies is still being investigated. At intermediate frequencies, between 1 and $60mHz$ (at the center), control over the test masses is limited by gas molecules bouncing off the cubes: a small number of them remains in the surrounding vacuum. This effect was seen to be reducing as more molecules were vented into space, and is expected to improve during the mission. At higher frequencies, between $60mHz$ and $1Hz$ (on the right), LISA Pathfinder's precision is limited only by the sensing noise of the optical metrology system used to monitor the position and orientation of the test masses. The cause of the spike around $70mHz$ is still under investigation [7]. An additional effect, visible as a bump in the red curve between $0.02Hz$ and $0.2Hz$, is caused by a tiny misalignment of the test masses in the two axes perpendicular to the direction of the laser. The blue curve, visible below the red one in this part of the graph, shows the mission's performance after this contribution has been subtracted. These results show that LISA Pathfinder has overcome its original

requirements, reaching a level of precision close to or comparable with the one required by a future gravitational-wave observatory [1].
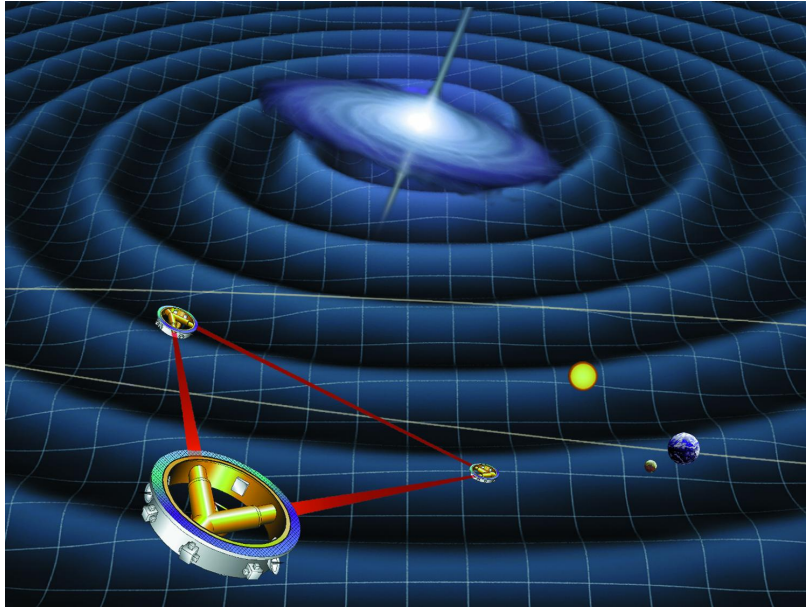
Figure 1.5.   NASA illustration of LISA.

Even before this mission was launched, ESA decided in November 2013 that the third large mission (L3) of its Cosmic Vision science programme would be an exploration of the gravitational Universe. Its launch is planned for 2034. In principle, it could be any investigation but it is most likely to be some form of gravitational wave observatory. As such, it would be sensitive to different frequencies of gravitational waves than its ground-based counterparts, and therefore would reveal different celestial events. For example, although ground-based detectors can see black holes merging, the giant ones – with masses of a million times that of the Sun – that sit at the heart of galaxies will generate gravitational waves of much lower frequency. These cannot be detected with ground-based systems because seismic interference and other sources of noise overwhelm the signals. For this reason, space-based observatories are needed. Shortly after the decision of the scientific theme for L3 was announced, ESA set up the *Gravitational Observatory Advisory Team* (GOAT). In March 2016, they released their final report into the feasibility of a LISA-like mission [8]. Their deliberations took into account the successful detection of gravitational waves from LIGO, and the first results from the LISA Pathfinder mission, which were successful.

6

1.2 Laser Interferometer Space Antenna (eLISA) project

The aspects related to the measurement of gravitational waves are more complex than the ones related to the detection of every other source in nature. "Gravitational waves are fundamentally different from electromagnetic waves." [1]. For example, it is clear that the phenomenon of electromagnetic waves belongs to the the framework of space-time. The event manifests itself in the domain without modifying it. In turn, gravitational waves are moving gravitational fields that create a time-varying strain or stretching of space-time.
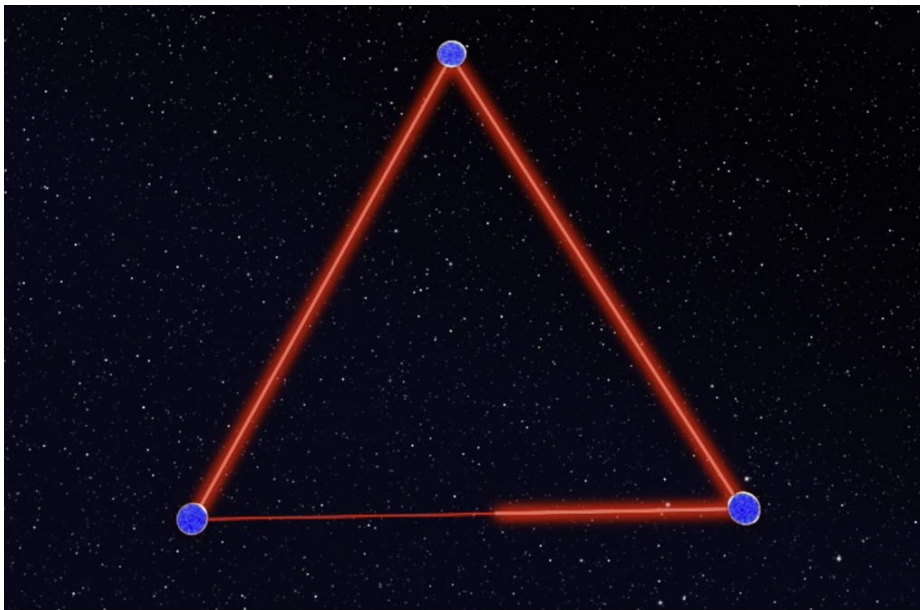
Figure 1.6. LISA formation flight: Artist's impression of LISA formation. Credit: AEI/MM/exozet.

If a gravitational wave passes in a certain region of space-time, it will create a distortion in the area that will produce the oscillation of the position of every mass. In particular, one can think to measure this tiny oscillation with respect to another mass, which will be indeed affected by the same gravitational wave.

1.2.1 Science performance

The technique that will enable the detection and the measurement of this distortion on board of the LISA sciencecraft will be an interferometry. A key point of the LISA mission is obviously the interferometric system measurement of distances on a $2.5Mkm$ path. This system, in contrast with the ones used for LIGO and LPF, presents more implications which will heavily affects the complexity of the overall mission architecture. Making use

of laser light superimposition in a certain optical path, the interferometry is used to extract information from the region. Shortly, under some circumstances two waves with the same frequency combine, the resulting intensity pattern is determined by the phase difference between the two waves. These interferometers will detect low frequency gravitational waves through measurement of changes in the length of the optical path between the two reflective test masses of one arm of the interferometer relative to the other arm. While LISA can be described as a Michelson interferometer (used in LIGO), the actual implementation is somewhat different from a classical interferometer that relies on the 'round-trip' of a beam of reflected laser light. The distances between two spacecraft is $2.5Mkm$, such a distance would require a great effort to enable the inverted reflection of the incoming beam. In other words, the laser on the receiving spacecraft is instead phase-locked to the incoming light, generating a return beam of full intensity. The distance between the two test masses is measured using heterodyne interferometry in three step measurements as showed in figure 1.7. The distances d_1 and d_2 are measured on board of each spacecraft, i.e., a local measurements between the local optical bench (OB) and the test mass. The arm distance is a measure taken between the two OBs [9].
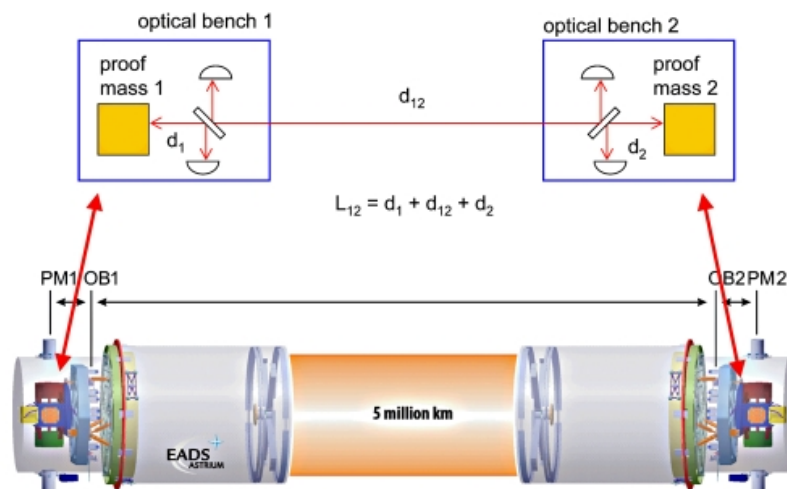
Figure 1.7. Measurement principle along one interferometer arm. The actual arm length is 2.5Mkm. Credit: EADS Astrium.

Gravitational waves cause an oscillating strain of the space-time domain, which accounts for four dimensions. The stretches and shrinks experienced by the passage of a gravitational wave on the nominal distance between the two TMs are orthogonal to the direction of

propagation of the GW and can be described as follow

$$\frac{\Delta L}{L} = \frac{h}{2}$$

where $h(t)$ is a dimensionless amplitude called "strain" and $\tilde{h}(f)$ is its frequency domain representation, ΔL is the actual displacement and L is the proper distance. This change in displacement occurs in the plane transverse to the direction of radiation, and causes a stretch along one axis and a squeeze along the orthogonal axis. This means that the bigger is the distance between two masses L, the bigger will be the amount of displacement suffered due to the GW passage ΔL on equal terms of strain. For istance, a common value of the strain h is $\sim 10^{-21}$, so if a GW with the declared strain passes between the Earth and the Sun, the distance between them would change of about $10^{-10}m$ (diameter of an hydrogen atom). LISA arm, instead, would experience a ΔL of $1.25 \cdot 10^{-12}m$.

It is the high order of the arm length that will enable a clearer measurement of the gravitational waves in the low and very low frequency band. From the single equation presented is not visible that h is not itself directly observable. A constant strain, or a strain that varies linearly with time, is exactly equivalent to starting the masses at slightly different positions, or with a slight relative velocity. Only the second and higher derivatives of the strain produce accelerations that would indicate the presence of gravitational radiation. For this reason many requirements will be presented on the strain acceleration. Moreover, on board of each spacecraft a so-called *Time-Delay Interferometry* (TDI) is used to take out the laser frequency noise and obtain a more pure signal of any gravitational wave that has interacted with space-time [10]. An intense work of pre and post processing can be made in order to extract the real data from the measurement. It must be highlighted that many sources of gravitational wave in the entire spectrum are quite speculative, or have highly uncertain amplitudes.

1.2.2   Science objectives

The science theme of The Gravitational Universe is addressed here in terms of Science Objectives (SOs) and Science Investigations (SIs), and the Observational Requirements (ORs) necessary to reach those objectives. The ORs are in turn related to Mission Requirements (MRs) for the noise performance, mission duration, etc. The assessment of Observational Requirements (ORs) requires a calculation of the Signal-to-Noise-Ratio (SNR) and the parameter measurement accuracy. The SNR is approximately the square root of the frequency integral of the ratio of the signal squared, $\tilde{h}(f)^2$, to the sky-averaged sensitivity of the observatory, expressed as power spectral density $S_h(f)$ [11].

The majority of individual LISA sources will be binary systems covering a wide range of masses, mass ratios, and physical states. The SOs for LISA describe the science that LISA will enable. The subsequent SIs highlight the ways of obtaining the science by evaluating the LISA data.

- SO 1 Study the formation and evolution of compact binary stars in the Milky Way Galaxy

- SO 2 Trace the origin, growth and merger history of massive black holes across cosmic ages

- SO 3 Probe the dynamics of dense nuclear clusters using extreme mass-ratio inspirals (EMRIs)

- SO 4 Understand the astrophysics of stellar origin black holes

- SO 5 Explore the fundamental nature of gravity and black holes

- SO 6 Probe the rate of expansion of the Universe

- SO 7 Understand stochastic gravitational wave backgrounds and their implications for the early Universe and TeV-scale particle physics

- SO 8 Search for gravitational wave bursts and unforeseen sources

1.3   Mission Profile

The LISA observatory is a constellation consisting of three S/C traveling in near-circular heliocentric orbits. The initial conditions of these orbits are chosen in such a way that the three S/C form an equilateral triangle with side length of $2.5\,Mkm$ for the whole duration of the mission (with some slight deformation due to disturbances). Any two arms of this triangle represent a Michelson-type interferometer. The triangle center moves on an Earth-trailing heliocentric orbit with a radius of about $1\,AU$, which is the distance from Earth to the Sun. The true anomaly of the center is 19 up to 25 lower than the true anomaly of the Earth. Therefore, the S/C are located at $50 \cdot 10^6\,km$ up to $65 \cdot 10^6\,km$ from our planet. Each S/C contains two optical assemblies, each containing a test mass [12].

To ensure the longest science phase, a particular orbit has been designed for the formation flight. This peculiar orbit called "cathweel" makes possible to have a continuous facing of the three spacecraft. Let us indicate the constellation plane as the one on which lies the laser arm of each S/C (in the nominal motion) and with the z axis pointing towards the

Sun. This means that, besides the natural circular counterclockwise motion around the Sun, each S/C will circulate in a clockwise spin around the z axis of the constellation plane. The recommended option for LISA is to use one of the Ariane 6 family of launch vehicles, with a dedicated Ariane 6.4 launch being the preferred option [11].
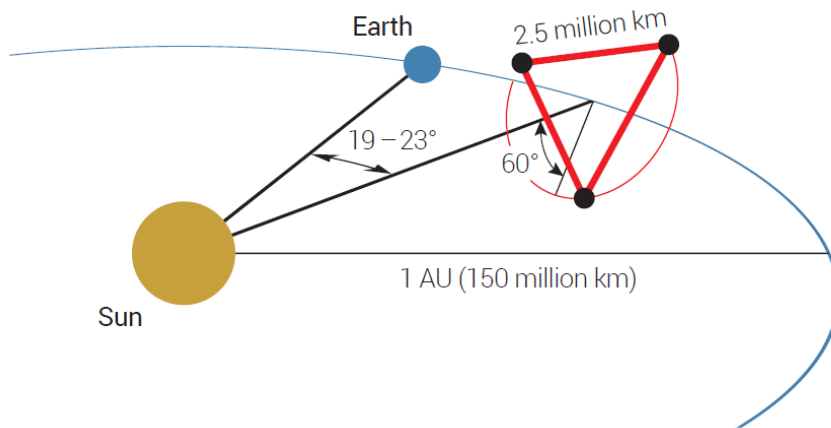
Figure 1.8.   Depiction of the LISA constellation orbit, [11].
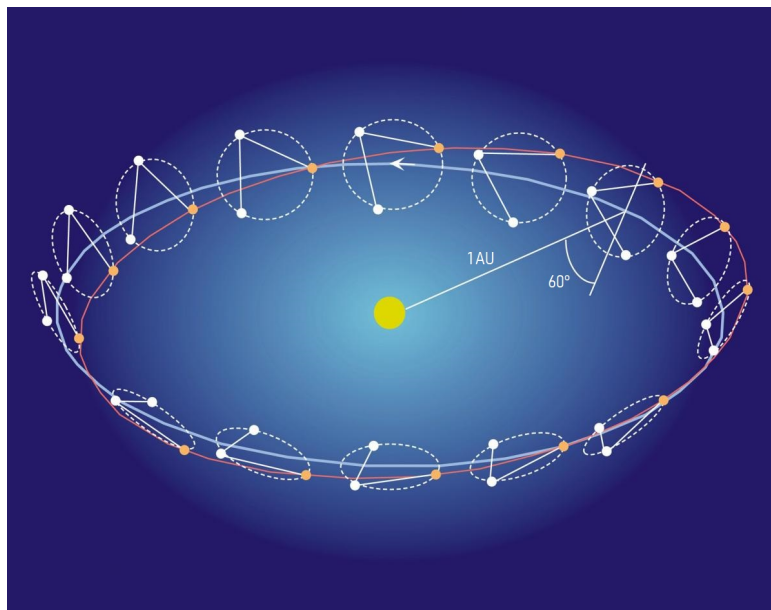
Figure 1.9.   Depiction of the LISA orbit around the Sun. Credit: NASA.

Besides the measurement technique, another key point of the mission is the drag free spacecraft based on inertial sensors. The acquisition of science measurements must be based

on the certainty of having the test masses on each spacecraft flying in a disturbance-free motion along their geodesics. In particular, the goodness of the data is strictly related to this concept. The geodesic motion of a mass in a solar body system only depends on the mass, and on the orbital parameters. It can be proven from the Newton's law, but easily from the same law it can be deduced that if an orbit is affected by a disturbance it will diverge from the geodesic motion, i.e., disturbance-free motion.

1.3.1 Concept of operations

The operation aspects dedicated to the first propulsion module required to bring into orbit each sciencecraft are not presented in thi section. More important for the DFACS design are the concept of operations related to the sciencecraft. Once that each sciencecraft is placed into orbit, the formation flight must be acquired in order to form the space observatory. In sequence the S/C must perform the release of the TMs, previously kept grabbed by the housing system, and the arm signal acquisition. The maneuvers to perform these operation will be demanded to the DFACS . Once constellation acquisition and calibration are performed correctly, LISA should be able to enter the science mode.

The duty to achieve a true geodesic motion for the test masses must be accomplished by the LISA sciencecraft. Is not possible to control the TMs in order to make them follow their undisturbed orbit, thus it is necessary to force the spacecraft to follow the TMs in their motion . In this way the sciencecraft is forced to follow the orbit traced by the TMs on their interferometry axis, which can be considered a geodesic motion due to the shield effect made by the same sciencecraft. As a result, the drag-free operations are related to the performance of the actuation system equipped on the spacecraft. Indeed, each spacecraft is provided by a Micro Newton Propulsion Assembly (MPA) composed by three *Micro-N Propulsion System* (MPS) that will allow to act with the required performances on the relative position between the S/C and the TMs. Drag-free control using micro-Newton thrusters will steer the S/C to follow the TMs, ensuring they are left in free fall following their geodesic trajectories along the lines of sight between the spacecraft. The remaining degrees of freedom being controlled with an *Electrostatic Suspension* (ES) system to follow the spacecraft motion, which must be attitude controlled to point the telescopes and communication antennas [13].

"The spacecraft are actively controlled to remain centered on the test masses along the interferometric axes, without applying forces on the test masses on these axes." [1].

The environment, i.e., the housing, in which the test masses have to stay must be as quieter as possible. It is however required to sense the position of the TM in the housing and then act with the required forces and torques on the non-interferometric axis in order to establish the drag-free operation. Moreover, the same presence of the mass of the spacecraft is a source

of disturbance due to the gravity that the S/C exercise on the TM. It emerges the fact that the S/C isolates the TMs from the external environment and placing them into another one, not completely disturbance-free. Sensor and actuators of the housing must be designed with certain requirements and then employed trying to minimizing their effects on the TMs and so avoiding that the GW starin is hided under the noise of sensors and actuators or under the motion of the sciencecraft.

As said before, the main requirements will be established on the acceleration as a more reliable source of data. The amplitude spectral density of the residual acceleration of the test mass characterizes the disturbance reduction, the first basic function of the science instrument.

The test masses are $46mm$ cubes, made from a dense non-magnetic Au-Pt alloy (figure 1.10) and shielded by the *Gravitational Reference Sensor* (GRS). The GRS core is a housing of electrodes, at several mm separation from the test mass, used for $nm/\sqrt{Hz}$ precision capacitive sensing and nN-level electrostatic force actuation in all non-interferometric degrees of freedom. The GRS also includes fibers for UV light injection for photoeletric discharge of the test mass and a caging mechanism for protecting the test mass during launch and then releasing it in orbit. The GRS technology is a direct heritage from LISA Pathfinder [1]. Moreover, the nominal mission duration in science phase is proposed to be at least 4 years with a science extension of 6 years for a nominal total extended lifetime of 12.5 years.
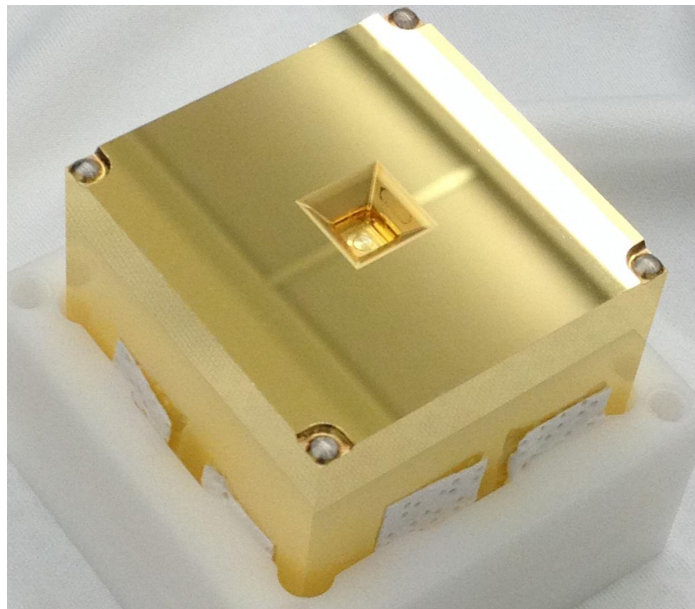
Figure 1.10.   One of LISA Pathfinder's two test masses. Credit: RUAG Space, Switzerland.

1.3.2 Science performance requirements

In the previous section we have briefly examined the aspects of a space-based gravitational wave observatory. Now we can present the key measurement performance requirement attributed to the mission. The peculiarity of the LISA mission will be the possibility to study the GWs in the low frequency band, i.e., the requirements are from $100\mu Hz$ to $0.1Hz$. The expected goal is to extend the requirements with one order of magnitude in both frequency directions. The total effective single TM acceleration noise level shall be

$$S_a^{1/2} \leq 3 \cdot 10^{-15} \frac{ms^{-2}}{\sqrt{Hz}} \cdot \sqrt{1 + \left(\frac{0.1mHz}{f}\right)^2} \sqrt{1 + \left(\frac{f}{8mHz}\right)^4} \qquad (1.1)$$

This requirement holds for the interferometry axis of each test mass. Without any doubt the total effective displacement acceleration noise in a one-way single TM-to-TM link will be the most relevant control performance quantity. As a matter of fact, the requirements limits the stray accelerations of the geodesic reference TM, thus it is mainly applicable to the GRS. As a result, the LPF experiment flight results supported the consolidation of the differential acceleration performance and the relevant requirement, with a little margin included [11].
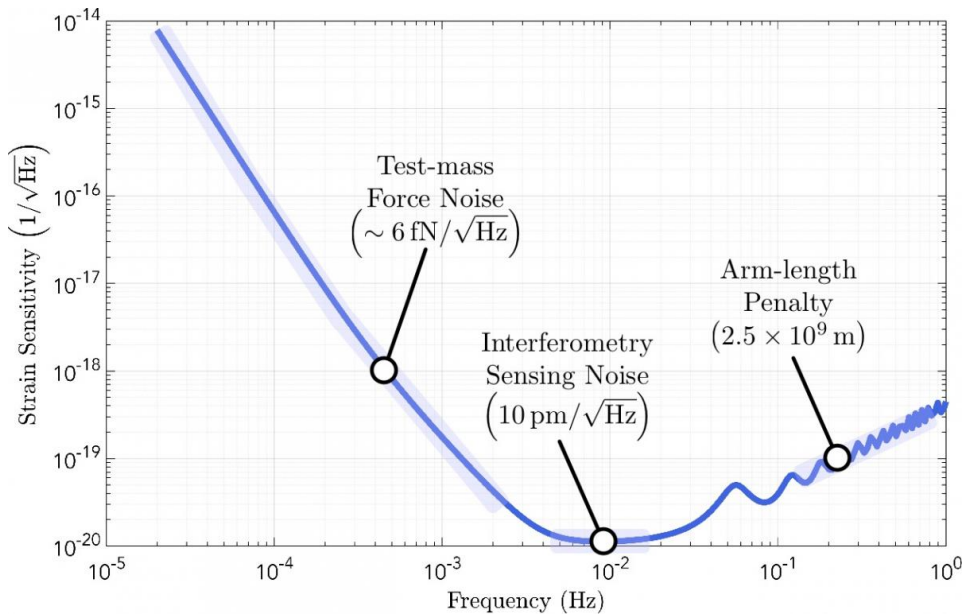
Figure 1.11. Strain sensitivity plotted as a linear spectral density. Credit: LISA Consortium.

With the same frequency requirements range the displacement noise of the interferometric

TM-to-TM ranging with a proposed requirement of

$$S_{IFO}^{1/2} \leq 10 \cdot 10^{-12} \frac{m}{\sqrt{Hz}} \cdot \sqrt{1 + \left(\frac{2mHz}{f}\right)^4} \qquad (1.2)$$

where $S_{IFO}^{1/2}$ is the effective total displacement noise in a one-way single link TM to TM measurement. The major drivers affecting the test masses displacement requirement are their acceleration noise, and the *Laser Interferometer* (IFO). From this perspective, limiting the TM displacement will enforce the IFO measure of the path-length variations caused by GWs, with the required accuracy.

As said before, the measurable strain is strictly related to the SNR given by the instrument. As a matter of fact, LISA will achieve 10^{-20} strain resolution by measuring displacements of the order of a picometer only if the requirement will be met.

1.4 Outline of the thesis

In this thesis, an extensive review effort has been devoted in the existing LISA and LPF publications. As a consequence, after the first introduction chapter, the following second chapter is dedicated to a detailed system-level definition in which the relevant aspects of the mission, including performance models for the sensors, actuators and all foreseen disturbances are taken into account.

The third chapter presents a discussion on the nonlinear mathematical model of the dynamics that govern the LISA mission. The nonlinear model is then linearized and studied in this simpler form in order to support the control design. The final model includes all the degrees of freedom related to a single sciencecraft. Preliminary prototyping in a representative simulation environment is also implemented

The fourth chapter is dedicated to the control design phase of the attitude system. After a brief overview on the guidelines applied in the preliminary control design, a set of controller is designed and tested for different mission phases.

Finally, in the last chapter conclusions on the overall work are presented.

Chapter 2

System-Level definition

2.1 Introduction

As mentioned before, the main focus of the LISA constellation will be the GWs detection via an interferometric measurement of the differential optical path-length modulation along the three sides of a triangular configuration defined by free-falling test masses. Hence, starting from the LPF heritage, each one of the three LISA S/C will be endowed by two TMs, each one dedicated to a single interferometry arm. Within their cage and the S/C, the test masses will follow their geodesic trajectories with sub-femto $g\sqrt{Hz}$ spurious acceleration [11]. The schema is showed in figure 2.1

The two TMs are contained inside co-orbiting drag-free spacecraft and surrounded by a GRS [15], [11], possibly also arranged according to the drift mode accelerometer concept [16], to provide distance measurements with *pm* precision [17], [18]. The proposed GRS subsystem [19] is based on the heritage of LPF, and it has demonstrated the LISA top-level acceleration noise requirement, as well as TMs position sensing [20] and other functionality requirements. In short, the adopted GRS is designed to provide:

- S/C and TM position sensing in some relevant directions,

- TM actuation forces and torques,

- shielding to the TM in order to limit stray forces.

In addition, the GRS is responsible for the TM caging during the launch and its release on orbit, and the discharging to neutralize the TMs [22], [23], [24]. Jointly with the TMs and the GRS, the LISA S/C payload is characterized by two identical assemblies of roughly cylindrical shape, each of which contains a telescope, an optical bench and a GRS with its enclosed TM.
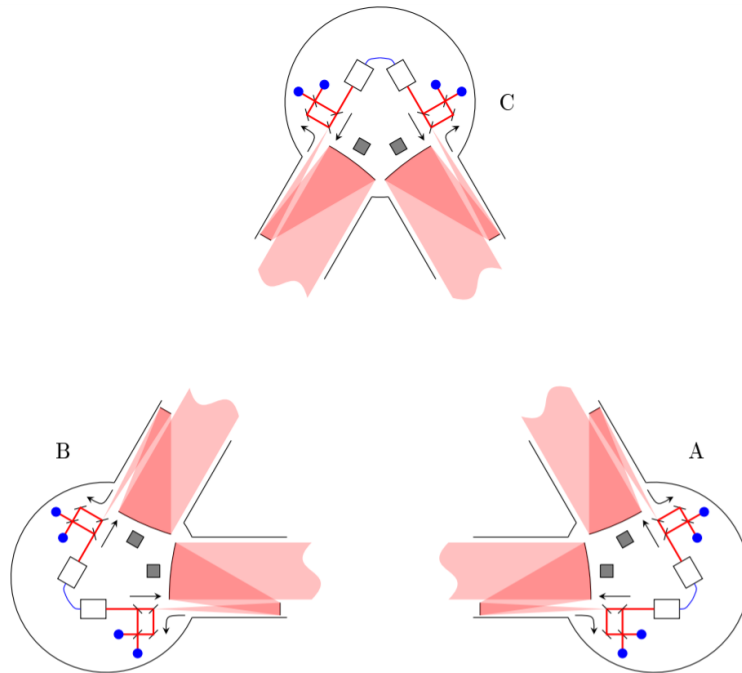
Figure 2.1.   Simplified optical layout of the LISA interferometer, [14].

In figure 2.1, the two assemblies of each S/C are connected, in a common frame, by a mounting structure able to rotate them about the vertical axis to reach mutual alignment of the laser beams along the LISA arms, against the variation of the vertex angles due to solar system dynamics.

Again, from the measurement perspective, laser interferometers are employed to measure path-length variations, namely the distance variations among the TM along the triangle arms, caused by GWs, down to the pm level [11]. In addition, laser interferometry is used to monitor the distance changes between the test masses and the optical bench inside each S/C; a technology demonstrated by the LISA Pathfinder mission [25], [26], [27] [28]. Interestingly, since the interferometers are intended to be all-sky monitors of GWs [11], no pointing or orientation towards specific sources is foreseen [29], [30], [31]. In turn, the science interferometry measurement imposes two main control requirements:

- each geodesic reference TM must be "force free" along its interferometry axis (thus requiring a properly designed drag-free control of the S/C)

- the telescopes must be pointed to the distant S/C (*nrad* DC pointing accuracy).

The latest objective is enforced by the Differential Wavefront Sensing (DWS) technique.

DWS, successfully flown in LPF [32], measures the angle between the interfering wave-fronts, thus provides pitch and yaw angular readouts of the TM wrt the optical bench, and of the S/C wrt to the incoming beam. These signals will then be used as part of the DFACS [9], [31].

Concerning the actuation setup, each LISA S/C is equipped with its own propulsion module to reach the desired orbit [14], [33], as well as DFACS system, leveraging the heritage of the cold gas propulsion system flown on LISA Pathfinder [34], [35], [36] (with an enlarged cold gas storage capacity, due to the higher mass and mission duration). Electrostatic actuation needs to be tracked as a possible source of stray force noise [11].

2.1.1 Sources of disturbance

A relevant aspect in the LISA and LPF literature is the analysis of the sources of disturbances, both internal and external, affecting the several part of the missions and platforms, and potentially undermining the final scientific measurement performance. To this aim, one of the mission most important sub-scenario to be taken into account is the Science Mode.

In the Science Mode, near-continuous operations of the gravitational observatory system, at the design sensitivity and performance, are carried out. As a consequence, at the Science Mode, the system design should be such that that external perturbations are minimized and neither station keeping nor orbit correction manoeuvres are required.

Of course, as observed during the LPF system design phases, reaching the GW missions ambitious targets requires a significant amount of system optimization and characterization from the disturbance perspective, thus implying accurate and quantitative noise analysis procedures [37], [38].

As mentioned before, the most challenging result to reach for the LISA mission is the detection and then the inhibition of noise affecting the gravitational wave measurement. The sensitivity is a measure of the way in which the noises act on LISA. From this point of view, the first necessity is to assume the right allocation of disturbances in the system in terms of budget.

Putting together all the disturbances to establish the requirement, it is outlined the "V-shape" of the differential acceleration noise budget. A particular distinction can be made between the effect that disturbances produce on the system. The sensitivity can be influenced by acceleration noise sources and by displacement noise sources. In the study of the sensitivity of the system these influences must be treated differently. Indeed, two main requirement are given on displacement and acceleration noise. The displacements or optical path-length noise sources affect directly the measurement of the position of the test mass i.e., the noise fakes fluctuations in the lengths of the optical paths. In this category takes place shot noise but
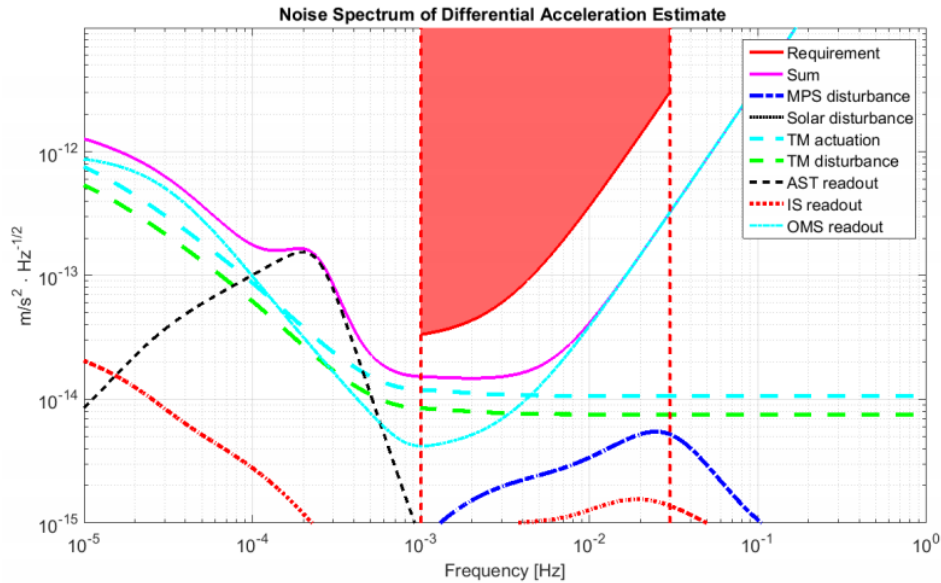
Figure 2.2.   Predicted differential acceleration performance prior to launch, [6].

also allocations for pathlength variations, laser frequency and amplitude noise, clock noise, stray light, phasemeter electronics noise and tilt-tolength coupling.

The acceleration noise takes into account many kind of sources most of them ironically come from the spacecraft itself, i.e., actuation fluctuations, Brownian noise, TM charge and stray potential fluctuations, spacecraft coupling, magnetic and thermal gradient effects [11]. Now, we can present the disturbance sources on the DF control system in four categories.

1) The first category includes all the external forces (surface and volume) which the Drag Free controller is demanded to remove i.e., environmental disturbances and in some cases to accurately use:

- Thrust actuation noise

- Electrostatic actuation noise

- Telescope actuation noise

- Difference in acceleration between TM and SC in their CoM

- Solar radiation Pressure

2) The second category of disturbances are related to the interactions internal to the SC, in particular the ones brought by the SC, as complex system:

- Thermal noise

- Pressure fluctuation

- Spacecraft self-gravity

- Magnetic forces

- Induced charge

3) The third category collects all the sources of noise produced by sensing the position of the TM, which will act directly on the error in feedback to the MPS, ES and *Inter Telescope* (IT):

- Optical metrology sensing noise

- Read-out bridge

4) It can be taken into account a fourth category which addresses for noise sources non-dominant for the drag-free performances in the required frequency band.
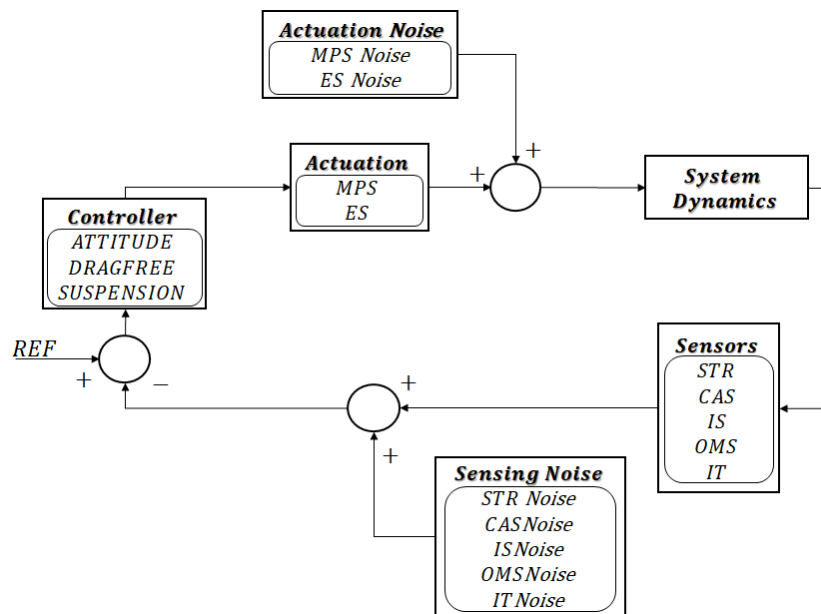
Figure 2.3. Block diagram with noise-shape filters.

Of course, these disturbances affect from different point of view the LISA components and so every source must be in the right place. In order to introduce noise effect into the model, a noise-shape filter approach has been used. Each disturbance will be generated starting from a white noise which feds the noise filter and produces a colored noise. In general,

noise-shape filter approach has been used for the disturbances acting on the payload and on the S/C. Similarly, in order to meet the sensitivity goal, each actuator and each sensor must be correlated by an accurate noise shape filter.

2.2 Sensors

In order to implement some feedback control law for actively stabilizing LISA S/C, it is necessary to have information on the current satellite attitude, on the current relative attitude and position between S/C and TMs and off course the current misalignment from the incoming laser beam. These information are provided by sensors that, in particular for LISA mission, are based on significantly different principles, depending on the S/C mode and the related pointing accuracy requirements. Roughly speaking, it is possible to group the common attitude determination hardware, applicable for the LISA mission, into 3 categories:

- Sun sensors

- Star trackers

- Payload-based sensors

Sun sensors should be never singularly involved for any phase of the mission, but are here cited as being part of the on board equipment. The *Star Tracker* (STR) is certainly the most accurate measurement instrument used for the inertial attitude. It is common to have its measurements as feedback quantity for the attitude control. As a matter of fact, the STR is not the most reliable sensor on board. A significant aspect of the mission is the possibility for the on board control system to leverage the geodesic motion of the TMs through the sensing of their coordinates with the GRS and *Optical Metrology System* (OMS). It is clear that the TMs can be treated as gyroscopes only in their geodesic motion. Certainly, to allow this sensing contribution from the payload it has to be ensured its free-falling flight.

The models presented in this section are those of the sensor equipment exploited on board of each SC to acquire every necessary measure for the success of the mission. These measurement systems are:

- Star Tracker

- Constellation Acquisition Sensor

- Inertial Sensor

- Optical Metrology System

- Inter Telescope Sensing

2.2.1 Star tracker

Star trackers are the most accurate and complex attitude sensors. They are based on a simple principle, that is, the attitude of the spacecraft is determined by comparing the position of a known set of stars with a catalogue, so that whole information on three attitude degree of freedom is readily available. In turn, the performance of the sensor are related to the facts that (i) stars provide a very faint reference and (ii) a significant amount of memory (to store the star catalogue) and processing capabilities (for matching the current view with the catalogue) are required.

The *Star Tracker Assembly* (STA) shall provide 3-axis inertial attitude information only during the constellation acquisition process. Every SC being part of the constellation is equipped by 2 STRs. The measurement process takes into account systematic [13] and random noises [39], [40] at STR level. It is assumed that the STRs are mounted approximately along the line of site of the inter-telescope.

Table 2.1. STA performance

Characteristic	Values
FoV	$13.25° x 13.25°$
Attitude accuracy	<1 arcsec xy-axes
	<10 arcsec z-axis
Attitude re-acquisition	<5 s (without a priori info)
	<0.5 s (with a priori info)
Slew rate	$<0.3°/s$ (full performance)
	$[0.3, 2]°/s$ (reduced performance)
Sampling time	250 ms
Noise	2 arcsec xy-axes
	10 arcsec z-axis
Assumed delay	100 ms

The main characteristics of the STA are reported in the Table 2.1. The transformation from the IF to the generic STR measurement frame STMF_{ji}, directly measured by the STRji, accounts for the measurement errors. Formally speaking, the mounting matrix is used to report the measurements in terms of SF as follow

$$T_I^{STR_{ij}} = T_{SF_i}^{STR_{ij}} T_I^{SF_i}$$

The measure is affected by a delay. The delay is introduced to manage measure acquisition and measure computation and when necessary to attitude re-acquisition. Actually, the model is quaternion-based and accounts for bias and noise introduced as an error quaternion. The bias is static and the noise is modelled by a white noise with gaussian distribution reshaped to
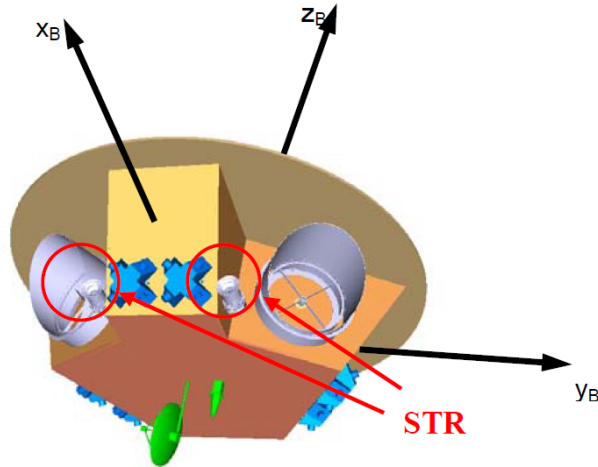
Figure 2.4.   LISA star trackers location, [10].

the noise value defined by each axis spectral density. The STR output measure is quantised and saturated.

2.2.2   Constellatoion Acquisition Sensor

The only STR pointing of the distant satellites has been determined to be insufficient to ensure laser link acquisition on the interferometer detectors. For this reason, the LISA Payload will contain a *Constellation Acquisition Sensor* (CAS) to aid in the process of constellation acquisition. The sensor is hosted in the telescope and is able to detect the incoming laser beam direction with the following performances [13]:

Table 2.2.   CAS characteristics

Characteristic	Values
Measurement range	$\pm250\mu$rad
Angular resolution (effective)	1μrad
Max. tracking speed	2.5μrad/s
Sampling rate	> 10Hz
Operating mode	centroid

The CAS enables beam direction acquisition only when the beam is visible on the sensor, in the case of no signal being detected the scanning phase goes on with its next step, until a signal is detected. In other words, during the constellation acquisition, the measure given by

the CAS is the angle between the *Optical Assembly* (OA) longitudinal axis of the first S/C and the incoming beam direction, thus, the OA longitudinal axis of the second S/C.

The model shall accounts for noise shape, accuracy and slew rate.

2.2.3   Optical Metrology System

The OMS is in charge to generate the laser beam, perform interferometry and measure distances along the sensitive axis. Furthermore, thanks to some signal processing techniques, it is able to measure some angular quantities such as the TM pitch and yaw angles with respect to the incoming laser beam. The OMS is composed by the Reference Laser Unit, the Laser Modulator, the Optical Bench Interferometer and finally the phasemeter. The optical bench is interfaced with the telescope thanks to a small aperture of few *mm*. Each telescope has an aperture of about 30*cm* and allows to transmit and receive laser beams simultaneously. The overlap of the beams is minimized thanks to a particular design of the internal reflectors. Moreover, each telescope is equipped with the so called Point Ahead Angle Mechanism, which allows compensate for the out-of-plane component of the Point Ahead Angle.

In the following table are reported the characteristics of the OMS

Table 2.3.   OMS characteristics

Characteristic	Values
Measurement range	$\pm 100 \mu$m
Max tracking speed	2μm/s
DC angles (S/C to TM)	3μrad
DWS angles inner/detected	$\pm 50 \mu$rad / $\pm 300 \mu$rad
DWS inner FoV	0.3μrad
DWS detected FoV	100μrad

The constellation is able to perform the science measurement on each arm thanks to the OMS. The instruments can measure inner distance between TM1 and OB i.e., S/C1, and arm distance between opposite OBs. The measurement noise on the displacement along the constellation arm are:

- $S_{OMS,p1}^{1/2} < 10 \frac{pm}{\sqrt{Hz}} \sqrt{1 + \left(\frac{2mHz}{f}\right)^4}$ for the inner distance;

- $S_{OMS,p2}^{1/2} < 1.5 \frac{pm}{\sqrt{Hz}} \sqrt{1 + \left(\frac{2mHz}{f}\right)^4}$ for the arm distance.

In addition, the OMS will have the capability of measuring different relative attitude angles. For the TMs are given the Horizontal/Vertical tilt (w.r.t. S/C) perpendicular to laser in

Direct Current (DC) and Differential Wavefront Sensing (DWS). For the S/C are given the Horizontal/Vertical tilt perpendicular to incoming laser beams in Differential Wavefront Sensing (DWS). The measurement noise on the angles given for TM and S/C are given:

- $S_{OMS,a1}^{1/2} < 0.12 \frac{nrad}{\sqrt{Hz}} \sqrt{1 + \left(\frac{1mHz}{f}\right)^4}$ for the inner measure;

- $S_{OMS,a2}^{1/2} < 35 \frac{nrad}{\sqrt{Hz}} \sqrt{1 + \left(\frac{1mHz}{f}\right)^4}$ for the detected measure.
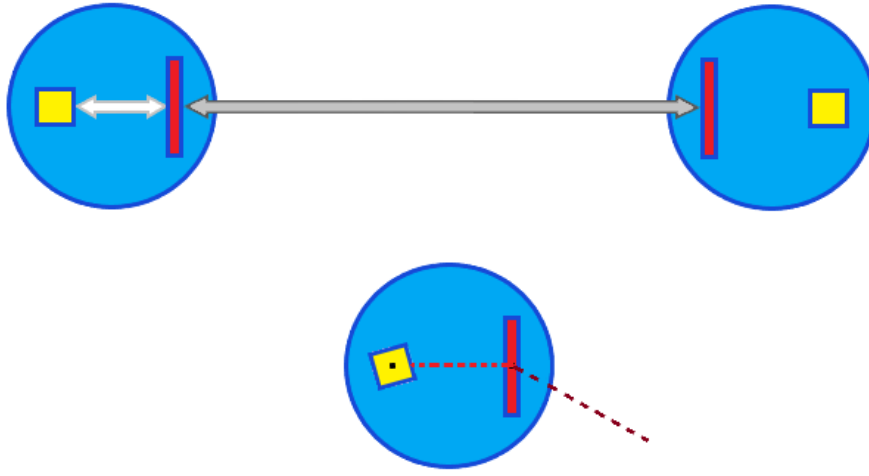
Figure 2.5.   OMS inner and long arm distance and detected angles measurements.

Regarding the DWS, the instrument is able to provide the S/C relative attitude in terms of misalignment angle between the incoming beam and the first axis of OF, from which are indirectly obtained θ_S and ζ. The measure of the angles is affected by the sensing noise of the instrument. Below is presented the implementation of the noise shape filter.

$$H_{OMS,p1} = 10^{-11} \frac{\left(s + 1.3 \cdot 10^{-2}\right)^2}{\left(s + 1 \cdot 10^{-5}\right)^2}, \qquad H_{OMS,a1} = 0.12 \cdot 10^{-9} \frac{\left(s + 6 \cdot 10^{-3}\right)^2}{\left(s + 1 \cdot 10^{-5}\right)^2},$$

$$H_{OMS,p1} = 1.5 \cdot 10^{-11} \frac{\left(s + 1.3 \cdot 10^{-2}\right)^2}{\left(s + 1 \cdot 10^{-5}\right)^2}, \qquad H_{OMS,a1} = 35 \cdot 10^{-9} \frac{\left(s + 6 \cdot 10^{-3}\right)^2}{\left(s + 1 \cdot 10^{-5}\right)^2},$$
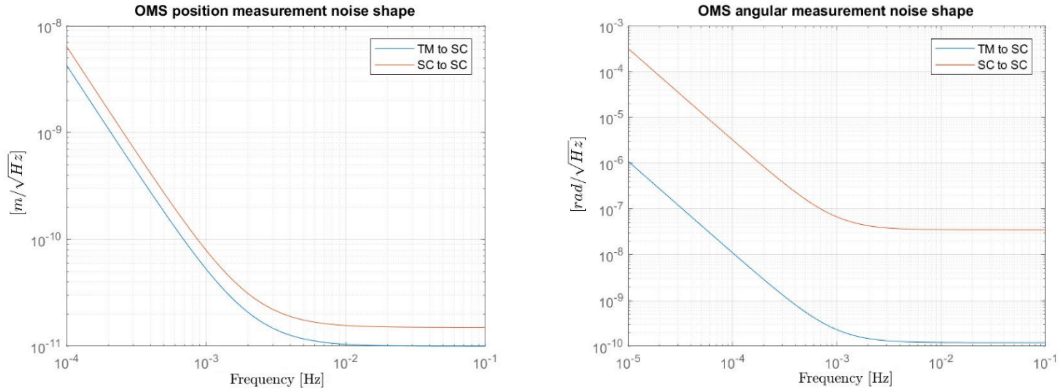
Figure 2.6.   OMS position (left) and angular (right) measurement noise shape.

2.2.4   Inter-telescope

Practically, the LISA Optical Assembly (OA) Subsystem consists of two Optical assemblies, oriented at a nominal angle of 60° and associated electronics. Each OA serves one of the two adjacent interferometer arms and is rotated as a whole within the constellation plane in order to cope with the breathing angle. The single OA is considered as a body inside the S/C constituted by the telescope, the optical bench implementing the interferometers and the GRS, which contains the TMs.

Since the LISA constellation has no formation flying control, it is expected that the pointing is guaranteed by the actuation of the inter-telescopes on each arm of the constellation. It is well known that the variation of the breathing angle is bounded and periodic, with maximum amplitude of and a maximum angular rate of change of 5 nrad. Every couple of opposite telescopes is actuated during constellation acquisition to scan the second laser once the first arm has been acquired and in the science mode to track the opposite S/C with the telescope boresight. Simultaneously the telescopes belonging to the same S/C contributes to the regulation of the breathing angle ζ. The OA actuation is given by a piezo-electric mechanism capable of step-moving the optical assemblies with a resolution of 1 nrad/step. The actuator is modeled as a second order dynamic system.

2.3   Actuators

Spacecraft control actuators can be based on different physical principles. The choice in the type of actuator installed on board of the satellite greatly affects its configuration, the resulting pointing accuracy, and even the implementation of the control laws themselves. A

Table 2.4.   IT characteristics

Characteristic	Values
Actuation range	±0.5deg
Resolution in nanostep mode	1nrad
Max. tracking speed	2.5μrad/s
Actuation noise	10nrad

control action can be delivered to the satellite by either a direct torque produced by a (set of) thruster(s) or other reaction control system (RCS), by exchanging angular momentum between parts in relative rotational motion. In this category we have:

- Cold gas jets

- Chemical propulsion (Mono–propellant or Bi–propellant propulsion system)

Momentum exchange devices can be listed as follow:

- Reaction wheels

- Bias–momentum wheel

- Double–gimbal bias–momentum wheel

- Control Moment Gyroscopes

Actually, for each S/C of the LISA mission, the attitude should be managed by a MPS able to perform the maneuvers with the required precision. The attitude and the position of the two TMs in the suspended coordinates are entrusted to the actuation module of the GRS, the ES system. Should be counted as an available actuator the inter telescope mechanism, that is used to ensure the pointing accuracy contrasting the breathing angle changing (±1°).

2.3.1   Micro-N Propulsion System

Generally speaking, in order to actively stabilize the satellite in the presence of external disturbances and allow for autonomous manoeuvres and drag-free operations, the satellite must be equipped with a suitable set of sensors and actuators, the former provide the on–board computer with the necessary information on the current attitude and consequently the latter will perform the requested manoeuvre from the control system. The precision of the control action depends on the accuracy of the attitude measurement.

Moreover, the control law itself depends on the type of actuators available. During the actuated phase of the mission, the 3–axis stabilised spacecraft featuring only a reaction control system will continuously bounce back–and–forth between the edges of the allowed dead–band, under the alternating action of a disturbance torque and the quick reversal provided by a control pulse at one of the edges of the dead–band. The control action can be continuous, if momentum exchange devices are employed, although the amount of angular momentum stored in the wheel is expected to grow during the actuation phase, so that a wheel desaturation manoeuvre is usually necessary, which requires the use of external torques, usually provided by a set of thrusters.

Each LISA spacecraft is equipped with 3 cold gas micro-Newton propulsion assemblies that have the characteristics shown in 2.5. It should be noted that the thrust resolution and the bias error are not equal in the entire thrust range.

Table 2.5.   MPS performance

Characteristic	Values
Maximum thrust	500μN
Minimum thrust	1μN
Thrust resolution	0.3μN $(1-100\mu$N$)$ 1μN $(100-500\mu$N$)$
Thrust resolution	$\pm0.5\mu$N $(<4\mu$N$)$ $\pm2\mu$N $(4-150\mu$N$)$ $<10\mu$N $(>150\mu$N$)$
Response time to 95% of demand	$<$2s
Thrust overshoot	2% of steady state value
Thrust direction bias	0.5°
Thrust delay	0.1 s
Thrust update rate	10 Hz
Thrust noise	5μN$/\sqrt{Hz}$ at 0.1mHz 0.1μN at 100mHz

According to tab 2.5, thrusters are arranged in 3 pods located 120° degrees apart and have a higher canting towards $+z$. Such a configuration has been reproduced in Matlab-Simulink and is shown in figure 2.7.

For each thruster the resultant output thrust is given by three contributions, formerly the thruster dynamics, the bias and the thrust noise:

$$F_{T,real} = F_T + F_{T,bias} + F_{T,noise}$$

Where F_T is given by a standard second-order delayed dynamic model:

$$F_T(t) = G(t)u_T(t - \delta_T)$$

28
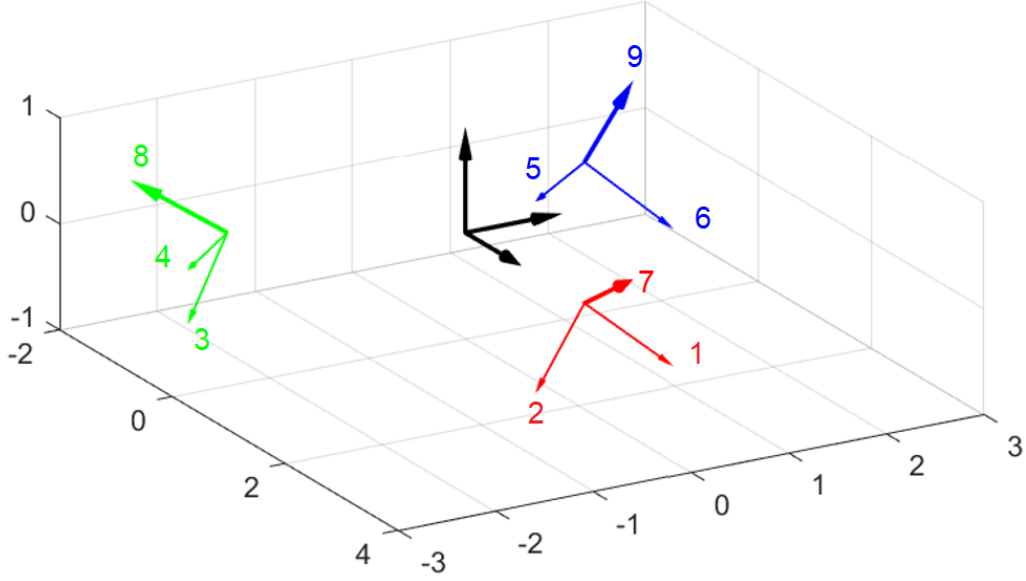
Figure 2.7. Thrusters configuration and disposition.

$$G_T(s) = \frac{\omega_T^2}{s^2 + 2\zeta_T \omega_T s + \omega_T^2}.$$

Regarding the dynamic adopted for the system, $u_T(t - \delta_T)$ is the delayed reference input thrust coming from the DFACS controller. Natural pulse and damping ratio are assumed as $\omega_T = 2\pi f_T = 2\pi \cdot 1.17$ and $\zeta_T = \frac{c}{c_r} = 0.787$ in order to ensure a response time of 2s (95%) and a 2% of the steady state value as reported in tab 2.5. The delay is assumed to be $\delta_T = 0.1$s.

The thrust bias $F_{T,bias}$ is taken from tab 2.5 while $F_{T,noise}$ is given by a white noise w_d passed through a filter whose zero/pole transfer function $H_{T,noise}(s)$ resembles the amplitude spectral density given in the [12]. Thus:

$$F_{T,noise} = H_{T,noise}(s) w_d$$

$$H_{T,noise}(s) = 1 \cdot 10^{-7} \frac{\left(s + 2\pi \cdot 10^{-2}\right)^2}{\left(s + 2\pi \frac{10^{-2}}{\sqrt{50}}\right)} = 5 \cdot 10^{-6} \frac{\left(\frac{10^2}{2\pi}s + 1\right)^2}{\left(\frac{10^2 \sqrt{50}}{2\pi}s + 1\right)^2}$$
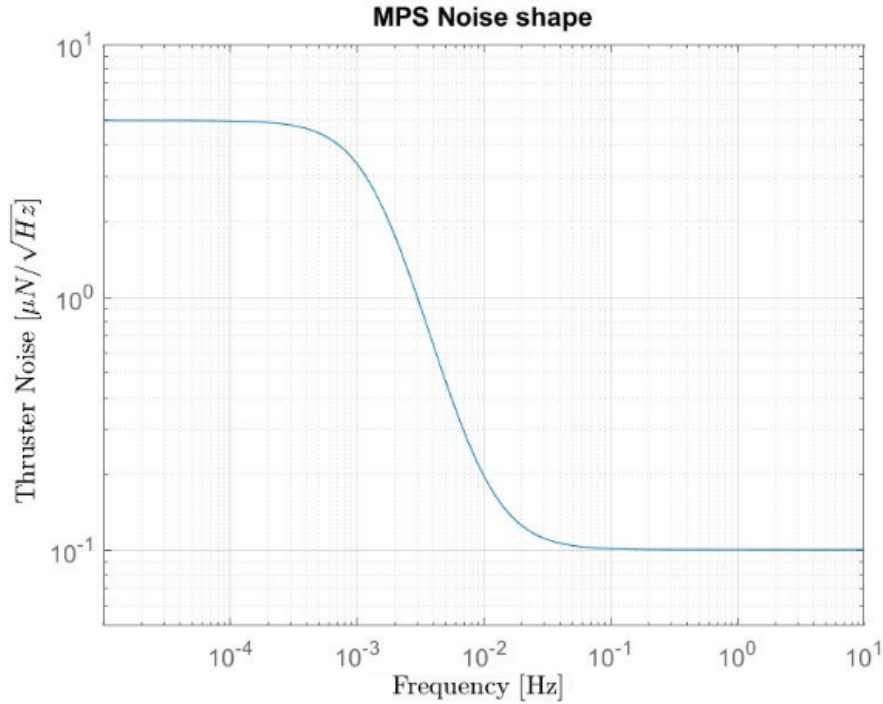
Figure 2.8.   MPS noise shape filter.

2.3.2   Electrostatic Suspension

The TMs are shielded by the SC that employs precision thruster to follow the DF TM orbits, based on measure on the relative position given by the *Inertial Sensor* (IS). Off course, the system serves as actuator for the suspension loop on the TM. In this actuation role the subsystem involved is the ES.

The subsystem exploits capacitive sensing and electrostatic actuation to control all 6 DoFs of each TM. In both function the subsystem can operate with different measurement range and performance, *Wide Range* (WR) and *High Resolution* (HR), thus different noise shape.

To meet the objectives set for each priority mode in which the ES is used, the forced applied on the TM must be modulated by the applied voltage in order to span it in two orders of magnitude. The 6 DoFs of the TM are measured by capacitive bridges metrology. The bridge has the operational noise presented in table. The resolution of the system shall enable the control system to meet the centering requirements for the mission. For the LISA mission, the electrostatic suspension system has indeed the characteristics of a variable capacitor due to the variable position of the TM in the cage. The plates of the capacitors are numerated as
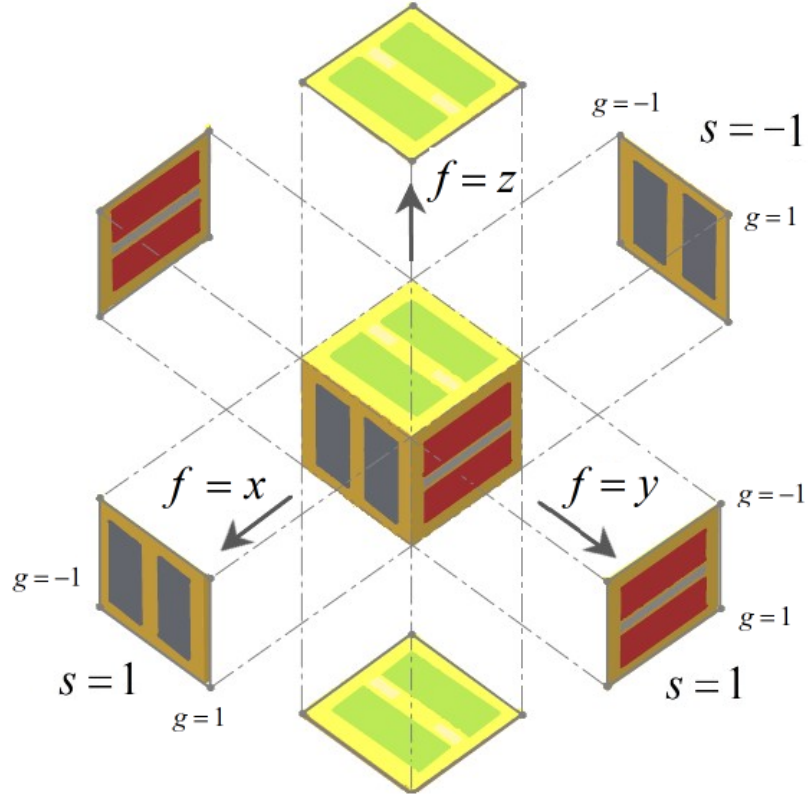
Figure 2.9.   GRS configuration.

presented in figure 2.9. Where $f = x, y, z$ denotes the axis orthogonal to the TM face, $g = \pm 1$ denotes the two plate sections on each face (1 has positive coordinate along an axis of the face and -1 negative coordinate), and $s = \pm$ denotes the positive and negative face along the orthogonal axis.

Table 2.6.   WR mode characteristics in actuation and sensing

Measurement ranges	Performance range	Full/Sensing saturation range	Actuation authorities	Max
Linear [μm]	100 in x	> 2000	Force per unit mass [nm/s^2]	520 in a_x
	100 in y			550 in a_y
	150 in z			310 in a_z
Rotation[$mrad$]	9 in ϕ	< 100	Torque per unit of inertia [$\mu rad/s^2$]	16 in γ_x
	5 in θ			24 in γ_y
	9 in η			13 in γ_z

Table 2.7.   HR mode characteristics in actuation and sensing

Measurement ranges	Performance range	Full/Sensing saturation range	Actuation authorities	Max
Linear [μm]	25 in x	> 2000	Force per unit mass [nm/s^2]	2.8 in a_x
	25 in y			3 in a_y
	25 in z			1.7 in a_z
Rotation[$mrad$]	2.5 in ϕ	< 100	Torque per unit of inertia [$nrad/s^2$]	29 in γ_x
	2 in θ			42 in γ_y
	2.5 in η			23 in γ_z

The ES authority is determined by the gap between the TM and the wall of the cage and by the voltage of the electrodes. In table 2.6 and table 2.7 are depicted two ranges in which the IS will actuate and sense the TM. The WR and HR can be defined respectively as a coarse and fine mode to control the TM. The two modes link sensing and actuation, i.e., if actuation is switched to WR mode, so is the sensing. Passing from WR to HR authority and noise on the measurements and on the actuation decreases as well.

The actuation noise in WR or HR mode is added to the output of F_E and M_E. Each noise is defined to be the output of a noise shape filter with the following transfer function in force and torque:

$$H_{WR,fx} = 6 \cdot 10^{-15} \frac{\left(s + 4\pi \cdot 10^{-5}\right)^2}{\left(s + \frac{4\pi}{\sqrt{600}} \cdot 10^{-5}\right)^2}$$

$$H_{WR,fy} = H_{WR,fz} = 5 \cdot 10^{-14} \frac{\left(s + 4\pi \cdot 10^{-5}\right)^2}{\left(s + \frac{4\pi}{\sqrt{2000}} \cdot 10^{-5}\right)^2}$$

$$H_{WR,t} = 5 \cdot 10^{-16} \frac{\left(s + 4\pi \cdot 10^{-5}\right)^2}{\left(s + \frac{4\pi}{\sqrt{600}} \cdot 10^{-5}\right)^2}$$

The HR mode presents the same transfer function but decreased by one order of magnitude, as showed in figure 2.10. Are showed in figure 2.11 the linear and angular sensing sensitivity for WR and HR mode, accordingly to the table 2.6 and 2.7
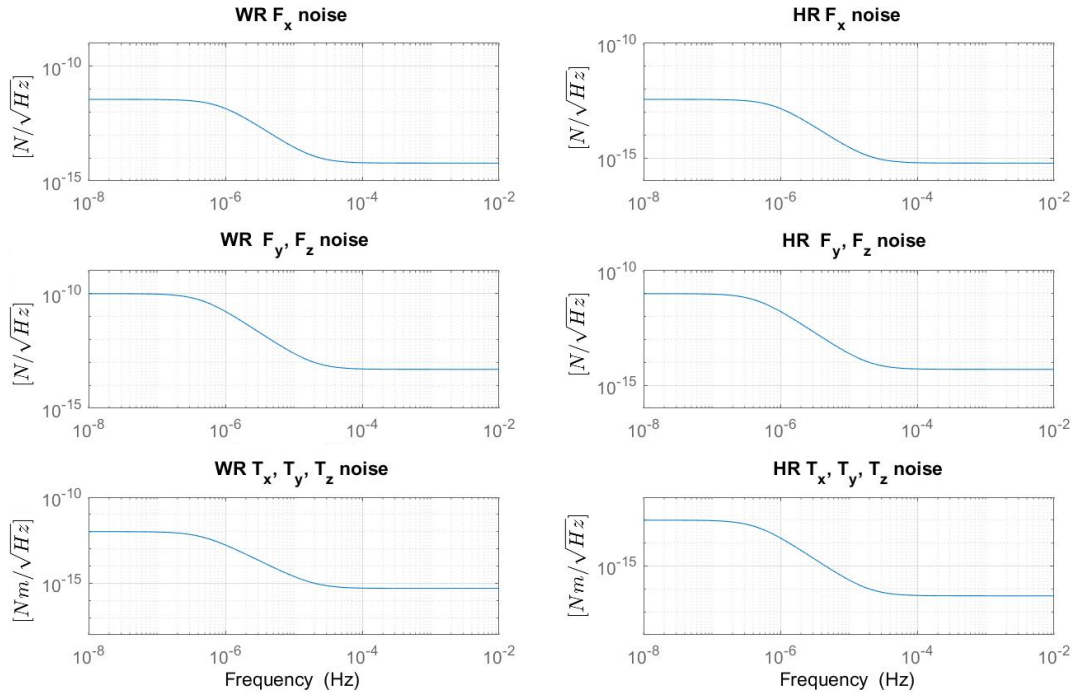
Figure 2.10.   WR and HR actuation noise shape filter.
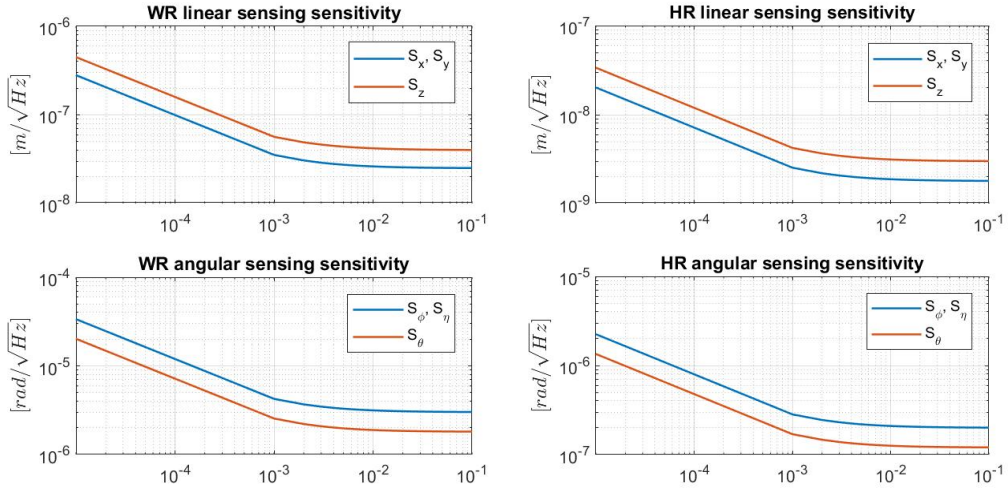
Figure 2.11.   WR and HR sensing noise shape filter.

33

2.4 Disturbances

In this section are discussed the main environmental disturbance acting on the S/C and on the TMs. It should be remarked that the external environmental disturbances will always act on the TM drag-free dynamics, since it is actually a relative motion between S/C and TM. Although small in terms of absolute value, disturbance torques act on each S/C of the constellation for all the time of the mission, thus producing in the long run a sizable displacement of the satellite from the desired attitude, if no proper compensating action is taken. Disturbances of different nature may affect spacecraft attitude. At the same time, internal sources of disturbances are also present, which either affect the dynamic behavior of the satellite with respect to the ideal one, or directly affect sensor pointing precision because of oscillations induced by flexible appendages or fuel sloshing. The major sources of external disturbances that may influence the dynamic behaviour of a satellite are:

- gravity gradient: the variation of gravity pull acting on different mass elements of the spacecraft provide a small yet significant torque;

- magnetic field: the satellite, with its metallic parts and currents flowing in the electric system produces a magnetic field that interacts with the external magnetic field;

- solar radiation: the solar radiation produce a light pressure force on the satellite parts exposed to the flow of nuclear particles emitted by the sun; again the force offset will determine a small torque, that would be insignificant in Earth missions, but is the main disturbance acting on the LISA mission.

Atmospheric and solar radiation torques depend strongly on the shape of the spacecraft, and in particular on how the solar panels and the spacecraft bus face the flow of the rarefied gas molecules or the stream of high energy particles from the Sun.

There are also some sources of internal disturbances, that can be due to the uncertainty of some parameters or to some simplifying assumptions the effect of which is not null on the actual spacecraft:

- uncertain center of gravity: there can be an uncertainty on the position of the center of gravity up to some centimeters;

- thruster misalignment: the direction of the thruster can be different from the design one up to 1 deg;

- run–run thrust variation: there can be sizable variation in the thrust produced by a thruster in different firings;

- fuel slosh: fuel sloshing in the propellant tanks causes both shift in the position of the center of mass and in the mass distribution (that is, affects the value of the moments of inertia); moreover, as propellant is burned, a long term variation in mean mass properties is also experienced by the satellite;

- rotating parts: rotating parts inside the satellite (gyroscopes, reaction wheels) produce microvibrations which in turn cause loss in pointing accuracy;

- elastic modes of flexible appendages: several flexible items, such as antennas, booms and solar arrays can be attached to the spacecraft bus, and their flexibility can interact with the rigid body motion of the main platform, resonating at the bending frequencies, if properly excited, with serious consequences for the pointing accuracy.

The main disturbance that acts directly on the S/C surface is the solar radiation pressure and its variation over time. The solar pressure is one of the biggest disturbances that act on the spacecraft. A simple model of the force generated by the solar pressure can be the following:

$$\mathbf{F}_{SP} = P_S c_{SP} S_{SC} \mathbf{n}_{SC}$$

where P_S is the solar pressure, $1 \leq c_{SP} \leq 2$ is the interaction coefficient, S_{SC} is the sun-facing area and $\mathbf{n}_{SC}$ is the unit vector from the spacecraft to the Sun CoM. This simple model appears to be reasonable, since LISA solar array shields the entire spacecraft. Anyway, a more complex plate-based model could be used:

$$\mathbf{F}_{SP} = -P_S \sum_{i=1}^{N} S_i \cos\theta_{SPi} \left[2\left(\frac{R_{diff,i}}{3} + R_{spec,i}\cos\theta_{SPi}\right) T_{SC}^I \mathbf{n}_{PL,i} + (1 - R_{spec,i})\mathbf{n}_{SC} \right]$$

$$\cos\theta_{SPi} = (T_{SC}^I \mathbf{n}_{PL,i}) \cdot \mathbf{n}_{SC}$$

wher $\mathbf{n}_{PL,i}$ is the unit vector normal to the i-th plate, and $R_{diff,i}$ and $R_{spec,i}$ are diffusion and reflection coefficients of the i-th plate. The solar pressure noise must be added in the model to account for indirect disturbances on the TM. Off course, the solar pressure is considered as a DC force and the variation of the solar flux is the changing parameter which determines the true noise on the S/C. From the pressure perspective, the solar flux$[W/m^2]$ is the driver of the noise phenomena [40]. One can obtain:

$$P_{SP} = (W_0 + \delta W)/a_l$$

where a_l is the speed of light, $W_0 = 1361 W/m^2$ is the DC value of the solar flux and δW is its variation depicted in figure 2.12 The spectrum used for the solar radiation flux variations is given in figure 2.12, based on [40] and is considered as a conservative assessment of potential

variations. The plot in figure indicates a constant spectrum at the frequencies below $0.1mHz$, followed by a $1/f$ roll off. This spectrum also includes the so-called 5 minutes acoustic oscillation (at $3.5mHz$), and levels off at frequencies above $10mHz$.
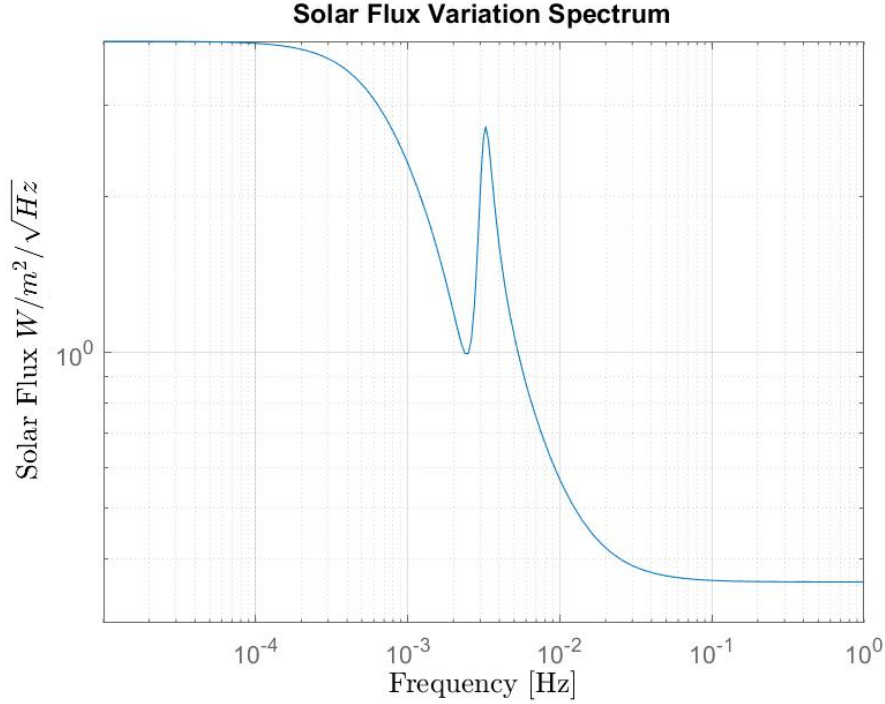
Figure 2.12.   Root Power Spectrum of the Solar Radiation Flux Variations.

To fully exploit the application of the LPF results to LISA, which has a 7 times more stringent requirement, it is necessary to remark two points. The first is the overall upper limit to stray force noise that LPF will provide, for any source of force noise, regardless of their origin or their inclusion in the noise budget. The second is the experimental assessment of the key parameters governing the dominant known noise sources, involving the space environment, the spacecraft hardware, and their interaction. In this following are given the current best estimate for how to set the estimated noise design for LISA.

It is extremely important to determine a reasonable model of the noise sources acting in every phase on the LISA TMs. A preliminary consideration may be done on the noise budget allocation. Compared to the requirements, all differential acceleration noise sources should be kept below 1 $fm/s^2/\sqrt{Hz}$ at $0.1mHz$, to keep the total sum below $3\sqrt{2}$ [41]. Gathering these information, a quantitative analysis of the excess noise detection and the noise parameter identification has been done and then applied to the LISA case.
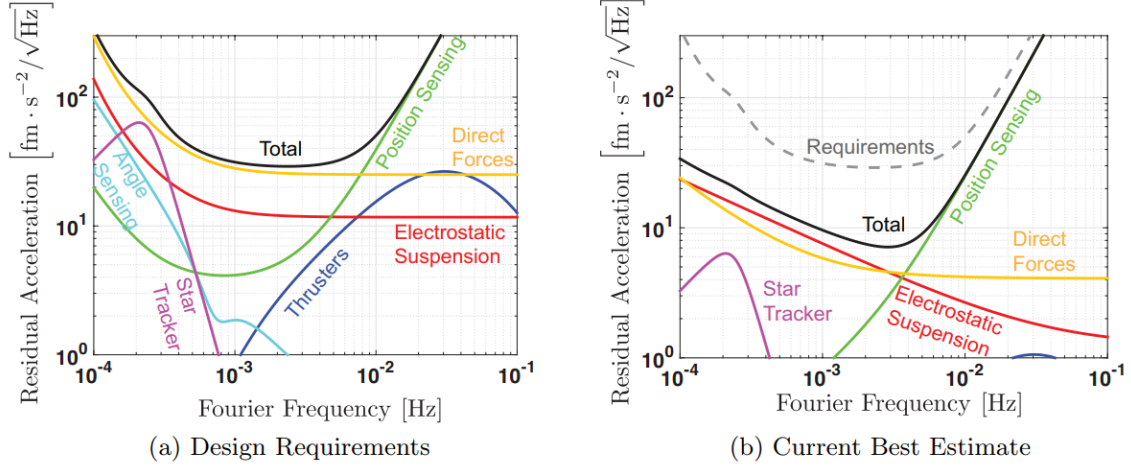
Figure 2.13. Design requirements (left) and Current best estimate (right) of the residual acceleration [52].

Pressure : The dominant noise source in the $1 - 10mHz$ band is due the so-called Brownian motion of residual gas particles trapped or outgassed in the housing. The phenomenon is naturally damped. Actually, its major disturbance effects are felt by the TMs immediately after the releasing and then, thanks to a quiet and cold environment, the gas entropy decreases. From LPF results has been highlithed that in one year the Brownian noise contribuscion decreased from 6 to $1.74\,\mathrm{f}m/s^2/\sqrt{Hz}$. Reducing gas damping differential acceleration noise, from LPF's 7 to below 2 $\mathrm{f}m/s^2/\sqrt{Hz}$ across the band in LISA will require reducing the gas pressure from $10^{-5}Pa$ to $5 \cdot 10^{-7}Pa$ or better. Moreover, is considered the laser radiation pressure. The same laser used to measure the position and the orientation of the TM acts on the measured coordinates.

Electro-Magnetics : Due to eddy currents, magnetic fields may generate acceleration disturbances. These noises can be compensated by using materials with low magnetic susceptibility, avoid the usage of permanent magnets and by placing sources of magnetic fields away from the electrode housing. Lorentz acceleration is present since the TMs are electrically charged bodies.

Thermal gradient effects : LISA will require that the temperature differences across the GRS be smaller than 10 $\mu K/\sqrt{Hz}$ to keep thermal gradient force noise below 1 $\mathrm{f}m/s^2/\sqrt{Hz}$, even with a small (25%) reduction in the coupling coefficient $dF/d\Delta T$, due to the drastically reduced role of the radiometric effect at the reduced LISA pressure.

Stray voltages and Random TM charging : Reducing the interaction of TM charge and

fluctuating electrostatic fields and the residual static potential imbalance will reduce these disturbances.

Self gravity : The gravitational forces that act on the two test masses must be compensated electrostatically and without using the suspension system along the sensitive axis. Since the design of LISA requires that all the spurious acceleration of the TMs must be kept below 3 f$m/s^2\sqrt{Hz}$, the gravitational effects must be considered. The three effects of the self-gravity are the static gravitational field, the gradient of the gravitational field and the fluctuations of the gravitational field. It should be noted that the gradient of the gravitational field is to all effects a stiffness, but even the pressure contributes to this negative stiffness in a minor way[43].

Table 2.8.   noise allocation

Source	Allocated disturbance
Pressure	0.65 f$m/s^2\sqrt{Hz}$
Electro-Magnetic	2.2 f$m/s^2\sqrt{Hz}$
Thermal	0.72 f$m/s^2\sqrt{Hz}$
Fluctuations of the gravitational field	0.5 f$m/s^2\sqrt{Hz}$
Static gravitational field	≤ 0.56 nm/s^2
Gradient of the gravitational field	≤ 400 ns^{-2}

The combination of the described disturbances can be grouped as a total TM acceleration variation, a stiffness matrix given by three contributions (magnetic, self-gravity and electrical) and a direct force term. The TM acceleration noise has been taken as follow

$$S_{TM}^{1/2} = 4\frac{fm/s^2}{\sqrt{Hz}}\sqrt{1 + \frac{3mHz}{f}}$$
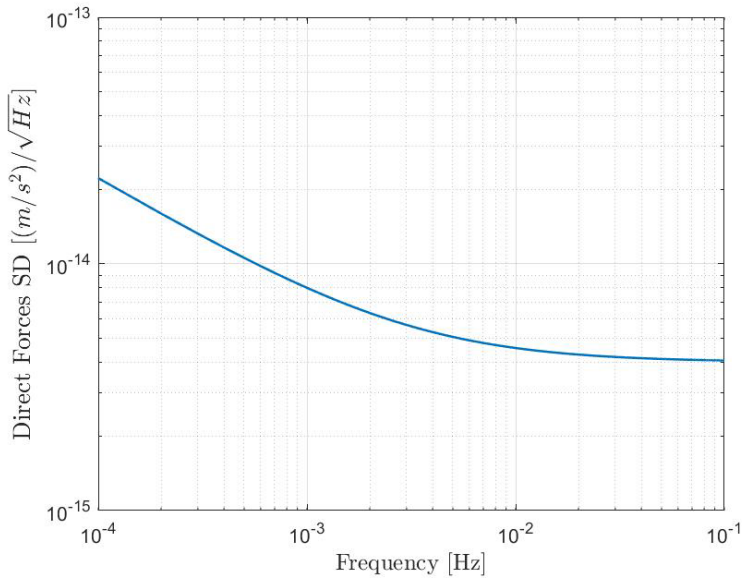
Figure 2.14.   Adopted residual acceleration on the TM.

2.5   Drag free control

In this section, a thorough review of the most relevant control system and performance requirements, affecting the final scientific performance, is presented.

Generally speaking, the preliminary set of requirements defined for the LISA control system have been developed in order to translate the mission objectives and scenario into a set of specifications applicable to the envisaged platform and its control subsystem. Hence, the control system requirements will be defined either in terms of what shall be accomplished by the control system itself (control system functional DF-F requirements), or considering how precisely such control functions or tasks should be achieved (control system performance DF-P requirements).

As a matter of fact, during the activities of this study great attention has been payed to the applicable requirements set. Indeed, the development, implementation, and test of a complete DFACS for the L3 mission will enable to perform a full set of consolidation activities of the control system requirements, preliminarily assumed as input of the study. To this aim, two main activities planned in the LISA study will undoubtedly support a thorough process of review and consolidation of the control requirements:

- the analysis of the several results (both simulated, ground testing, and in-flight) and lessons learnt from the Lisa Pathfinder mission,

39
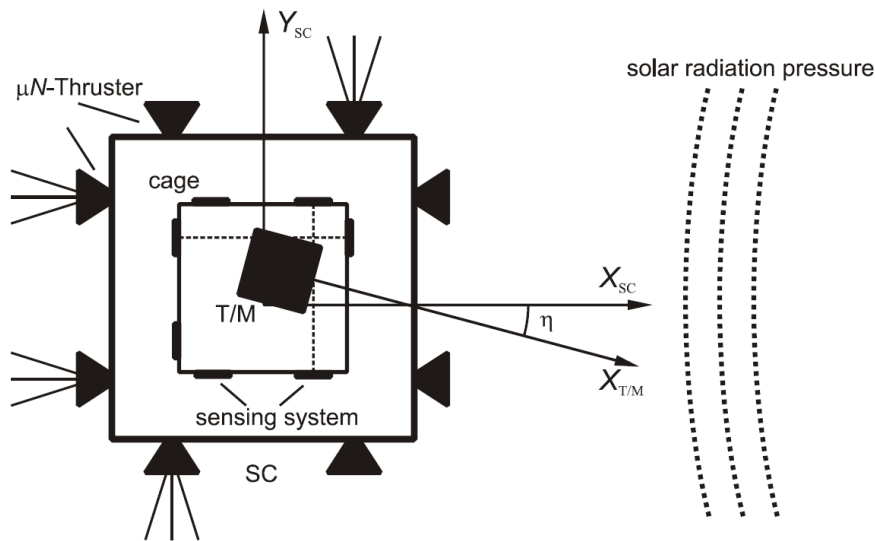
Figure 2.15.   General principle of a drag-free satellite, [10].

• the trade-off of different control system architectures and control design methodologies, as well as their implementation.

First of all, from the LPF perspective, several recent studies focused on the presentation of the most relevant results retrieved in the first part of the mission; often stressing the relationship and the lessons learnt in the future LISA perspective, for instance indicating what improvements, in hardware or testing methods, are necessary for LISA. Thus, the combination of the LPF experiments with laboratory measurements on ground will refine the known noise sources for LISA, in turn supporting the consolidation or modification of its requirement set with reduced risk and reasonable confidence.

Two further aspects will be of interest in the requirement consolidation process:

• The verification of the requirements consistency with the platform components and equipment (e.g. sensors, actuators, expected manoeuvres, etc.),

• The full supervision of the requirements status, also in preparation for the following mission and study phases (Phase A, etc.).

In the following, the preliminary control requirements will be reviewed and analyzed, also in relation with their context. Thus, each of them will be characterized by a specific number for traceability purposes, a brief summary, and a rationale.

The control system functional requirements intend to specify the main capabilities of the system, in terms of input, output, and behavior, and drive its architecture. As a result, the control system functional requirements allow to translate mission and system objectives into the following preliminary control objectives:

- DF-F-010
  The DFACS, in Science phase (starting after the constellation acquisition and the TMs release), shall be in charge of several control tasks in tight coordination:

  - S/C attitude (via MPS);

  - S/C relative position wrt TMs (via MPS);

  - S/C-to-S/C pointing, to enable laser interferometry (via MPS);

  - TMs electrostatic control (ensuring the free-falling conditions).

  Such a functional requirement is deemed to be fully compliant with the expected mission scenario and objective, as per [11], and it appears to be in line with DF-F-010, although at a higher-level.

- DF-F-020
  Given the micro-propulsion and the electrostatic actuations, the envisaged DFAC control tasks, as per DF-F-010, will require several sensors. This functional requirement comprehensively states the need of a proper network of sensors, ensuring that the S/C, the telescopes, and the TMs status is timely known, with proper accuracy and frequency.

- DF-F-030
  This functional requirement addresses more in detail the control tasks to be performed in LISA Science phase, coherently with DF-F-010. Specifically, concerning the S/C attitude control, it is conveniently specified that:

  - MPS shall be used;
  - the S/C attitude control shall be performed also when the test masses are still caged/grabbed;
  - the S/C attitude control shall be active also during orbit correction and/or decommissioning manoeuvres;
  - the S/C attitude control shall be active also during the TMs capture, after any release from the grabbed position;
  - the S/C attitude control shall be coordinate with the telescope attitude control, for constellation and drag-free condition maintenance purposes;

- the S/C attitude control shall be active also during the TMs position/attitude/drag-free control;

- the S/C attitude control shall be active also during the communication antenna re-pointing;

In addition, other DFACS functions shall be:

- the constellation acquisition, aiming at the laser pointing and bi-directional laser links acquisition;

- the telescopes attitude control, in tight coordination with the S/C one, in order to keep the constellation links, and electrostatic position/attitude control of the test masses;

- the telescope attitude control shall be active also during the TMs capture, after any release from the grabbed position;

- the telescope attitude control shall be active also during the TMs position/attitude/drag-free control;

- the telescope attitude control shall be active also during the communication antenna re-pointing;

- the TMs electrostatic capture, during any release from the grabbed configuration;

- the drag-free control, relatively to the necessary TMs DoFs;

- the position/attitude control of the TMs non-drag-free DoFs, via electrostatic actuation;

- the position/attitude control of the TMs DoFs, during the communication antenna re-pointing;

- the communication antenna pointing.

In addition, for test and calibration purposes, the Science mode should encompass the possibility to apply specific force or torque commands to the test masses. As a result, the DF-F-030 provides a sound boundary to the fields of applicability of the LISA DFACS.

- DF-F-040
  This functional requirement better clarifies the DFACS tasks, during the science measurement. Specifically, in order for the scientific retrieval could be performed, it is needed that:

  - the TMs are free-falling in the S/C-to-S/C LOS directions (2 drag-free DoFs);

- a third drag-free DoF might optionally included;

- the S/C relative attitude wrt the other S/C is zeroed, via DWS (laser) angular measurements;

- the inter-telescope angle control supports the S/C-to-S/C laser pointing;

- the TMs non-drag-free DoFs are controlled (attitude/position) wrt the cage and the S/C.

Moreover, although potentially encompassed by the above-mentioned point, DF-F-040 further points out the DFAC capability of ensuring a quiet and disturbance-free environment for LISA S/C, by calling for the need of compensating to the maximum extent the external environmental disturbances, namely the solar radiation pressure compensation.

From this perspective, the DF-F-040 figures out an open-loop compensation scenario. However, via a proper disturbance estimator and rejector, it is possible to endow the DFAC control unit with a full closed-loop compensation of the solar radiation pressure, as well as of any other possible external or internal disturbance, characterized by a frequency band coherent with the LISA science prescriptions.

- DF-F-050
The DF-F-050 concludes the list of functions to be carried out by the DFACS accounting for the FDIR concepts. Indeed, the DFACS should include some specific capability to monitor its status, and recover from potential failures, if needed. Although not a prescription, FDIR should not interfere with the LISA constellation laser links stability.

The control system functional requirements are completed by a full set of control system performance requirements. They are derived in tight coordination with the applicable system requirements, given the constraints imposed by other sub-system, and allocated to lower level requirements for the control components. Thus, the performance requirement to be met by the controlled system will apply either to the controller, or to sensors and actuators, or directly to the plant. From this perspective, a relevant activity within the requirement consolidation is the analysis and modeling of sensors and actuators, according to their specification, also ensuring that such specifications fit the expected control performance. As a final note, some of them can stem from other constraints than the control objectives (e.g. the controlled system verification). To sum up, the following control performance requirements are applicable to the study:

- DF-P-010
The first performance requirement defines the measurement frequency band applicable

for all performance requirements. Specifically, being the minimum bandwidth (MBW) required $f = \{0.1mHz, 0.1mHz\}$, the ideal MBW holds $f = \{0.02mHz, 1mHz\}$. Such a MBW interval is fully coherent with the typical measurement bands characterizing the gravity mission, also adopting laser interferometry, yet way more challenging wrt past missions. As a matter of fact, the capability to retrieve GW signal and source parameters with astrophysical relevant sensitivity in the selected band is consistent with the need to outperform the ground GW observatories capability, naturally limited by the seismic vibrations and other spurious noises. Further, the possibility to achieve the desired drag-free performance in the mentioned frequency band was, at least partially, tested by the LPF experiment, although with a scaled-down set of requirements and MBW [7].

Finally, the distinction between minimum and ideal requirements is supposed to streamline the effort of design and testing. Nevertheless, it is believed that the DFAC control architecture and configuration, if properly endowed with external and internal disturbance estimation and rejection capabilities, should be able to reach the ideal goal.

- DF-P-020
  The most relevant control performance quantity is defined via the DF-P-020, addressing the total effective displacement acceleration noise; in a one-way single TM-to-TM link (more precisely, TM-to-S/C + S/C-to-S/C + S/C-to-TM), coherently with the scientist retrieval need [11]. Such a key measurement performance requirement defines the strain sensitivity curve, and it is based on several main parameters:

  – Known acceleration noise sources (e.g. couplings, actuators, TM charge, magnetic effects, thermal gradients, etc.);

  – LISA and LPF simulation and experimental data (e.g. low-frequency unmodelled disturbances and noise sources).

  As a matter of fact, DF-P-020 limits the stray accelerations of the geodesic reference TM, thus it is mainly applicable to the GRS. As a result, the LPF experiment flight results supported the consolidation of the differential acceleration performance and the relevant requirement, with a little margin included [42] [7].

- DF-P-030
  The Test Mass position jitter is defined by DF-P-030, for what concerns the drag-free coordinates (S/C-to-S/C LOS directions). Although still in TBC format, the specified limit seems to be in line with the strawman system requirements for LISA, derived from the science requirements. Specifically, in line with the S/C errors consideration

(cf. DF-P-060), the major drivers affecting the test masses jitter requirement DF-P-030 are their acceleration noise, and the laser interferometer (IFO) cross coupling. From this perspective, limiting the TM displacement will enforce the IFO measure of the path-length variations caused by GWs, with the required accuracy.

- DF-P-040

  The Test Mass position jitter is defined by DF-P-040, for what concerns the non-drag-free coordinates (suspended directions), and in line with the S/C jitter set by DF-P-060. Also in this case, the specified limit seems to be in line with the strawman system requirements for LISA, derived from the science requirements, while the numerical value is relaxed (doubled, TBC) wrt to the drag-free directions figure. The above consideration about the major drivers affecting the test masses jitter requirement DF-P-030 do apply also for DF-P-040.

- DF-P-050

  In order to minimize the potential coupling effects of the S/C wrt the IFO readouts, DF-P-050 prescribe a proper limit to the TM angular error wrt to the reference attitude, coherently with the S/C angular jitter constrained by DF-P-080. Such requirement depicts in frequency the limits to the displacement noise of the IFO TM-to-TM ranging (one way, single TM-to-TM measurement). As a result, the requirement justification and further consolidation shall take into account, during the future phases of the LISA mission, the IFO assembly, including telescope and optical bench (OB), and their source of errors and noise. Interestingly, given the articulated nature of the TM-to-TM link (TM-to-S/C + S/C-to-S/C + S/C-to-TM), LPF demonstrated, with relevant margin, the TM-to-OB part of the requirement, whereas the S/C-to-S/C one was interested by the preliminary ground experiment; hence reminding the bottom-up approach to the requirements consolidation discussed above.

- DF-P-060

  The S/C position jitter is defined by DF-P-060, for what concerns the three coordinates. Also in this case, the specified limit seems to be in line with the strawman system requirements for LISA, derived from the science requirements. Specifically, the major drivers affecting the test masses jitter requirement DF-P-060 are their acceleration noise, and the laser interferometer (IFO) cross coupling. From this perspective, limiting the S/C displacement will enforce the IFO measure of the path-length variations caused by GWs, with the required accuracy.

- DF-P-070

  The spacecraft DC pointing accuracy is defined by DF-P-070 (3σ), in line with its

frequency behaviour in DF-P-080. In this case, the requirement is believed to establish a S/C DC mispointing coherently with the frequency limits set by DF-P-060, in order to minimise the coupling of the S/C attitude errors, mainly in terms of satellite-to-satellite pointing. Also in this case, the DC pointing accuracy is considered to be quite adequate to point the distant S/C, provided the beam opening angle, and quite conservative, thus taking into account possible optical, mounting, and alignment imperfections. Also the provided noise and errors level associated with the attitude pointing sensors support the consolidation of the DC pointing requirement DF-P-070. From this perspective, the high-fidelity simulation environment, accounting for the updated sensors and actuators package, shall be leveraged to further verify the pointing consistency with the IFO demands.

- DF-P-080

  The S/C angular jitter is defined by DF-P-080, for what concerns the three coordinates, in order to bind in frequency the potential coupling effects of the S/C wrt the IFO readouts. Regardless the final design S/C-to-S/C design, currently based on a controllable inter-telescope angle, the attitude error in DF-P-080 results to be compatible with the DC pointing accuracy level established by DF-P-070, and the need to enable the inter-satellite interferometry; provided the beam divergence angle produced by a 2.5 Mkm constellation arm-length, and the angular readouts of the incoming laser wavefront with respect to the local reference one, provided by the DWS sensors.

- DF-P-090

  The control performance requirement DF-P-090 calls for a controller stability modulus margin larger than 6 dB, although it is specified that, in Science mode, the key performance requirement DF-P-010 takes priority over such a value. Generally speaking, a gain margin stability value of 6 dB is quite a common and mainstream prescription for controllers, especially in linear and *Single-Input Single-Output* (SISO) design, together with a phase margin around 30 deg, to assess the relative stability of a closed-loop system. Hence, it can be accepted

Given the above listed requirements, both functional and performance, part of the consolidation study will focus on their verification and validation. As a matter of fact, starting the control verification during the earliest phase of the control design and prototyping, through iterative checks simulations and design re-adjustments, makes possible a more straightforward selection of the best technical solutions among the control system concepts. Of course, such an activity implies that a proper control verification strategy and process are chosen, consistently with the system verification plan.

Chapter 3

Mathematical models

3.1 Introduction
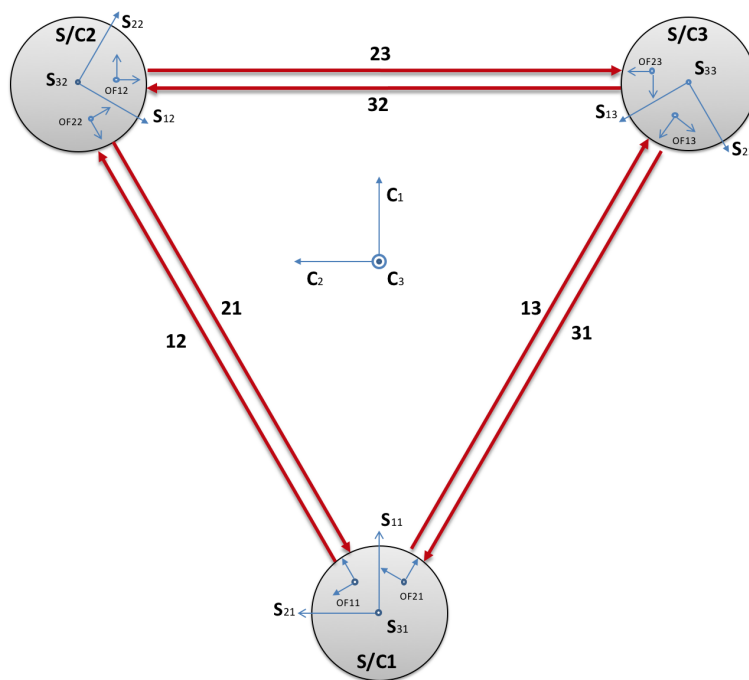
Figure 3.1. S/C and OA numbering convention.

In this chapter, will be showed the mathematical representation implemented in order to define a proper LISA simulator. To this aim, it is more useful to describe the dynamic of the single S/C that is part of the constellation. A relevant aspect of the treated problem is

the multibody dynamic. For what we said in the previous chapter, is not possible to treat the dynamic of each body (one spacecraft and two test masses) separately.

3.2 Nonlinear models of the relevant dynamics

In the following is presented the notation adopted in the context of mathematical modeling.

- Scalars: $a, b \in \mathbb{R}$.

- Column vectors:

$$\mathbf{r} = (r_1, \ldots, r_n) = [r_1 \ \ldots \ r_n]^T = \begin{bmatrix} r_1 \\ \vdots \\ r_n \end{bmatrix} \in \mathbb{R}^{n \times 1}.$$

- Row vectors: $\mathbf{r}^T = [r_1 \ \ldots \ r_n] \in \mathbb{R}^{1 \times n}$.

- Matrices: $M \in \mathbb{R}^{n \times m}$.

- Products:

$$\mathbf{r} \cdot \mathbf{p} = \mathbf{r}^T \mathbf{p} = \sum_{i=1}^{n} r_i p_i \qquad\qquad\qquad \text{dot product}$$

$$\mathbf{r} \times \mathbf{p} = \begin{bmatrix} 0 & -r_3 & r_2 \\ r_3 & 0 & -r_1 \\ -r_2 & r_1 & 0 \end{bmatrix} \begin{bmatrix} p_1 \\ p_2 \\ p_3 \end{bmatrix} = \begin{bmatrix} r_2 p_3 - r_3 p_2 \\ r_3 p_1 - r_1 p_3 \\ r_1 p_2 - r_2 p_1 \end{bmatrix} \qquad \text{cross product}$$

$$\mathbf{r} \times \;\doteq\; \begin{bmatrix} 0 & -r_3 & r_2 \\ r_3 & 0 & -r_1 \\ -r_2 & r_1 & 0 \end{bmatrix}.$$

- Vector ℓ_2 (Euclidean) norm:

$$|\mathbf{r}| = \|\mathbf{r}\| = \|\mathbf{r}\|_2 = \sqrt{\mathbf{r} \cdot \mathbf{r}} = \sqrt{\mathbf{r}^T \mathbf{r}} = \sqrt{\sum_{i=1}^{n} r_i^2} = r.$$

- $\Lambda(\omega) \equiv \Lambda(J, \omega) \doteq -J^{-1} \omega \times J \omega.$

- $\Omega \equiv \Omega(\omega) \doteq \omega \times \omega \times + \dot{\omega} \times.$

- T_a^b: rotation matrix RFb –> RFa (coordinate transformation RFa –> RFb). A rotation matrix can be expressed in function of the corresponding quaternion as

$$T \equiv T(\mathfrak{q}) = \begin{bmatrix} q_0^2 + q_1^2 - q_2^2 - q_3^2 & 2(q_1 q_2 - q_0 q_3) & 2(q_1 q_3 + q_0 q_2) \\ 2(q_1 q_2 + q_0 q_3) & q_0^2 - q_1^2 + q_2^2 - q_3^2 & 2(q_2 q_3 - q_0 q_1) \\ 2(q_1 q_3 - q_0 q_2) & 2(q_2 q_3 + q_0 q_1) & q_0^2 - q_1^2 - q_2^2 + q_3^2 \end{bmatrix}.$$

- Elementary rotation matrices:

$$X(\phi) \doteq \begin{bmatrix} 1 & 0 & 0 \\ 0 & c\phi & -s\phi \\ 0 & s\phi & c\phi \end{bmatrix} \quad \begin{array}{l} \text{rotation about } X \\ \text{through an angle } \phi \end{array}$$

$$Y(\theta) \doteq \begin{bmatrix} c\theta & 0 & s\theta \\ 0 & 1 & 0 \\ -s\theta & 0 & c\theta \end{bmatrix} \quad \begin{array}{l} \text{rotation about } Y \\ \text{through an angle } \theta \end{array}$$

$$Z(\psi) \doteq \begin{bmatrix} c\psi & -s\psi & 0 \\ s\psi & c\psi & 0 \\ 0 & 0 & 1 \end{bmatrix} \quad \begin{array}{l} \text{rotation about } Z \\ \text{through an angle } \psi \end{array}$$

where $c \equiv \cos$ and $s \equiv \sin$.

- Rotation Matrix derivatives:

$$\dot{T}_a^b = T_a^b \omega \times$$
$$\dot{T}_b^a = -\omega \times T_b^a$$

where ω is the angular velocity vector of RFa wrt RFb with components expressed in RFa.

- Quaternions: $\mathfrak{q} = (q_0, \mathbf{q}) = \begin{bmatrix} q_0 \\ \mathbf{q} \end{bmatrix}$, $q_0 \in \mathbb{R}$, $\mathbf{q} \in \mathbb{R}^{3 \times 1}$.

- $\mathfrak{q} \oplus \mathfrak{p}$: quaternion product.

- $\mathfrak{q} \oplus \omega$: quaternion product between a quaternion $\mathfrak{q}$ and a quaternion where the first component is 0 and the other three are given by ω.

- Euler angles kinematics matrix (Tait-Bryan 321):

$$Q(\boldsymbol{\theta}) \doteq \frac{1}{c\theta} \begin{bmatrix} c\theta & s\phi\,s\theta & c\phi\,s\theta \\ 0 & c\phi\,c\theta & -s\phi\,c\theta \\ 0 & s\phi & c\phi \end{bmatrix}$$

where $\boldsymbol{\theta} = (\psi, \theta, \phi)$, $c \equiv \cos$ and $s \equiv \sin$.

- Quaternion kinematics matrix:

$$Q(\mathfrak{q}) \doteq \begin{bmatrix} -q_1 & -q_2 & -q_3 \\ q_0 & -q_3 & q_2 \\ q_3 & q_0 & -q_1 \\ -q_2 & q_1 & q_0 \end{bmatrix}.$$

49

3.2.1 Main variables and parameters

It is now presented the convention used for each optical assembly in the relative S/C and the convention of each S/C in the formation flight. As showed in figure 3.1, the S/C numbering increases clockwise. The S/C are denoted with S/C_n, where $i = 1,2,3$ is the index of the spacecraft. Laser links are (i,j) labeled, since the laser beam goes from spacecraft i to spacecraft j.

In figure 3.2 are depicted the two optical assemblies. Each OA is characterized by a longitudinal axis, individuated by the line of sight of the optical sensor intercepting the incoming laser beam. The longitudinal axes of the two optical assemblies of a S/C define a plane, called the optical plane. The optical assemblies are denoted with OA_{nm}, where n is the number of the spacecraft and m is the number of the laser beam. Practically, $m = 1$ if a clockwise laser beam is transmitted and $m = 2$ if a counterclockwise laser beam is transmitted. In short, we indicate OA_m as the m-th optical assemly of the generic S/C.
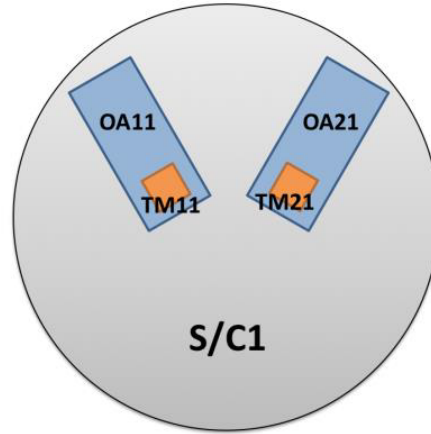
Figure 3.2.   Single S/C convention.

As showed in figure 2.9, inside each OA there is the corresponding test mass. The TMs are denoted with TM_{np}, where n is the number of the S/C, p is the number of the OA that hosts the TM. So, $p = 1$ if the test mass is housed inside the first optical assembly and $p = 2$ if the test mass is housed inside the second optical assembly.

Finally, the formation flight is composed by 3 spacecrafts with a total of 6 optical assemblies and 6 test masses.

Considering the single S/C we can distinguish between actuated and non actuated degrees of freedom (DoF).

S/C the system groups 7 DoFs, 3 linear position of the S/C, 3 attitude angles. The 3 attitude

angles of the S/C are always actuated in order to maintain the pointing to the other S/Cs and the 3 linear positions are actuated for drag-free purposes only and not for constellation control.

OAs only one is the DoF that the system can control. With a first simplification it can be assumed that the angle actuation for the OAs of the same S/C are equal and opposite, reducing the breathing angle to a single controlled DoF.

TMs with a total of 6 linear positions (actuated), 6 attitude angles (actuated) wrt the housing. During the science measurement phase, the 6 TM positions are arranged into 3 drag-free coordinates (2 longitudinal and the mean vertical coordinate of the TM pair) and 3 suspension coordinates (2 lateral and the difference between the vertical coordinates). The 3 DF coordinates are actuated together with the S/C attitude by 9 thrusters of the *Micro-N Propulsion Assembly* (MPA), the 3 suspension coordinates are actuated by 4 suspension actuators. The spacecraft z axis is commanded to follow the average of both TMs z coordinate in a "drag-free" loop in order to reduce the electrostatic actuation applied to both TM z axis. This will reduce the coupling noise contributions from electrostatic z actuation into both sensitive axes.

Besides the mere distinction between controlled and free DoF, it must be cleared the modes in which these are controlled or left free. Three main modes can be cited and discussed:

Attitude control : In this mode the DFACS shall force the single S/C attitude to a declared attitude. Since the first attitude acquisition do not require any particular condition for the TMs, these can remain grabbed inside the housing. Anyway, the release of the TMs must be performed to trigger the constellation acquisition. Still in this mode the TM can be mechanically captured in order to re-establish the initial configuration.

Constellation Acquisition : At this point the TMs are released and controlled with the electrostatic suspension system in all the coordinates. The S/C shall follow a search sequence to find and hook the laser of the other S/Cs.

Science : The constellation should be now locked onto the combination of the laser of both arms. The science measurements can start.

In the table 3.2 are reported the modes definition with the corresponding controlled DoFs.

It should be noted that in science mode only the interferometric axes are left free. Actually, the compensation of the mean vertical displacement of the two TMs does not necessarily leads to the shutdown of the capacitors normal to the z axis but only to their command output reduction.

Table 3.1.   DFACS modes definition

Controlled system	Controlled DoFs	Attitude Control	Constellation Acquisition	Science Mode
TM	All Coord (12)	×	×	
	Susp Coord (10)			×
SC	Inertial Attitude (3)	×	×	×
	Relative Position (3)			×
OA	Breathing angle (1)		×	×
	Total DoFs	**15**	**16**	**17**

It is worth to recall how the cited DoFs are sensed and actuated. The variable symbols will be defined below

Table 3.2.   Coordinates relation with sensors and actuators

Body	Variable name	Symbol	Sensor	Actuator
TM	Relative position	$\mathbf{r}_M$	IS/OMS	ES/MPA/IT
	Relative attitude	$\mathfrak{q}_M$	IS/OMS	ES/MPA/IT
SC	Inertial Attitude	$\mathfrak{q}_{SI}$	STR/CAS/OMS*	MPA
OA	Breathing angle	ζ	CAS/OMS	IT

The Reference Frames used for the mathematical modeling procedure are now presented.

Inertial Frame (IF) $\{O_I; \vec{I}_1, \vec{I}_2, \vec{I}_3\}$ has the origin in the Sun CoM and the first two axes lie on the ecliptic plane and the third is chosen in order to obtain a counterclockwise rotation of the constellation.

Constellation Frame (CF) $\{O_c; \vec{c}_1, \vec{c}_2, \vec{c}_3\}$ has the origin in the nominal triangle center and its basic plane $\{\vec{c}_1, \vec{c}_2\}$ contains all the CoMs of the three S/C and its normal vector points toward the Sun.

Local Constellation Frame (CF$_i$) $\{O_{ci}; \vec{c}_{1i}, \vec{c}_{2i}, \vec{c}_{3i}\}$ where $i = 1,2,3$ is the number of the S/C$_i$, has the origin in the S/C$_i$ CoM and $\vec{c}_{1i}$ is the bisector of the two constellation arms starting from the S/C$_i$ CoM.

Spacecraft Frame (SF) $\{O_{Si}; \vec{s}_{1i}, \vec{s}_{2i}, \vec{s}_{3i}\}$ has the origin in the CoM of the S/C$_i$ and $\{\vec{s}_{1i}, \vec{s}_{2i}\}$ lie in the optical plane defined by the telescope optical axes and $\vec{s}_{1i}$ s is the bisector of the two telescope optical axes.

Optical assembly Frame (OF$_{ji}$) $\{O_{Oji}; \vec{o}_{1ji}, \vec{o}_{2ji}, \vec{o}_{3ji}\}$ where $j = 1,2$ is the number of the OA in the S/C$_i$ has the origin in the CoM of the OA$_{ji}$, $\{\vec{o}_{1ji}, \vec{o}_{2ji}\}$ are on the optical

plane previously defined and $\vec{o}_{1ji}$ is the telescope optical axis. The OA is able to rotate around the $\vec{o}_{3ji}$ so that it can be assume to always have $\vec{o}_{3ji}$ parallel to $\vec{s}_{3ji}$.

Test mass Frame (TF$_{ji}$) $\{O_{mji}; \vec{m}_{1ji}, \vec{m}_{2ji}, \vec{m}_{3ji}\}$ has the origin in the CoM of the TM$_{ji}$ and $\vec{m}_{1ji}$ is orthogonal to the positive x face of the TM and $\vec{m}_{3ji}$ is orthogonal to the positive z face of the TM. To better visualize the presented reference frames refer to figures 3.3 and 3.4.

When referring to the generic S/C$_i$, OA$_{ji}$ or TM$_{ji}$ the subscripts j, i will be omitted.
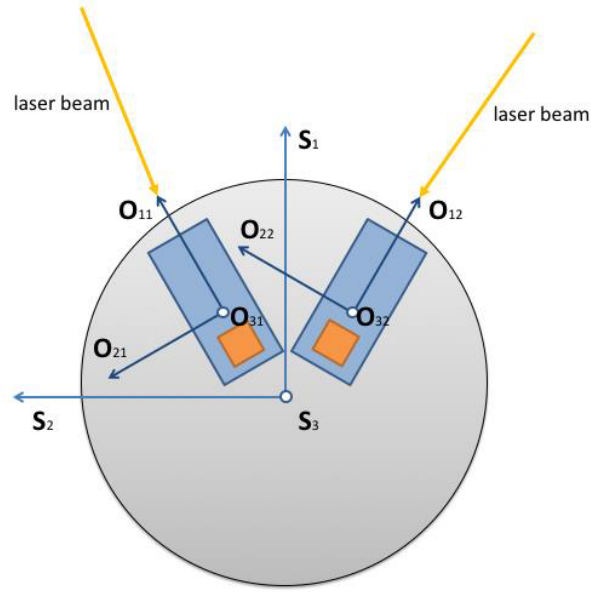
Figure 3.3.   Optical Reference frames. Unit vectors (usually denoted with an arrow) are here denoted with the bold style.

In the following, we will mainly refer to generic S/C, OA and TM. Hence, in order to simplify the notation, the indexes i and j denoting the S/C, the OA and the TM will be omitted, if not strictly necessary. Below is the list of the main variables and parameters used in this proposal, indicating also the reference frame in which the vector components are expressed.

Main variables

- $\mathbf{r}_I$: S/C CoM position wrt the IF origin - components in IF

- $\mathbf{r}_M$: TM CoM position wrt the cage center - components in OF

- $\mathbf{r}_M^I$: TM CoM position wrt the cage center - components in IF
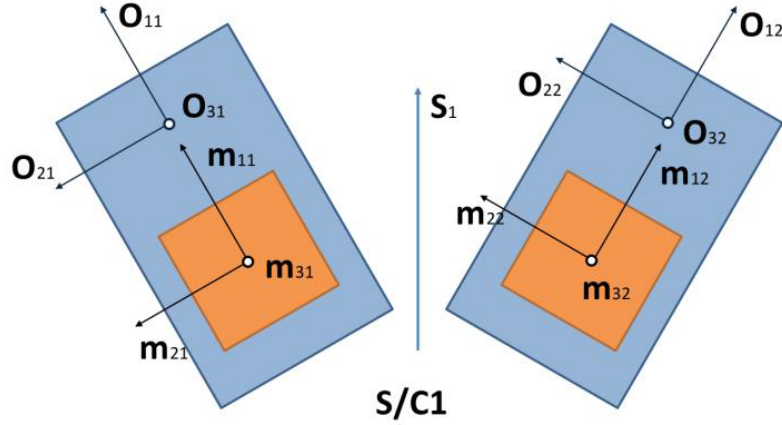
Figure 3.4. Test mass and optical assembly reference frames. Unit vectors (usually denoted with an arrow) are here denoted with the bold style.

- $\mathbf{r}_{MI}$: TM CoM position wrt the IF origin - components in IF

- q_S: quaternion of the rotation CF –> SF

- q_{SI}: quaternion of the rotation IF –> SF

- q_ζ: quaternion of the rotation SF –> OF

- q_M: quaternion of the rotation OF –> MF

- $\boldsymbol{\theta}_S$: Euler angle vector of the rotation CF–> SF

- $\boldsymbol{\theta}_M$: Euler angle vector of the rotation OF –> MF

- $\boldsymbol{\omega}_S$: S/C angular velocity wrt CF - components in SF

- $\boldsymbol{\omega}_{SI}$: S/C angular velocity wrt IF - components in SF

- $\boldsymbol{\omega}_O$: OA angular velocity wrt IF - components in OF

- $\boldsymbol{\omega}_M$: TM angular velocity w.r.t. OF - components in MF

- $\boldsymbol{\omega}_{MI}$: TM angular velocity w.r.t. IF - components in MF

- $\boldsymbol{\omega}_C$: CF origin angular velocity wrt IF - components in CF

- ζ: OF angle with respect to its rest position (the rest positions of the two OFs x-axes are given by the SF x-axis $\pm \pi/6$)

- γ: OF angle with respect to SF

- $\boldsymbol{\omega}_\zeta \doteq (0,0,\dot{\zeta})$, $\boldsymbol{\omega}_\gamma \doteq (0,0,\dot{\gamma})$

- $\boldsymbol{\alpha}_\zeta \doteq (0,0,\ddot{\zeta})$, $\boldsymbol{\alpha}_\gamma \doteq (0,0,\ddot{\gamma})$

Command inputs

- $\mathbf{F}_T$: MPA commanded force - components in SF

- $\mathbf{F}_E$: suspension force - components in OF

- $\mathbf{M}_T$: MPA torque - components in SF

- $\mathbf{M}_E$: suspension torque - components in OF

- $\mathbf{u}_{EF}, \mathbf{u}_{EM}$: suspension digital commands

- u_{OA}: OA command

Disturbances

- $\mathbf{d}_S$: force disturbance acting on a S/C - components in SF

- $\mathbf{d}_M$: force disturbance acting on a TM - components in OF

- $\mathbf{D}_S$: torque disturbance acting on a S/C - components in SF

- $\mathbf{D}_M$: torque disturbance acting on a TM - components in MF

- d_ζ: OA motor noise

Parameters

- m_S: S/C mass (including the two OAs)

- m_M: TM mass

- J_S: S/C inertia matrix w.r.t its CoM (including the two OAs)

- $\mathbf{b}_S$: vector from the S/C CoM to the OA pivot - components in SF

- $\mathbf{b}_M$: vector from the OA pivot to the cage center - components in OF

- $\mathbf{b} \equiv \mathbf{b}_S + T_O^S \mathbf{b}_M$: vector from the S/C CoM to the cage center - components in SF

- c_{OA}: OA input coefficient

- p_i: OA parameters

55

3.3 LISA nonlinear models

The dynamic models (equations of motion) for the various elements composing the LISA observatory are now reported.

The equations have been derived by means of the Newton-Euler approach. The command inputs and disturbances are treated as generic signals.

The models are written for generic S/C, OA and TM. The index $j \in \{1,2\}$ (denoting the OA and the TM) will be used only when necessary, otherwise it will be omitted. The convention for the symbols $\pm$ and $\mp$ is the following:

$$\pm = \begin{cases} + & if\ j = 1 \\ - & if\ j = 2 \end{cases}$$

$$\mp = \begin{cases} - & if\ j = 1 \\ + & if\ j = 2. \end{cases}$$

S/C rotation model

The angular velocity and acceleration of the S/C wrt CF are given by

$$\omega_S = \omega_{SI} - T_C^S \omega_C$$
$$\dot{\omega}_S = \dot{\omega}_{SI} - \dot{T}_C^S \omega_C - T_C^S \dot{\omega}_C = \alpha_{SI} + \omega_S \times T_C^S \omega_C - T_C^S \alpha_C.$$

The angular acceleration $\alpha_{SI} \equiv \dot{\omega}_{SI}$ is obtained from the Euler equation

$$\dot{\omega}_{SI} = \Lambda(\omega_{SI}) + J_S^{-1} \left(\mathbf{M}_T + \mathbf{D}_S - \sum_{i=1,2} \left(T_{Oi}^S \mathbf{M}_{Ei} + \mathbf{b}_i \times T_{Oi}^S \mathbf{F}_{Ei} \right) \right).$$

The rotational dynamics of the S/C wrt CF is described by the following equations:

$$\dot{\omega}_S = \alpha_{SI} + \alpha_{SR}$$

$$\alpha_{SI} = \Lambda(\omega_{SI}) + J_S^{-1} \left(\mathbf{M}_T + \mathbf{D}_S - \sum_{i=1,2} \left(T_{Oi}^S \mathbf{M}_{Ei} + \mathbf{b}_i \times T_{Oi}^S \mathbf{F}_{Ei} \right) \right)$$

$$\alpha_{SR} = \omega_S \times T_C^S \omega_C - T_C^S \alpha_C$$
$$\omega_{SI} = \omega_S + T_C^S \omega_C.$$

The rotation matrices are

$$T_{Oi}^S = Z(\gamma_i)$$
$$T_C^S = T(\mathfrak{q}_S^*)$$

where

$$\gamma_i = \begin{cases} \pi/6 + \zeta, & i = 1 \\ -\pi/6 - \zeta, & i = 2. \end{cases}$$

The attitude quaternion and Euler angles are given by the standard kinematic equations:

$$\dot{\mathfrak{q}}_S = \frac{1}{2}\mathfrak{q}_S \oplus \omega_S$$

$$\dot{\boldsymbol{\theta}}_S = Q(\boldsymbol{\theta}_S)\omega_S.$$

OA rotation model

A simple linear second-order model is considered for the OA rotation:

$$\ddot{\zeta} = -p_1\dot{\zeta} - p_2\zeta + c_{OA}u_{OA} + d_\zeta.$$

The OA angles wrt the S/C are given by γ_j (defined above). The following angular velocity and acceleration vectors can also be defined:

$$\omega_{\gamma j} = (0,0,\dot{\gamma}_j)$$

$$\alpha_{\gamma j} = (0,0,\ddot{\gamma}_j).$$

TM translation model

Relative acceleration in IF –> relative acceleration in OF

The following kinematic relations hold for a generic TM:

$$\mathbf{r}_M^I = T_O^I \mathbf{r}_M$$

$$\begin{aligned}
\dot{\mathbf{r}}_M^I &= \dot{T}_O^I \mathbf{r}_M + T_O^I \dot{\mathbf{r}}_M \\
&= T_O^I \omega_O \times \mathbf{r}_M + T_O^I \dot{\mathbf{r}}_M
\end{aligned}$$

$$\begin{aligned}
\ddot{\mathbf{r}}_M^I &= \dot{T}_O^I \omega_O \times \mathbf{r}_M + T_O^I \dot{\omega}_O \times \mathbf{r}_M + T_O^I \omega_O \times \dot{\mathbf{r}}_M + \dot{T}_O^I \dot{\mathbf{r}}_M + T_O^I \ddot{\mathbf{r}}_M \\
&= T_O^I \omega_O \times \omega_O \times \mathbf{r}_M + T_O^I \dot{\omega}_O \times \mathbf{r}_M + 2T_O^I \omega_O \times \dot{\mathbf{r}}_M + T_O^I \ddot{\mathbf{r}}_M.
\end{aligned}$$

It follows that

$$\begin{aligned}
\ddot{\mathbf{r}}_M &= T_I^O \ddot{\mathbf{r}}_M^I - (\omega_O \times \omega_O \times + \dot{\omega}_O \times)\mathbf{r}_M - 2\omega_O \times \dot{\mathbf{r}}_M \\
&= T_I^O \ddot{\mathbf{r}}_M^I - \Omega(\omega_O)\mathbf{r}_M - 2\omega_O \times \dot{\mathbf{r}}_M.
\end{aligned}$$

The equation for the jth TM is

$$\ddot{\mathbf{r}}_{Mj} = T_I^{Oj} \ddot{\mathbf{r}}_{Mj}^I - \Omega(\omega_{Oj})\mathbf{r}_{Mj} - 2\omega_{Oj} \times \dot{\mathbf{r}}_{Mj}$$
$$= \mathbf{a}_{Rj} - \Omega(\omega_{Oj})\mathbf{r}_{Mj} - 2\omega_{Oj} \times \dot{\mathbf{r}}_{Mj}$$

where $\mathbf{a}_{Rj} \doteq T_I^{Oj} \ddot{\mathbf{r}}_{Mj}^I$.

Absolute acceleration in IF –> relative acceleration in IF

The following kinematic relations hold for a generic TM:

$$\mathbf{r}_{MI} = \mathbf{r}_I + T_S^I \mathbf{b}_S + T_O^I \mathbf{b}_M + \mathbf{r}_M^I$$
$$\mathbf{r}_M^I = \mathbf{r}_{MI} - \mathbf{r}_I - T_S^I \mathbf{b}_S - T_O^I \mathbf{b}_M = \Delta\mathbf{r}_I - T_S^I \mathbf{b}_S - T_O^I \mathbf{b}_M$$

where $\Delta\mathbf{r}_I \doteq \mathbf{r}_{MI} - \mathbf{r}_I$. The first and second time derivatives of $\mathbf{r}_M^I$ are given by

$$\dot{\mathbf{r}}_M^I = \Delta\dot{\mathbf{r}}_I - \dot{T}_S^I \mathbf{b}_S - \dot{T}_O^I \mathbf{b}_M = \Delta\dot{\mathbf{r}}_I - T_S^I \omega_{SI} \times \mathbf{b}_S - T_O^I \omega_O \times \mathbf{b}_M$$

$$\ddot{\mathbf{r}}_M^I = \Delta\ddot{\mathbf{r}}_I - \dot{T}_S^I \omega_{SI} \times \mathbf{b}_S - T_S^I \dot{\omega}_{SI} \times \mathbf{b}_S - \dot{T}_O^I \omega_O \times \mathbf{b}_M - T_O^I \dot{\omega}_O \times \mathbf{b}_M$$
$$= \Delta\ddot{\mathbf{r}}_I - T_S^I(\omega_{SI} \times \omega_{SI} \times + \dot{\omega}_{SI} \times)\mathbf{b}_S - T_O^I(\omega_O \times \omega_O \times + \dot{\omega}_O \times)\mathbf{b}_M$$
$$= \Delta\ddot{\mathbf{r}}_I - T_S^I \Omega(\omega_{SI})\mathbf{b}_S - T_O^I \Omega(\omega_O)\mathbf{b}_M.$$

The equation for the jth TM is

$$\ddot{\mathbf{r}}_{Mj}^I = \Delta\ddot{\mathbf{r}}_{Ij} - T_S^I \Omega(\omega_{SI})\mathbf{b}_{Sj} - T_{Oj}^I \Omega(\omega_{Oj})\mathbf{b}_M.$$

It follows that

$$\mathbf{a}_{Rj} \doteq T_I^{Oj} \ddot{\mathbf{r}}_{Mj}^I = T_I^{Oj} \Delta\ddot{\mathbf{r}}_{Ij} - T_S^{Oj} \Omega(\omega_{SI})\mathbf{b}_{Sj} - \Omega(\omega_{Oj})\mathbf{b}_M$$
$$= \mathbf{a}_{Nj} - T_S^{Oj} \Omega(\omega_{SI})\mathbf{b}_{Sj} - \Omega(\omega_{Oj})\mathbf{b}_M$$

where $\mathbf{a}_{Nj} \doteq T_I^{Oj} \Delta\ddot{\mathbf{r}}_{Ij}$.

Newton's laws

According to the Newton's laws, we have that

$$\ddot{\mathbf{r}}_{MIj} = -\mu_\odot \frac{\mathbf{r}_{MIj}}{\left|\mathbf{r}_{MIj}\right|^3} + m_M^{-1} T_{Oj}^I(\mathbf{F}_{Ej} + \mathbf{d}_{Mj})$$
$$\ddot{\mathbf{r}}_I = -\mu_\odot \frac{\mathbf{r}_I}{\left|\mathbf{r}_I\right|^3} + m_S^{-1} T_S^I(\mathbf{F}_T + \mathbf{d}_S) - m_S^{-1} \sum_{i=1,2} T_{Oi}^I \mathbf{F}_{Ei}.$$

Hence,

$$\Delta\ddot{\mathbf{r}}_{Ij} = K_\Delta \Delta\mathbf{r}_{Ij} + m_M^{-1} T_{Oj}^I(\mathbf{F}_{Ej} + \mathbf{d}_{Mj}) - m_S^{-1} T_S^I(\mathbf{F}_T + \mathbf{d}_S) + m_S^{-1} \sum_{i=1,2} T_{Oi}^I \mathbf{F}_{Ei}$$

where

$$K_\Delta \Delta \mathbf{r}_{Ij} \cong -\mu_\odot \left(\frac{\mathbf{r}_{MIj}}{|\mathbf{r}_{MIj}|^3} - \frac{\mathbf{r}_I}{|\mathbf{r}_I|^3} \right)$$

is the gravity gradient. Since

$$\Delta \mathbf{r}_{Ij} \doteq \mathbf{r}_{MIj} - \mathbf{r}_I = T_S^I \mathbf{b}_{Sj} + T_{Oj}^I \mathbf{b}_M + \mathbf{r}_{Mj}^I$$

the equation for $\Delta \ddot{\mathbf{r}}_{Ij}$ can be written as

$$\Delta \ddot{\mathbf{r}}_{Ij} = K_\Delta (T_S^I \mathbf{b}_{Sj} + T_{Oj}^I \mathbf{b}_M) + K_\Delta T_{Oj}^I \mathbf{r}_{Mj} + m_M^{-1} T_{Oj}^I (\mathbf{F}_{Ej} + \mathbf{d}_{Mj}) - m_S^{-1} T_S^I (\mathbf{F}_T + \mathbf{d}_S) + m_S^{-1} \sum_{i=1,2} T_{Oi}^I \mathbf{F}_{Ei}.$$

It follows that

$$\begin{aligned}
\mathbf{a}_{Nj} &\doteq T_I^{Oj} \Delta \ddot{\mathbf{r}}_{Ij} \\
&= T_I^{Oj} K_\Delta (T_S^I \mathbf{b}_{Sj} + T_{Oj}^I \mathbf{b}_M) + T_I^{Oj} K_\Delta T_{Oj}^I \mathbf{r}_{Mj} \\
&\quad + m_M^{-1}(\mathbf{F}_{Ej} + \mathbf{d}_{Mj}) - m_S^{-1} T_S^{Oj}(\mathbf{F}_T + \mathbf{d}_S) + m_S^{-1} \sum_{i=1,2} T_{Oi}^{Oj} \mathbf{F}_{Ei} \\
&= \mathbf{u}_{bj} + S_{TT} \mathbf{r}_{Mj} + S_{TR} \mathbf{q}_{Mj} + m_M^{-1}(\mathbf{F}_{Ej} + \mathbf{d}_{Mj}) - m_S^{-1} T_S^{Oj}(\mathbf{F}_T + \mathbf{d}_S) + m_S^{-1} \sum_{i=1,2} T_{Oi}^{Oj} \mathbf{F}_{Ei}.
\end{aligned}$$

The equations of the jth TM translation motion, relative to the cage center, are the following:

$$\begin{aligned}
\ddot{\mathbf{r}}_{Mj} &= \mathbf{a}_{Rj} - \Omega(\omega_{Oj})\mathbf{r}_{Mj} - 2\omega_{Oj} \times \dot{\mathbf{r}}_{Mj} \\
\mathbf{a}_{Rj} &= \mathbf{a}_{Nj} - T_S^{Oj}\Omega(\omega_{SI})\mathbf{b}_{Sj} - \Omega(\omega_{Oj})\mathbf{b}_M \\
\mathbf{a}_{Nj} &= \mathbf{d}_{gj} + S_{TT}\mathbf{r}_{Mj} + S_{TR}\mathbf{q}_{Mj} + m_M^{-1}(\mathbf{F}_{Ej} + \mathbf{d}_{Mj}) - m_S^{-1}T_S^{Oj}(\mathbf{F}_T + \mathbf{d}_S) + m_S^{-1}\sum_{i=1,2} T_{Oi}^{Oj}\mathbf{F}_{Ei} \\
\omega_{Oj} &= T_S^{Oj}\omega_{SI} + \omega_{\gamma j} \\
\mathbf{d}_{gj} &= T_I^{Oj} K_\Delta T_S^I \mathbf{b}_{Sj} + T_I^{Oj} K_\Delta T_{Oj}^I \mathbf{b}_M
\end{aligned}$$

where S_{TT} and S_{TR} are stiffness matrices, accounting for gravity gradient and self gravity effects, and other forces proportional to displacements. The quantity $\Omega(\omega_{Oj})$ is given by

$$\Omega(\omega_{Oj}) \doteq \omega_{Oj} \times \omega_{Oj} \times + \dot{\omega}_{Oj} \times$$

where

$$\begin{aligned}
\dot{\omega}_{Oj} &= \dot{T}_S^{Oj}\omega_{SI} + T_S^{Oj}\alpha_{SI} + \alpha_{\gamma j} \\
&= -\omega_{\gamma j} \times T_S^{Oj}\omega_{SI} + T_S^{Oj}\alpha_{SI} + \alpha_{\gamma j}.
\end{aligned}$$

The rotation matrices are

$$T_S^{Oj} = Z(-\gamma), \ j = 1,2$$
$$T_{O1}^{O2} = Z(2\gamma)$$
$$T_{O2}^{O1} = Z(-2\gamma).$$

TM rotation model

The angular velocity and acceleration of the TM wrt OF are given by

$$\omega_{Mj} = \omega_{MIj} - T_{Oj}^{Mj} \omega_{\gamma j} - T_S^{Mj} \omega_{SI}$$
$$\dot{\omega}_{Mj} = \dot{\omega}_{MIj} - \dot{T}_{Oj}^{Mj} \omega_{\gamma j} - T_{Oj}^{Mj} \alpha_{\gamma j} - \dot{T}_S^{Mj} \omega_{SI} - T_S^{Mj} \dot{\omega}_{SI}$$
$$= \alpha_{MIj} + \omega_{Mj} \times T_{Oj}^{Mj} \omega_{\gamma j} - T_{Oj}^{Mj} \alpha_{\gamma j} + \left(T_{Oj}^{Mj} \omega_{\gamma j} + \omega_{Mj} \right) \times T_S^{Mj} \omega_{SI} - T_S^{Mj} \alpha_{SI}.$$

The angular acceleration $\alpha_{MIj} \equiv \dot{\omega}_{MIj}$ is obtained from the Euler equation

$$\alpha_{MIj} = \Lambda(\omega_{MIj}) + S_{RT} \mathbf{r}_{Mj} + S_{RR} \mathbf{q}_{Mj} + J_M^{-1} \left(T_{Oj}^{Mj} \mathbf{M}_{Ej} + \mathbf{D}_{Mj} \right).$$

The rotational dynamics of the *j*th TM wrt OF is described by the following equations:

$$\dot{\omega}_{Mj} = \alpha_{MIj} + \alpha_{MRj}$$
$$\alpha_{MIj} = \Lambda(\omega_{MIj}) + S_{RT} \mathbf{r}_{Mj} + S_{RR} \mathbf{q}_{Mj} + J_M^{-1} \left(T_{Oj}^{Mj} \mathbf{M}_{Ej} + \mathbf{D}_{Mj} \right)$$
$$\alpha_{MRj} = \omega_{Mj} \times T_{Oj}^{Mj} \omega_{\gamma j} - T_{Oj}^{Mj} \alpha_{\gamma j} + \left(T_{Oj}^{Mj} \omega_{\gamma j} + \omega_{Mj} \right) \times T_S^{Mj} \omega_{SI} - T_S^{Mj} \alpha_{SI}$$
$$\omega_{MIj} = \omega_{Mj} + T_{Oj}^{Mj} \omega_{\gamma j} + T_S^{Mj} \omega_{SI}$$

where S_{RR} and S_{RT} are stiffness matrices, accounting for all forces proportional to displacements. The rotation matrices are

$$T_{Oj}^{Mj} = T(\mathfrak{q}_M^*)$$
$$T_S^{Mj} = T_{Oj}^{Mj} T_S^{Oj} = T(\mathfrak{q}_M^*) Z(-\gamma_j).$$

The attitude quaternion and Euler angles are given by the standard kinematic equations:

$$\dot{\mathfrak{q}}_{Mj} = \frac{1}{2} \mathfrak{q}_{Mj} \oplus \omega_{Mj}$$
$$\dot{\theta}_{Mj} = Q(\theta_{Mj}) \omega_{Mj}.$$

Electrostatic suspension model

A simplified noise-free static model is the following:

$$\begin{bmatrix} \mathbf{F}_E \\ \mathbf{M}_E \end{bmatrix} = \begin{bmatrix} A_{EF} & A_{MF} \\ A_{FM} & A_{EM} \end{bmatrix} \begin{bmatrix} \mathbf{r}_M \\ \theta_M \end{bmatrix} + \begin{bmatrix} B_{EF} & B_{MF} \\ B_{FM} & B_{EM} \end{bmatrix} \begin{bmatrix} \mathbf{u}_{EF} \\ \mathbf{u}_{EM} \end{bmatrix}.$$

3.4   Linear models of the relevant dynamics

The derivation of the linear equations can be found in the Appendix. Neglecting second order and higher order terms of the nonlinear equations, small perturbations and disturbances, the linearized dynamic equations can be written as follows:

$$\dot{\omega}_S = J_S^{-1}\mathbf{M}_T - J_S^{-1}\bar{\mathbf{b}}_1 \times \bar{T}_{O1}^S \mathbf{F}_{E1} - J_S^{-1}\bar{T}_{O1}^S \mathbf{M}_{E1} - J_S^{-1}\bar{\mathbf{b}}_2 \times \bar{T}_{O2}^S \mathbf{F}_{E2} - J_S^{-1}\bar{T}_{O2}^S \mathbf{M}_{E2}$$

$$\dot{\mathbf{v}}_{M1} = S_{TT}\mathbf{r}_{M1} + S_{TR}\mathbf{q}_{M1} - m_S^{-1}\bar{T}_S^{O1}\mathbf{F}_T + \left(m_M^{-1} + m_S^{-1}\right)\mathbf{F}_{E1} + m_S^{-1}\bar{T}_{O2}^{O1}\mathbf{F}_{E2}$$

$$\dot{\omega}_{M1} = S_{RT}\mathbf{r}_{M1} + S_{RR}\mathbf{q}_{M1} + J_M^{-1}\bar{T}_{O1}^{M1}\mathbf{M}_{E1}$$

$$\dot{\mathbf{v}}_{M2} = S_{TT}\mathbf{r}_{M2} + S_{TR}\mathbf{q}_{M2} - m_S^{-1}\bar{T}_S^{O2}\mathbf{F}_T + m_S^{-1}\bar{T}_{O1}^{O2}\mathbf{F}_{E1} + \left(m_M^{-1} + m_S^{-1}\right)\mathbf{F}_{E2}$$

$$\dot{\omega}_{M2} = S_{RT}\mathbf{r}_{M2} + S_{RR}\mathbf{q}_{M2} + J_M^{-1}\bar{T}_{O2}^{M2}\mathbf{M}_{E2}$$

$$\dot{\omega}_\zeta = -p_1\dot{\zeta} - p_2\zeta + c_{OA}u_{OA} + d_\zeta.$$

The linearized kinematic equations are

$$\dot{\mathbf{q}}_S = \omega_S/2$$

$$\dot{\mathbf{r}}_{M1} = \mathbf{v}_{M1}$$

$$\dot{\mathbf{q}}_{M1} = \omega_{M1}/2$$

$$\dot{\mathbf{r}}_{M2} = \mathbf{v}_{M2}$$

$$\dot{\mathbf{q}}_{M2} = \omega_{M2}/2$$

$$\dot{\zeta} = \omega_\zeta$$

where $\mathbf{q}$ is the quaternion vector part. The real part is obtained by normalization.

The following relations hold:

$$\bar{T}_{O1}^{M1} = I$$

$$\bar{T}_{O1}^{M1} = I$$

$$\bar{T}_{O1}^S = Z(\pi/6)$$

$$\bar{T}_{O2}^S = Z(-\pi/6)$$

$$\bar{T}_{O1}^{O2} = Z(\pi/3).$$

3.4.1   Linearized state equation

Let us define the following state and command vectors:

$$\mathbf{x} \doteq (\mathbf{q}_S, \mathbf{r}_{M1}, \mathbf{q}_{M1}, \mathbf{r}_{M2}, \mathbf{q}_{M2}, \omega_S, \mathbf{v}_{M1}, \omega_{M1}, \mathbf{v}_{M2}, \omega_{M2}) \in \mathbb{R}^{30\times1}$$

$$\mathbf{u} \doteq (\mathbf{F}_T, \mathbf{M}_T, \mathbf{f}_{E1}, \mathbf{M}_{E1}, \mathbf{f}_{E2}, \mathbf{M}_{E2}) \in \mathbb{R}^{16\times1}$$

where

$$\mathbf{f}_{Ej} = P\mathbf{F}_{Ej} \in \mathbb{R}^{2\times 1}, \quad P \doteq \begin{bmatrix} 0 & 1 & 0 \\ 0 & 0 & 1 \end{bmatrix}.$$

The linearized state equation is

$$\dot{\mathbf{x}} = \begin{bmatrix} \mathbf{0} & A_K \\ A_V & \mathbf{0} \end{bmatrix} \mathbf{x} + \begin{bmatrix} \mathbf{0} \\ B_V \end{bmatrix} \mathbf{u}$$

where

$$A_K \doteq \begin{bmatrix} I/2 & \mathbf{0} & \mathbf{0} & \mathbf{0} & \mathbf{0} \\ \mathbf{0} & I & \mathbf{0} & \mathbf{0} & \mathbf{0} \\ \mathbf{0} & \mathbf{0} & I/2 & \mathbf{0} & \mathbf{0} \\ \mathbf{0} & \mathbf{0} & \mathbf{0} & I & \mathbf{0} \\ \mathbf{0} & \mathbf{0} & \mathbf{0} & \mathbf{0} & I/2 \end{bmatrix} \in \mathbb{R}^{15\times 15}$$

$$A_V \doteq \begin{bmatrix} \mathbf{0} & \mathbf{0} & \mathbf{0} & \mathbf{0} & \mathbf{0} \\ \mathbf{0} & S_{TT} & S_{TR} & \mathbf{0} & \mathbf{0} \\ \mathbf{0} & S_{RT} & S_{RR} & \mathbf{0} & \mathbf{0} \\ \mathbf{0} & \mathbf{0} & \mathbf{0} & S_{TT} & S_{TR} \\ \mathbf{0} & \mathbf{0} & \mathbf{0} & S_{RT} & S_{RR} \end{bmatrix} \in \mathbb{R}^{15\times 15}$$

$$B_V \doteq \begin{bmatrix} \mathbf{0} & J_S^{-1} & -J_S^{-1}\bar{\mathbf{b}}_1 \times \bar{T}_{O1}^S P^T & -J_S^{-1}\bar{T}_{O1}^S & -J_S^{-1}\bar{\mathbf{b}}_2 \times \bar{T}_{O2}^S P^T & -J_S^{-1}\bar{T}_{O2}^S \\ -m_S^{-1}\bar{T}_S^{O1} & \mathbf{0} & \left(m_M^{-1}+m_S^{-1}\right)P^T & \mathbf{0} & m_S^{-1}\bar{T}_{O2}^{O1}P^T & \mathbf{0} \\ \mathbf{0} & \mathbf{0} & \mathbf{0} & J_M^{-1} & \mathbf{0} & \mathbf{0} \\ -m_S^{-1}\bar{T}_S^{O2} & \mathbf{0} & m_S^{-1}\bar{T}_{O1}^{O2}P^T & \mathbf{0} & \left(m_M^{-1}+m_S^{-1}\right)P^T & \mathbf{0} \\ \mathbf{0} & \mathbf{0} & \mathbf{0} & \mathbf{0} & \mathbf{0} & J_M^{-1} \end{bmatrix} \in \mathbb{R}^{15\times 16}.$$

3.5 Nonlinear dynamics discussion and main design drivers

The nonlinear model derivation and its consequent linearization, certainly, led to a more direct understanding of the nature of the system taken into account. In the previous chapter we considered the definition of the external disturbances acting on S/C and TMs and determination of the hardware (sensor and actuators) noise. Although this is process is necessary, it is not sufficient to extrapolate a faithful behavior of the real case. Initial state, parametric uncertainty and neglected dynamics can be considered in the control design process in order to ensure the robustness of the control. However, these other uncertainties are not treated in this work.

A decoupling analysis of the equation in the previous section has been done in order to deconstruct the complexity of the system. As said in [9] the original idea to decouple the system equation was developed in the framework of LPF. Even if eLISA and LPF have the same principal mission objective, the mission architecture leads to different decoupling analysis. For the sake of simplicity, we can get to write the overall dynamics as the parallel of 15 SISO systems (has been excluded the OA DoF), where each variable is controlled by at least a single independent command input. On the basis of this analysis, considering also the control authorities of the available command inputs, it is possible, for each variable (or group of variables), to choose which command inputs are used for its control. According to [9], control during the science mode of the LISA mission can be performed effectively by means of three loops:

S/C attitude loop based on the Euler attitude equation, it shall be controlled with the MPS for slew to target and fine pointing.

TMs attitude and position loop rigid body dynamic controlled by the ES in order to center the TM in the housing.

DF loop couples the TMs and the S/C in a isolated relative motion perspective .

In figure 3.5 are presented the decoupled loops. The configuration holds if and only if the cross-coupling terms between the different loops can be neglected. This can be ensured by a wisely choice of the bandwidths of the three loops. At this point, the choice is not arbitrary, but constrained by many aspects related to the system.
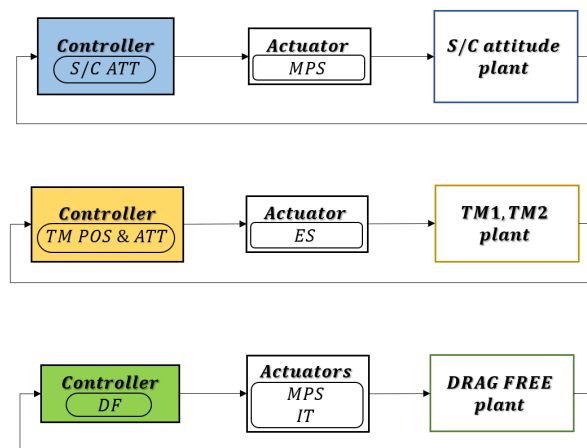
Figure 3.5.   Closed-loop structure.

Since the S/C attitude and the drag-free loops are both actuated by the MPS, the thrust noise level and the thrust update rate (see table 2.5) can be considered as bounding drivers for the controllers. In a preliminary study, the lower bound will drive the gain/phase margin of the control loops and in order to meet the requirements, the drag-free control must be endowed with the widest possible BW, followed by the S/C attitude BW. Similarly, for the suspension control loop a minimum bandwidth is required in order to stabilize the test masses against the negative stiffness in the plant. An upper bound can be placed due to the necessity of limiting the cross-talk effects of the ES actuation into the sensitive axis. The control loop design will be discussed in the next chapter.

Chapter 4

Control system design

4.1 Overview

The typical purpose of putting a satellite into orbit is to point an instrument at something. In the case of the LISA mission the pointing not only aims at two moving targets, but more, requires an inner control of the pointer. As a matter of fact, the desired pointing accuracy can only be achieved by keeping in mind the loops in the dynamic of the satellite [45] [44]. As said before, three major control areas can be identified [9]:

- The spacecraft and telescope pointing control

- The drag-free control of the proof masses

- The electrostatic suspension control of the proof masses

This implies that the attitude of the spacecraft must be stabilized to the desired attitude compatible with the pointing requirements. Moreover, the relative drag-free position between the spacecraft and the test masses and in general the position and the orientation of the test masses must be controlled to make the mission to succeed. The decoupling analysis carried out in the previous chapter has been useful to understand the relevant dynamics of the system with studies on the whole and the single loops. In this sense, each loop can be seen separately from the others as long as the distance in bandwidth between the loops is satisfying. After this substantial simplification of the dynamics, many approaches can be used to design a proper controller. Off course, the choice of the controller is strongly driven by the requirements. A key element of the control design process is how we specify the desired performance of the system. Inevitably the design process requires a trade-off between different features of the closed loop system and specifications are the mechanism by which we describe the desired

65

outcome of those trade-offs. The majority of the performance specifications are expressed as frequency domain specifications and so they can be better included in the design of a frequency domain based controller (e.g. PID, H_∞) via loop shaping.

The dynamic relation between the output $y(s)$ and the control input $u(s)$ and disturbances $d(s)$ can be expressed in the classical notation as

$$y(s) = G(s)u(s) + G_d(s)d(s)$$
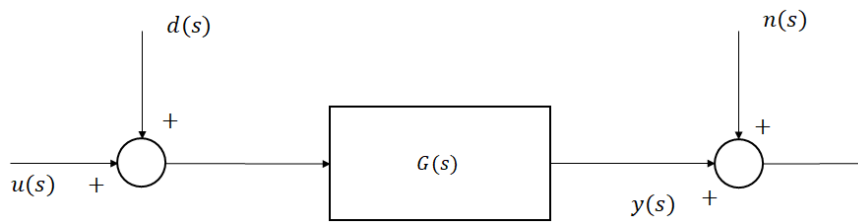
Figure 4.1. Block diagram of the open-loop system.

where $G(s)$ is the system transfer function related to the control path and $G_d(s)$ is the system transfer function of the disturbance path. Note that, for the cases treated in this work, $G(s) = G_d(s)$ since we have assumed the disturbance input acting on the plant as the control input. Note also that the system output is typically measured with a sensor which is affected by noise. A usual scheme implies that the noise $n(s)$ is added to the system output $y(s)$. We can write the noisy measure is

$$y_n(s) = G(s)u(s) + G_d(s)d(s) + n(s)$$
$$= G(s)\Big(u(s) + d(s)\Big) + n(s)$$

Our preliminary and general purpose is to design a control system for each loop capable to meet the requirements and to prove the feasibility of the mission itself. Note that the satisfaction of the single loop requirements does not necessarily leads to the meeting of the overall requirements. In the case of the attitude loop, pointing accuracy is the major driver but every command given as input to the attitude plant will return as disturbance to the other plants.

The result of a properly design of a feedback controller will lead to the block diagram reported in figure 4.2, where $K(s)$ is the transfer function of the controller. Generally speaking, any feedback control system determined by the closed-loop design process should exhibit the following properties:

- Closed-loop stability

- Capability to follow the reference signal with prescribed static and dynamic performance

- Capability of rejecting disturbance

- Capability of rejecting measurement noise

- Robustness against model uncertainties

Stability, reference tracking (static and dynamic), disturbance rejection, noise rejection and robustness are qualities characteristics of control scheme. The quantities that can be associated to each concept will define the performance of the system in time and frequency domain. Using a loop shaping approach, all these concepts can be taken into account and so treated as requirements to be met. According to the typical closed-loop scheme, the control law can be written in the Laplace domain as

$$u(s) = K(s)e(s)$$

where

$$e(s) = r(s) - [y(s) + n(s)]$$

is the output error. Therefor, the system output is written as

$$y(s) = G(s)K(s)e(s) + G(s)d(s)$$
$$= G(s)K(s)[r(s) - y(s) - n(s)] + G(s)d(s)$$
$$= \frac{K(s)G(s)}{1 + K(s)G(s)}r(s) - \frac{K(s)G(s)}{1 + K(s)G(s)}n(s) + \frac{G(s)}{1 + K(s)G(s)}d(s)$$
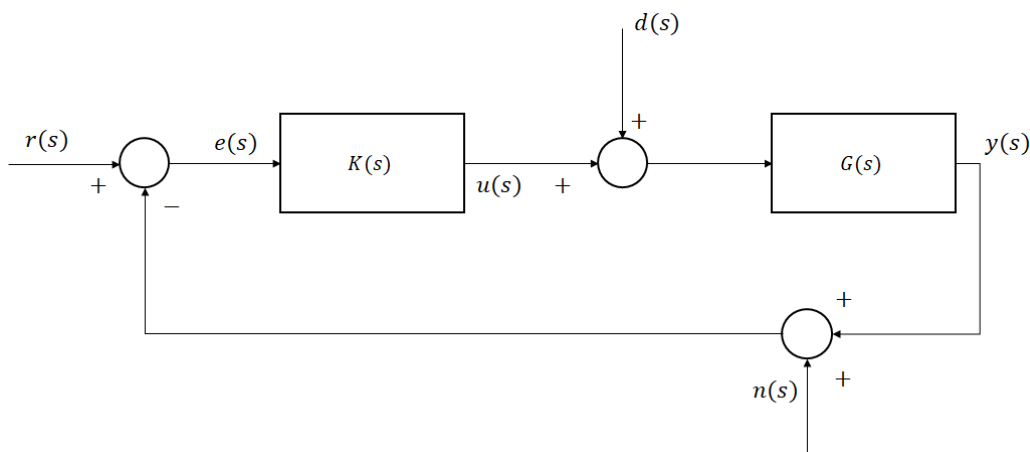
Figure 4.2.   Block diagram of the closed-loop system.

and taking the so-called *loop transfer function* as $L(s) = K(s)G(s)$, we have

$$y(s) = \frac{L(s)}{1 + L(s)} r(s) - \frac{L(s)}{1 + L(s)} n(s) + \frac{G(s)}{1 + L(s)} d(s) \qquad (4.1)$$

where it is clear that the output dynamics is characterized by the following, actually two transfer function:

- $\frac{L(s)}{1+L(s)}$ which is the *complementary sensitivity function $T(s)$*

- $\frac{1}{1+L(s)}$ which is the *sensitivity function $S(s)$*

In terms of the error between the reference and the system output, we have

$$
\begin{aligned}
e(s) &= r(s) - y(s) \\
&= \frac{1}{1 + L(s)} r(s) - \frac{G(s)}{1 + L(s)} d(s) + \frac{L(s)}{1 + L(s)} n(s)
\end{aligned}
\qquad (4.2)
$$

The *complementary sensitivity function* and *sensitivity function* are related by the following equation

$$T(s) + S(s) = 1 \qquad (4.3)$$

In the case of a real system with disturbances and noises as reported in figure 4.3, the *loop transfer function $L(s)$* is by definition the product of all the transfer function in the loop:

$$L(s) = K(s)G_a(s)G(s)G_s(s)$$

but the (4.3) must always hold.
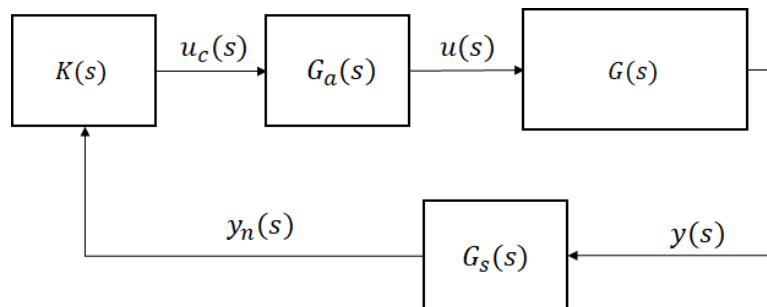
Figure 4.3.   Block diagram of the closed-loop system with sensor and actuator.

It is clear that a controller must be chosen to obtain the desired loop function even when the measurements and the actuation are corrupted. The feedback loop in figure 4.2 is influenced by three external signals, the reference r , the load disturbance d and the measurement noise

n. There are at least three signals, y, y_n and u that are of great interest for control, giving nine relations between the input and the output signals. Since the system is linear, these relations can be expressed in terms of the transfer functions in a general matrix of 9 elements. To avoid a long mathematical treatment we can discuss in the present study the characteristics of the complementary sensitivity and sensitivity function.

4.2 Shaping design guidelines

The equations (4.1) and (4.2) represent the key relationships for the design of a feedback control system. Before proceeding with control solutions, let discuss the general design guidelines to be followed in order to achieve the closed-loop requirements declared previously via shaping transfer functions. In this approach the designer specifies the magnitude of some transfer function(s) as a function of frequency, and then finds a controller which gives the desired shape(s). The open-loop characteristics are firstly shaped. Usually no optimization is involved and the designer aims to obtain $|L(j\omega)|$ with desired bandwidth, slopes etc. However, classical loop shaping is difficult to apply for complicated systems, and one may then instead use the (Glover-McFarlane) H_∞ loop shaping design which method consists of a second step where optimization is used to make an initial loop-shaping design more robust. In addiction, the closed-loop transfer functions, such as $S(s)$ and $T(s)$ are taken into account, better if the process is now driven by a tailor made optimization process.

First of all, we must ensure the stability of the closed-loop system. The stability can be checked in different ways and the method used can highlight in different ways how much a system is stable or unstable. It is easy to prove that the closed-loop poles are the roots of the following equation

$$1 + L(s) = 0$$

which represents the common denominator of the sensitivity functions of the system. The controller must be selected in such a way that all the poles given by the equation are placed in the left half complex plane, i.e., real part of the closed-loop poles must be negative. A more graphical technique to prove the stability of the system is the Nyquist stability theorem. It allows to determine the stability of a dynamical system without explicitly computing the poles and zeros of either the closed-loop or open-loop system (although the number of each type of right-half-plane singularities must be known). Once the stability is ensured, the ideal control system would be such that the output y matches perfectly the reference r. This goal should be achieved along with good rejection of disturbance and measurement noise. To this

aim, referring to eq (4.1) we require that

$$\frac{L(s)}{1 + L(s)} \to 1 \quad \text{for reference tracking}$$
$$\frac{G(s)}{1 + L(s)} \to 0 \quad \text{for disturbance rejection} \quad (4.4)$$
$$\frac{L(s)}{1 + L(s)} \to 0 \quad \text{for noise rejection}$$

By referring to eq (4.2), perfect tracking implies also that

$$\frac{1}{1 + L(s)} \to 0$$
$$\frac{G(s)}{1 + L(s)} \to 0 \quad (4.5)$$
$$\frac{L(s)}{1 + L(s)} \to 0$$

Good reference tracking is possible with complementary sensitivity function $T(s) \approx 1$ and sensitivity function $S(s) \approx 0$. This is also completely compatible with relation (4.3). Furthermore, the above requirements on the sensitivity functions leads to a good disturbance rejection of the closed-loop system. Therefore, good reference tracking can be achieved along with good disturbance rejection by taking large loop function at any frequency ω which characterizes the reference and disturbances signals, i.e.,

$$|L(j\omega)| \gg 1 \quad \text{(good reference tracking and disturbance rejection)}$$

The drawback of this choice lies in the complete lack of noise rejection capabilities. Indeed, good noise rejection is achieved by taking small values of the loop function, i.e.,

$$|L(j\omega)| \ll 1 \quad \text{(good noise rejection)}$$

The above requirements are clearly in contrast. It means that good tracking, disturbance rejection and noise rejection cannot be simultaneously met at all frequencies. Fortunately, a satisfactory design can be generally achieved since the frequency content of the reference and disturbance signal typically well separated from the frequency content of the measurement noise. In most applications, both reference and external disturbances vary relatively slow in time, so that their characteristic frequency content is in the low frequency range. On

the contrary, the noise arising from sensors typically vary rapidly with time, that is, it is characterized by high frequencies. Therefore, the design should be performed such that

$$|L(j\omega)| \gg 1 \quad \text{over the appropriate } low\ frequency\ range$$

$$|L(j\omega)| \ll 1 \quad \text{over the appropriate } high\ frequency\ range$$

In other words, closed-loop tracking and disturbance rejection requirements place lower-bound restrictions on the modulus of the loop function $L(s)$ at low frequencies, whereas measurement noise attenuation requirements place upper-bound restrictions on the modulus of the loop function in the high frequency range. An example based on the conclusions made until now is given in figure 4.4. It is implied in the characteristics of the shaped loop function that the log-plot of the magnitude must cross at least one time the zero-dB axis. The lowest crossing frequency is typically called gain cross-over frequency of the closed-loop system, which corresponds to the frequency where $|L(j\omega)| = 1$.
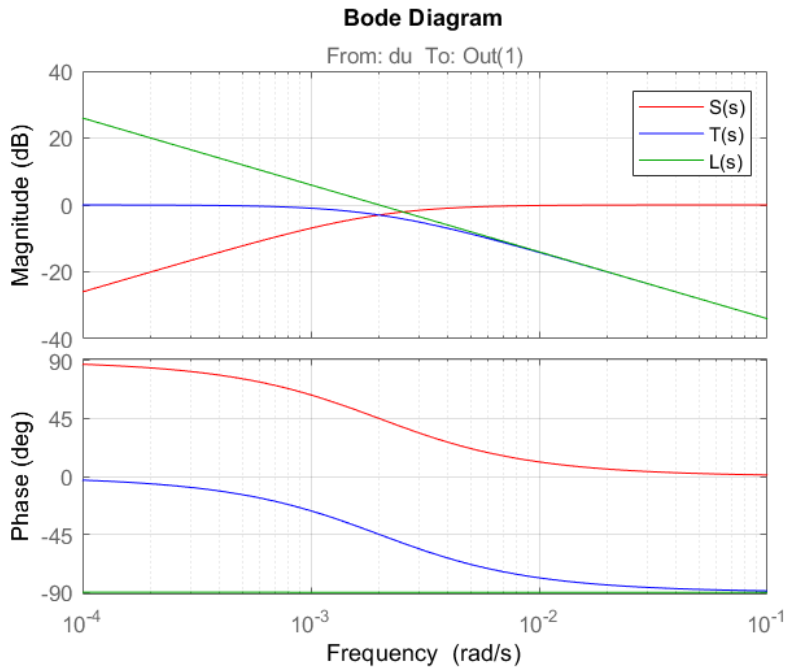
Figure 4.4.   Example of desired shape of the transfer functions in the loop.

As a result, the sensitivity and the complementary sensitivity function have opposite behavior in relation to the frequency where they are observed.

$$T(s) = \begin{cases} 1 & \omega \le \omega_c \\ 0 & \omega > \omega_c \end{cases} \qquad S(s) = \begin{cases} 0 & \omega \le \omega_c \\ 1 & \omega > \omega_c \end{cases} \tag{4.6}$$

where ω_c is the cross-over frequency. Therefore, the complementary sensitivity function $T(s)$ should approximate an ideal low-pass filter with corner frequency ω_c, and the sensitivity function $S(s)$ should have a corresponding high-pass filtering behavior. Since the bandwidth of a low-pass filter is determined by the corner frequency, we can say that the closed-loop bandwidth of a feedback control system can be expressed by the cross-over frequency ω_c.

The desired loop shaping of $L(s)$ discussed thus far should also provide a closed-loop system having prescribed static and dynamic properties in tracking reference and rejecting disturbance and measurement noise. Static requirements are typically achieved by imposing a minimum slope of $|L(s)|$ at $s = 0$. Indeed, using the final value theorem, the steady-state error can be expressed as

$$e_{ss} = \lim_{t \to \infty} e(t) = \lim_{s \to 0} s e(s) \tag{4.7}$$

If we consider the effect of the reference signal on the error, the above equation is written as

$$e_{ss} = \lim_{s \to 0} \frac{s}{1 + L(s)} r(s) \tag{4.8}$$

Again, to remain into the objectives of this chapter we can jump directly on the conclusions from the eq (4.8).

- A type-0 system has non-zero steady-state error (inversely proportional to the DC gain of the loop function) with respect to a step and ramp reference.

- A type-N system with $N \geq 1$ has zero steady-state error with respect to a step reference.

- A type-N system with $N \geq 2$ has zero steady-state error with respect to a ramp reference.

The general trend for higher order reference input can be already envisaged from the previous cases. Indeed, the static properties of a closed-loop system with respect to a reference input are good in the loop transfer function contains a prescribed number of poles at the origin. Such number can be selected by adding integrators in the controller function $K(s)$. The minimum number of poles at the origin is related to the type of reference (step, ramp, sinusoidal, ...). In general, the more integrators in the loop, the higher the order of reference signal that can be tracked.

In some cases, the closed-loops system must also providde static requirements with respect to the disturbance. In practice, the nature of disturbances is unknown. However, if the disturbance is slowly varying with time, a constant disturbance can be taken as good as a good approximation for the purpose of initial controller design. Let us examine the effect of a constant disturbance of amplitude $\hat{A}_d$ on the steady-state error of the closed-loop system.

According to (4.2) the error is related to the disturbance by the following equation

$$e(s) = -\frac{G(s)}{1 + L(s)} d(s) \tag{4.9}$$

Using the final-value theorem, the corresponding steady-state value for a constant disturbance is given by

$$e_{ss} = \lim_{s \to 0} \frac{sG(s)}{1 + L(s)} \frac{\hat{A}_d}{s} = \lim_{s \to 0} \frac{G(s)}{1 + L(s)} \hat{A}_d = \lim_{s \to 0} \frac{G(s)}{1 + K(s)G(s)} \hat{A}_d \tag{4.10}$$

Jumping to the conclusion, one can easily see that, in order to have a zero steady-state error of the closed loop system due to a step disturbance, the controller $K(s)$ must be at least of type-1, i.e., there must be an integrator $1/s$ in the controller to reject a constant disturbance.

4.2.1 Summary

As already outlined, the dynamic performance of the closed-loop system can be specified in different ways. Often, dynamic requirements are expressed in terms of time-domain specifications. It is also possible to recast some time-domain specifications as frequency-domain specifications, and therefore find a match between closed-loop transient characteristics and shaping of the loop function $L(s)$. It is very difficult to establish such exact correspondence, we can use the results obtained for simple systems as guidelines to design $L(s)$ in practical applications.

An example of the correspondence between time-domain and frequency-domain specifications is related to the speed of the closed-loop response of the system. If we consider the common test case of a step reference input, the speed of the response can be expressed by the rise-time and settling-time. It can be shown that, in some simple cases, the above time-domain parameters can be explicitly related to the gain cross-over frequency of the closed-loop system. Therefore, a prescribed rise- and settling-time can be specified by by designing a loop function $L(s)$ with prescribed bandwidth. Indeed, it is known that the larger the bandwidth of a system, the higher the speed of the response to an input. This can be considered as a general guideline which can be used for those systems whose complexity prevents to find an explicit relationship between rise-time and bandwidth.

Another example of correspondence between time- and frequency-domain properties of the control system involves the maximum overshoot of the closed-loop response, which is again typically related to a unit step command. The overshoot is a property that can be computed from the time response and is strongly dependent on the damping ratio of the closed-loop system. It can be shown that the damping, and so the maximum overshoot, is related to

the *phase margin* of the system, i.e., a prescribed maximum overshoot can be recast as a prescribed system phase margin. The phase margin is defined as how much phase lag can be added to the open-loop system without making it unstable. It can be calculated as the angle by which the phase of $L(s)$ is short of $-180°$ when the magnitude of $L(s)$ is unity, which match to the cross-over frequency ω_c . A companion quantity is the so called *gain margin*, which is defined as the amount by which the gain can be increased before the system becomes unstable. It has the value $1/x$, where x is the magnitude of $L(s)$ corresponding to a phase of $-180°$, and it is normally quoted in decibels. Gain and phase margin can be read off easily from the Bode plots of the loop function $L(s)$ or directly from Nichols plot. A particular attention should be payed to the *modulus margin* which is the minimal distance between the critical point $[-1,0]$ and the Nyquist plot of the open loop $L(s)$ transfer function.

4.2.2 Closed–loop control: ideal thrust modulation

An ideal case of thrust modulation can be presented to have an overview on the control design applied. If the satellite is equipped with a set of sensors that provides the necessary information on the attitude motion, it is possible to implement a control law which provides a torque command that drives the satellite towards the prescribed attitude. If the torque command is simply proportional to the attitude error, $e = \theta_{des} - \theta$, the closed–loop equation of motion becomes

$$\ddot{\theta} = M/J \quad \text{with} \quad M = K_p(\theta_{des} - \theta) = Ke$$
$$\ddot{\theta} = \frac{K_p}{J}(\theta_{des} - \theta) \quad \rightarrow \quad \ddot{\theta} + p^2\theta = p^2\theta_{des}$$

where $p^2 = K_p/J$. The solution of this second order equation for an initial condition of rest for $\theta = 0$ is

$$\theta(t) = \theta_{des}[1 - \cos(pt)]$$

i.e., an unacceptable undamped oscillation of amplitude θ_{des} about the desired condition. In order to damp the oscillation and asymptotically reach the desired condition, it is necessary to add a damping term in the control law, proportional to the angular rate $\dot{\theta}$. The command torque is thus

$$M = K_p(\theta_{des} - \theta) + K_d\dot{\theta} \qquad (4.11)$$

and the closed-loop of the equation of motion becomes

$$\ddot{\theta} + c\dot{\theta} + p^2\theta = p^2\theta_{des}$$

where the coefficient of the damping term $c = 2\zeta p = -K_d/J$ is positive (damped oscillations) if the gain associated to the angular rate is negative (negative feedback). There are two possible resulting closed–loop behaviours. For $0 < \zeta < 1$, the time–history of the angular motion is

$$\theta(t) = \theta_{des}[1 - \exp(-\zeta p t)\cos(p_d t)]$$

where $p_d = p\sqrt{1-\zeta^2}$, that is, damped oscillations with an exponentially decaying amplitude. If on the converse $\zeta > 1$, the characteristic equation has two real solutions

$$\lambda_{1,2} = p\left(-\zeta + \sqrt{\zeta^2 - 1}\right)$$

which are both negative. In this case the evolution of the rotation angle is

$$\theta(t) = \theta_{des}\left[1 - \frac{\lambda_2}{\lambda_2 - \lambda_1}\exp(\lambda_1 t) + \frac{\lambda_1}{\lambda_2 - \lambda_1}\exp(\lambda_2 t)\right]$$

Two important issues need to be considered, at this point. The first one is the choice of the gains. The case with $\zeta < 0$ is not considered at all, inasmuch as one of the poles of the closed loop system would be a positive real number, that is, the closed loop system would be unstable. Whem $\zeta < 1$ (sub–critical damping), the time τ to damp out 99% of the initial oscillation amplitude increases as ζ gets smaller according to the equation

$$\exp(-\zeta p \tau) = 0.01 \quad \rightarrow \quad \tau = -\log(0.01)/(\zeta p)$$

At the same time, if $\zeta > 1$ (super–critical damping) the time constant of the slowest mode becomes larger, being approximately equal to ζ/p, for large values of ζ. This means that a largely super–critical damping coefficient will cause a slower convergence.

The best performance in terms of maneuver agility are obtained for the critical damping $\zeta = 1$, which guarantees the fastest convergence time to the desired position. The over–damped case may be of interest in those cases when fuel consumption is more a stringent concern than maneuver time. On the contrary, the under–damped case, which exhibits some overshoot, is of no practical interest, since it is characterized by a longer settling time and an increased fuel consumption, because of the thrusting system firing alternatively in both directions, during the oscillations.

The second issue concerns the actual implementation of a control law in the form (4.11). Such a control law would be realistic only if the control torque provided by the thruster could be modulated. Unfortunately direct thrust modulation would require a complex hardware and, at the same time, would be extremely inefficient in large portions of the required thrust range. For these reason, thrusters are always on/off devices. As a consequence, some form of pulse modulation is required to provide a feasible implementation of the control torque

demand. Two techniques can be implemented, the Pulse–Width/Pulse– Frequency (PWPF) modulator, which is an analogic device, and the Pulse–Width Modulator (PWM), which lends itself to a discrete time implementation. The study made in this thesis does not take into account the possibility of a PWPF or PWM, but only a continuous thrust.

4.3 Quaternion feedback attitude control

Considering the LPF heritage, we can gather a set of controller designed and tested for different scenarios of the mission. A similar approach can be foreseen for LISA. Here PID controllers are used to perform the different SISO controllers. In general, the quaternion feedback control provides a means for obtaining a nearly–optimal reorientation, with a control logic only marginally more complex.

The potential function method for nonlinear control stems directly from Lyapunov's second method: an extended form of the Lyapunov function, referred to as the potential function, is analytically defined with a global minimum at the target state. According to Lyapunov's second theorem, the state vector converges to the goal point if the rate of change of the potential is negative definite. The mechanism which drives the convergence is thus based upon the rate of change of the potential function $V = V(x)$: whenever the rate of change of V is positive for the unforced system, the state vector will diverge from the goal point unless some form of control over the system is available, in which case it is possible to make negative by properly tailoring the control action. In this way, given a dynamical system described by a set of differential equations in the form $\bar{x} = f(x, u)$, where u indicates a set of available control variables, it is possible to derive a control methodology which forces the convergence to the desired goal condition, indicated by the symbol $\bar{x}$. Convergence to $\hat{x}$ and global stability can be enforced by building a candidate Lyapunov potential function that has a global minimum in $\hat{x}$, that is, such that

$$1) \quad V(\bar{\mathbf{x}}) = 0$$

$$2) \quad V(\mathbf{x}) = 0 \quad \text{for} \quad \mathbf{x} \neq \bar{\mathbf{x}}$$

$$3) \quad V(\mathbf{x}) \to \infty \quad \text{for} \quad ||\mathbf{x}|| \to \infty$$

Once a candidate Lyapunov function is available, its rate of change is given by

$$\dot{V}(\mathbf{x}) = \frac{\partial V}{\partial \mathbf{x}} \frac{d\mathbf{x}}{dt} = \frac{\partial V}{\partial \mathbf{x}} \mathbf{f}(\mathbf{x}, \mathbf{u})$$

By choosing a control action $\mathbf{u} = \mathbf{u}(\mathbf{x})$ such that

$$4) \quad \dot{V}(\mathbf{x}) < 0 \quad \text{for} \quad \mathbf{x} \neq \bar{\mathbf{x}}$$

Lyapunov theorem guarantees that the resulting closed loop system is globally asymptotically stable in $\bar{\mathbf{x}}$ and thus, once the final target state has been defined, controllable. This method for the generation of closed–loop control functions has the advantage of allowing the implementation of non–linear controls for wide amplitude manoeuvres, since the method does not hinge on linearization.

4.3.1 Slew to target

Starting from the consideration made in the previous sections, we can describe the simplest model to control as the S/C attitude in a reference problem. The preliminary problem that we are going to face can be useful in the perspective of a reacquisition of the target attitude due to the insertion in orbit and for our purpose can be seen as a first check of the model.

The problem can be synthesized as a S/C in detumbling when only affected by the solar pressure. Reasoning in short-term dynamics, the solar pressure can be considered a constant disturbance, since the attitude of the S/C is limited and forced to converge to the target. The control problem can be easily solved via quaternion feedback control. Actually, with the lyapunov verification we proved that a single proportional-derivative (PD) controller can stabilize the system. However, the absence of the integral term and the contemporary presence of the solar pressure, will lead to a considerable steady-state error.

In order to study the nonlinear system, it is useful to extract continuous-time linear state-space model around an operating point from the model. This rapid linearization allow us to see the linearized system in a MIMO form. Indeed, the system asks as input the vector torque $\mathbf{M}_T$ and the feedback is done with the inertial vector quaternion $\mathbf{q}_{SI}$. For the sake of simplicity, the 3×3 MIMO system can be considered as a diagonal MIMO, which is equal to three SISO systems. Each SISO system is a simple double integrator.
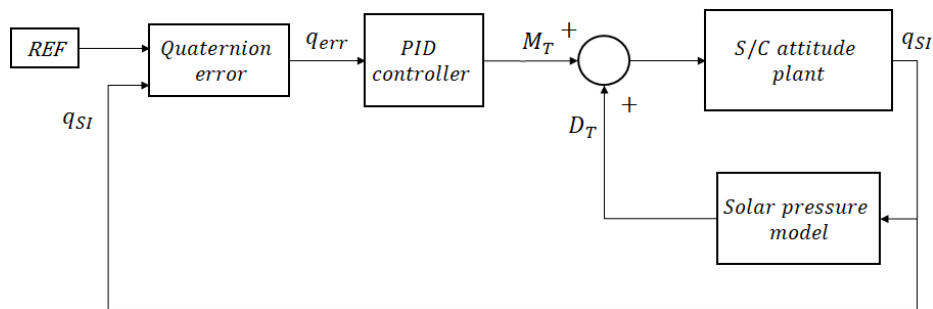
Figure 4.5. Simulink$^{©}$ noise-free model.

The diagonal represents the effect of $\mathbf{M}_i$ on $\mathbf{q}_i$ where $i = x, y, z$. Concerning the roll and pitch, the open loop transfer functions are identical and present a cut-off frequency

of $w_c = 0.023265 rad/s$. Meanwhile, the yaw is slightly translated and presents a cut-off frequency of $w_c = 0.02081 rad/s$. Therefore, the gains for the MIMO *Proportional Integrative Derivative* (PID) will be different for the yaw. The reason of this difference can be traced back to the inertia matrix of the S/C.

In the tables 4.1 4.2 and 4.3 are showed three different PID-tuning made on the same system. For the PID form with proportional, integral, and derivative with first-order filter on derivative term showed below

$$K_p + \frac{K_i}{s} + K_d \frac{s}{T_f s + 1}$$

Table 4.1. PID tuning gains for $w_c = 0.02 rad/s$

K_p	K_i	K_d	T_f
0.136	0.000127	35.8	9.2
0.17	0.000159	44.8	9.2

Table 4.2. PID tuning gains for $w_c = 0.2 rad/s$

K_p	K_i	K_d	T_f
1.36	0.00127	358	0.92
1.7	0.00159	448	0.92

Table 4.3. PID tuning gains for $w_c = 2 rad/s$

K_p	K_i	K_d	T_f
1360	127	3580	0.092
1700	159	4480	0.092

In a noise-free simulation we can obtain an acceptable response in time domain from the slowest PID. In this case, the PID contribution to the dynamic is just enough to bring the error to zero in less than 5000 seconds. The response of the systems with greater cut-off frequency is more stiff and less damped, thus generating more oscillation around the target.

The model with the actuation dynamics in presented in figure 4.6. With the introduction of the propulsion system, which enclose the dispatching of the commanded torque to the single thruster and its actuation noise, a slow control of the dynamic will be not sufficiently robust to inhibit the delay and the noise of the actuation.

For a simple slew to target manoeuvre the main constraints are set by the actuation authority. Moreover, in absence of stringent performance requirements, it is acceptable to have as sensor implied in this phase the STR.
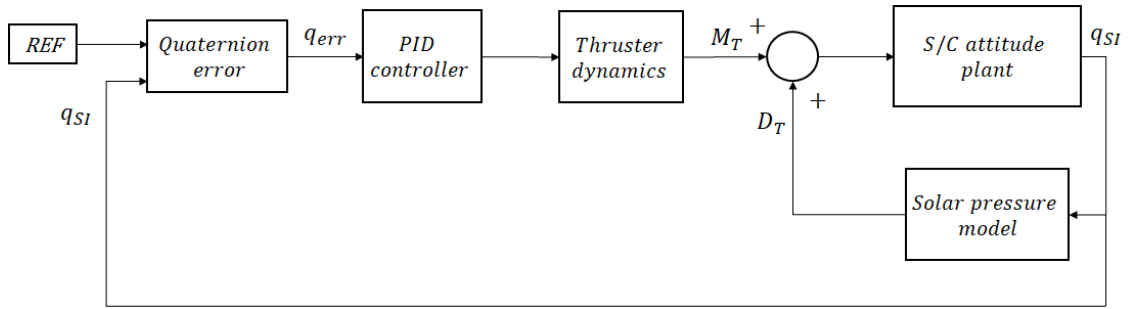
Figure 4.6. Model with actuation system.
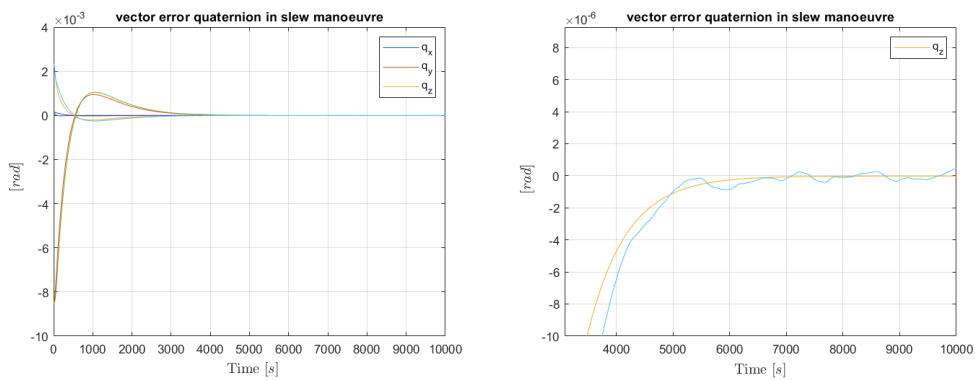
Figure 4.7. Error quaternion performance in the slew with and without the actuation model at $w_c = 0.02 rad/s$. (Left) The major effect of the actuation model is in the transient due to the delay. (Right) The noise effect is visible in the steady state.
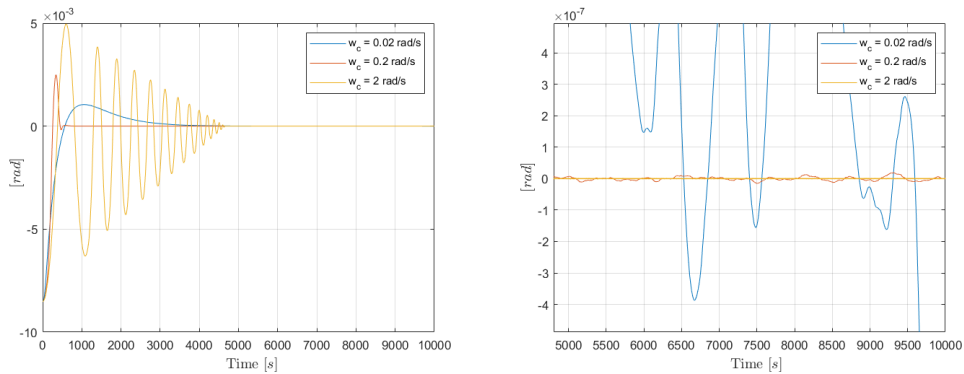
Figure 4.8. Error pitch performance in the slew with the actuation model for different w_c. (Left) The major difference between the 3 PID is given by the settling time and oscillation. (Right) The greater is the w_c, the more the actuation noise is rejected.

4.3.2   Fine pointing control

After slew to target, the control system switches to fine pointing control, in order to maintain the payload aimed at the desired target with a prescribed tolerance, in presence of external disturbances. A simple way to achieve such a fine pointing is to use cold gas jets, that produce thrust in a suitable range, with short pulse times for fine control.

Without external disturbances, the satellite would bounce back and forth between the edges of a limit cycle, thus requiring the maximum number of pulses per unit time. This means that the estimate of the fuel consumption in this situation is a worst–case–scenario. However, our study is focused on the preliminary control of the attitude with ideal-continuous thrusters.

The orbit that each S/C must follow is not only studied in terms of orbital parameters. As a matter of fact, each S/C must reach along its orbit a predescribed inertial attitude in order to aim at the other S/Cs. Considering only the inertial reference frame, this perspective would require the tracking of a changing-time attitude. In fact, the nominal angular motion that the S/C must reach in the IF is showed in figure 4.9. Generally speaking, one can declare that
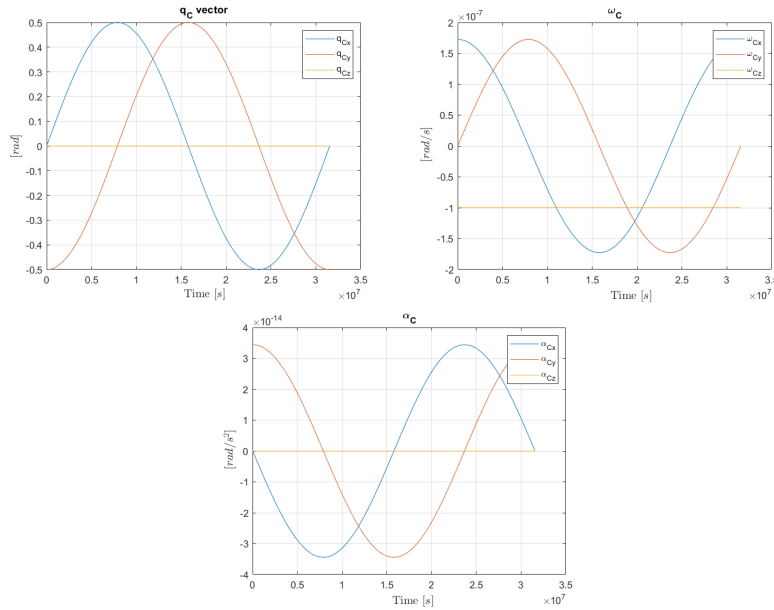
Figure 4.9.   Nominal attitude, angular velocity and angular acceleration in one orbit period of the S/C expressed in the IF.

the S/C along its orbit must be forced to follow the angular motion presented in the figure. Only in a nominal condition the following of the path would lead to the formation of the exact constellation. Nevertheless, the angular motion that the S/C must follow is dictated

by the behavior of the other S/Cs and so the fine pointing does not depend by a single S/C. To simplify the discussion, we can assume that two out of three S/Cs are forced to follow the path of the nominal orbit (is implied that the orbit also includes the angular motion) and in other words, it must be ensure by the control that the $\mathbf{q}_S$ quaternion tends to zero. This quaternion represents the rotation CF ->SF and so the deviation of the actual attitude of the free S/C from the nominal attitude.
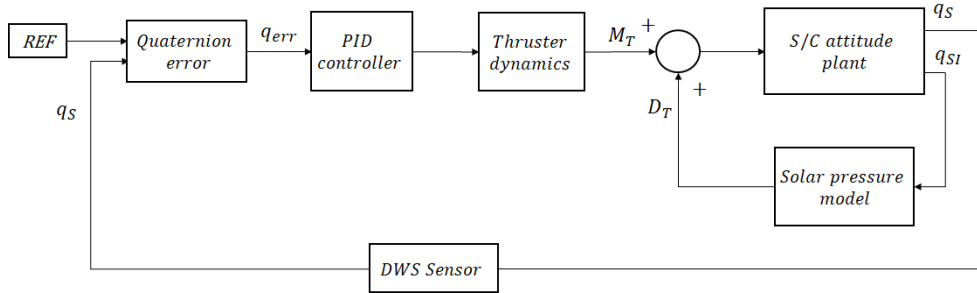

Figure 4.10. Complete model of the fine pointing control with actuation and sensing system.

To be true, a first slew manoeuvre must be performed to align the S/C with the nominal inertial attitude. Furthermore , the S/C must be forced to track the nominal angular motion and then performer the fine pointing. The described phase can be seen as the sum of two problems. The first is the angular tracking of the inertial attitude and the second is the fine pointing to reference. In this phase we want to analyze the only the reference problem, considering that is the more critical part of the phase. The model has been slightly modified to account for the feedforward control of the angular motion. The S/C now starts his dynamic in the nominal motion but is disturbed by the solar pressure. A proof of the correctness of the model can be seen disabling the solar pressure model. Effectively, in this case the quaternion $\mathbf{q}_S$ will not diverge from its initial condition.

It must be emphasized the role and the usage of the sensors in these phases. In the slew to target manoeuvre, the sensor used to feedback the inertial attitude is the STR. In the early phases of the mission the control system must rely on the STR to target the initial attitude. However, once that the constellation has been acquired, the control system can entrust to the OMS in order to deliver a more accurate attitude. The acquisition of the inertial angles from the OMS is not direct but requires a tailor made process to integrate the different data sources. From a preliminary perspective, it is acceptable to base our control on the feedback of the OMS. In a 3-roles scenario in which the S/Cs are be affected by different dynamics since each one starts from different initial conditions, such study must be carried on.

Like done before, the MIMO system can be studied in a parallel form of three SISO

systems. In this case, the assumption to design the controller based on the MIMO diagonal will be stronger since the non-diagonal SISO systems are comparable with the diagonal. A linearization has been made in order to obtain a linear state-space model. The system studied
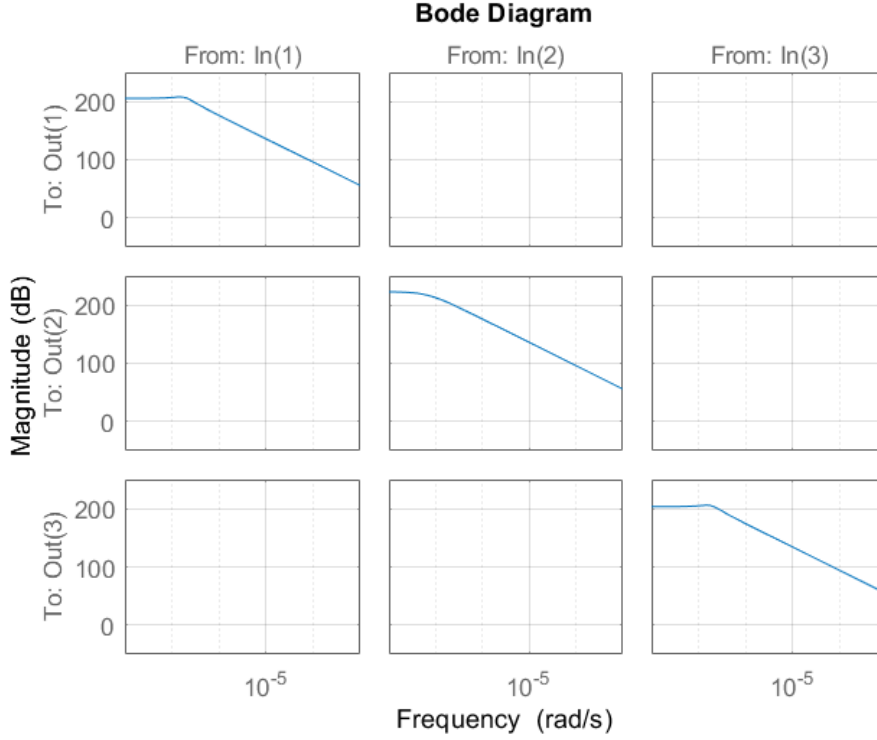

Figure 4.11.   SISO systems in matrix form of the linearized model in fine pointing manoeuvre.

in this part, presents some differences from the one studied before. Besides, the difference in the type of control problem, the main reason is given by the presence of the angular motion of the S/C. Indeed, the period of the motion is 365 days, which gives a frequency $\omega_p \approx 2 \cdot 10^{-7} rad/s$. One can see that the MIMO system changes from the natural double integrator, i.e., double pole in zero. In the new configuration the double pole is moved to the characteristic frequency of the orbital motion. So, each SISO system assumes the generic form

$$G_{SISO} = \frac{k_n}{s^2 + p^2}$$

where k_n is a generic DC gain and p is the pole.

To prove the stability of a MIMO system is not sufficient to show the gain, phase and modulus margin. Indeed, these systems are more often considered in terms of sensitivity and complementary sensitivity function. Common and not very stringent numerical values to be set for acceptable stability margins shall be as follow:

Gain margin shall be $\geq 6dB$

Phase margin shall be $\geq 30deg$

Modulus margin shall be ≥ 0.5

Peak margin for the sensitivity and complementary sensitivity function shall be $\leq 6dB$

In figure 4.12 are showed the open loop SISO requirements. In figure 4.13 the consequent closed loop MIMO requirements. The controller taken into account is the one with $\omega_c = 0.5rad/s$
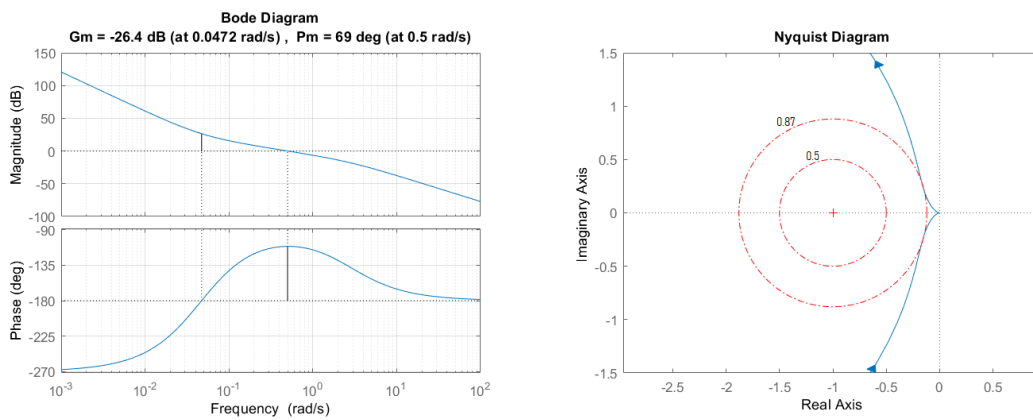

Figure 4.12.   SISO system stability requirements visualization.
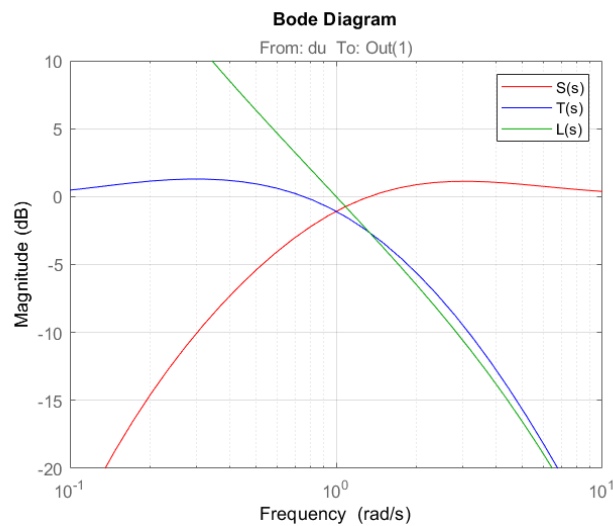

Figure 4.13.   MIMO system stability requirements visualization.

Via loop shaping we can derive a constrained behavior of the closed-loop functions. As a matter of fact, the imposition of requirements over a given plant sets a family of closed-loop function suitable for the control problem. We can recall the figure 4.2 to define the closed-loop control loop specifications.

$$S_{spec} = \frac{y_{req}}{Gd_{spec}}, \quad \text{Input noise suppression}$$

$$T_{spec,1} = \frac{y_{req}}{n_{spec}}, \quad \text{Measurement noise suppression}$$

$$T_{spec,2} = \frac{Gu_{req}}{n_{spec}}, \quad \text{Measurement noise influence on actuator signal}$$

$$T_{spec,3} = \frac{u_{req}}{d_{spec}}, \quad \text{Input noise influence on actuator signal}$$
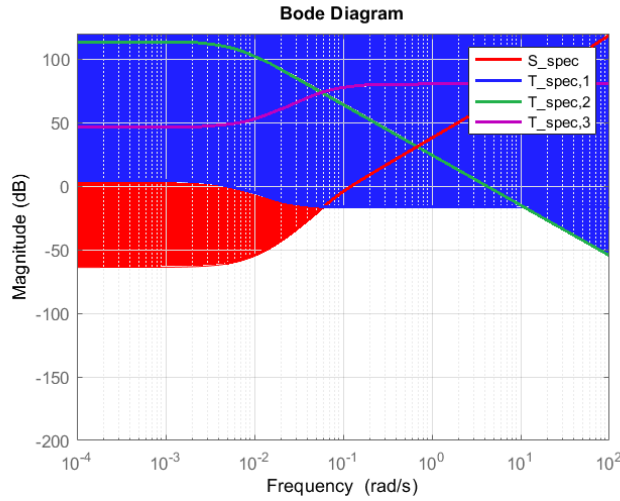
Figure 4.14. Closed-loop bounding requirements.

The sensitivity function is constrained by a single specification function which sets a lower boundary for the control system. The complementary sensitivity function is constrained by three specification. From the figure 4.14 is visible that the measurement noise suppression can not be met in a certain region. Eventually, the $T_{spec,1}$ exceeds the $0dB$ in the cut-off frequency region. The critical element in this constraint is the DWS on the SC which noise shape filter has an high gain value. However, a recommendation on the sensor noise is premature since this preliminary study is excluding the presence of any sort of estimator in the model. Eventually, the sensor characteristics used in this control simulation are improved in order to define a proper feasibility region but imposed to be lower or equal to the best

sensor available, i.e., the DWS on the TM. Moreover, the assumption made is not too far from reality since the actual attitude of the TM can be used as a gyroscope.
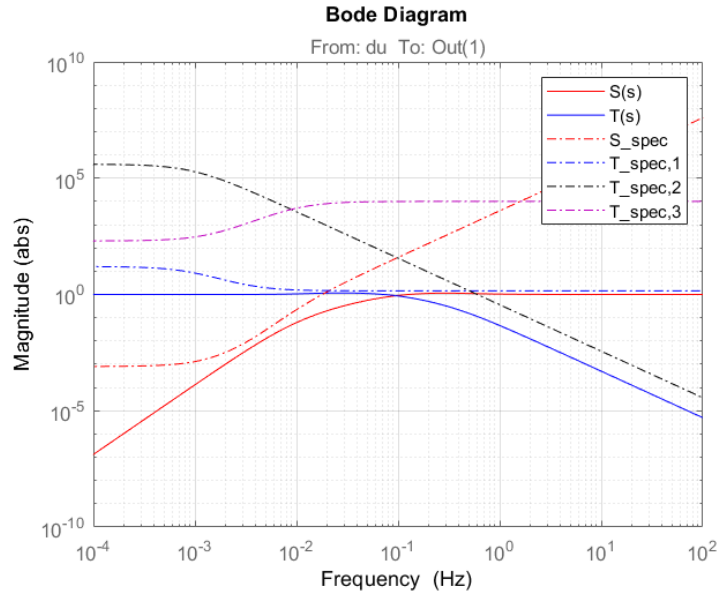
Figure 4.15. Closed-loop relaxed bounding requirements.

Exploiting the results of the slew manoeuvre and keeping in mind the consideration made for the control design, we can imagine to adopt a restrict bandwidth in which place the cut-off frequency of the attitude controller. Actually, this band stays in the order of $0.1rad/s$. The choice to take a smaller cut-off frequency, in a simulation that takes into account sensors and actuator would return unacceptable results. A proof is given in figure 4.16.
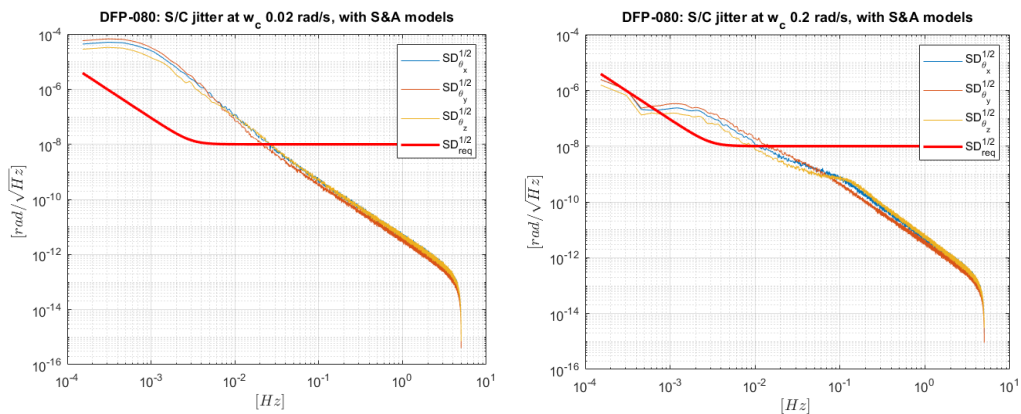
Figure 4.16. S/C jitter simulation with low cross over frequency.

85

The following gains have been found and simulated in the closed loop.

Table 4.4.   PID gains for ω_c at 2 rad/s

K_p	K_p	K_d	T_f
$1.18 \cdot 10^3$	110	$3.1 \cdot 10^3$	0.092
$1.47 \cdot 10^3$	137	$3.88 \cdot 10^3$	0.092

Table 4.5.   PID gains for ω_c at 1 rad/s

| K_p	K_i	K_d	T_f
297	13.9	1560	0.183
371	17.4	1950	0.183

Table 4.6.   PID gains for ω_c at 0.7 rad/s

K_p	K_i	K_d	T_f
146	4.77	1090	0.262
182	5.96	1360	0.262

Table 4.7.   PID gains for ω_c at 0.5 rad/s

K_p	K_i	K_d	T_f
74	1.7	780	0.3667
92	2.1	973	0.3667

The PID gains tried in simulation gave the following results:
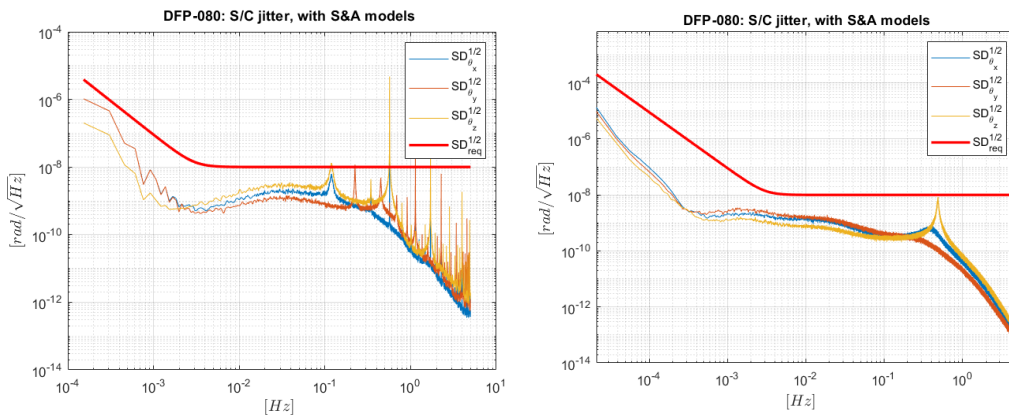
Figure 4.17.   Spectral density of the S/C angular jitter with different cut-off frequencies ω_c: $2 rad/s$ (left) e $1 rad/s$ (right).

Must be noted that the highest cut-off frequency ($\omega_c = 2 rad/s$) requires a $T_f = 0.092s$ which is approximately $1/T_f \approx 10 Hz$. The crossover frequency ω_c roughly sets the control
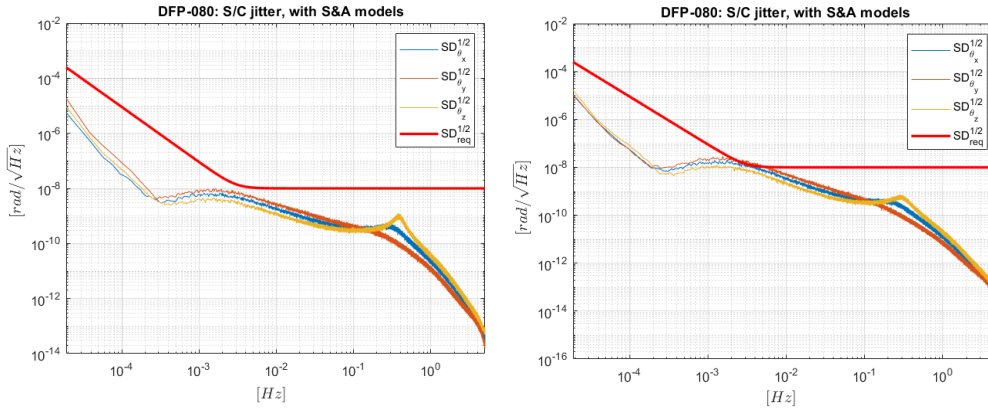
Figure 4.18. Spectral density of the S/C angular jitter with different cut-off frequencies ω_c: $0.7rad/s$ (left) e $0.5rad/s$ (right).

bandwidth. The closed-loop response time is approximately $1/\omega_c$ but the filter setup takes into account the first order filter which interacts with the command input. Since the thrust update rate is $10Hz$, the first controller can be excluded. Acceptable performances are given by the other PID gains. As a matter of fact, one can see that the main spike in the SD are given in the high frequency range. That contribution is mainly given by the choice of the cut-off frequency and consequent coupling in the system, i.e., solar pressure noise, S/C angular motion.

The second requirement on the S/C attitude is given as a pointing requirement in time domain. The laser pointing accuracy shall be as follow

$$e_p \leq 10nrad(3\sigma)$$

This last requirement can not be met with a noisy sensor. Actually, the level of required accuracy asks for the lowest sensing noise level. In figure 4.19 are showed the Euler angles obtained implementing a control system fed by the SC attitude measured by the improved DWS. In figure 4.20 are presented the normal distribution of the accuracy obtained from the pointing error. The sensing noise determines the performances and the meeting of the requirement. The standard deviation decreases of two orders of magnitude with the improved sensor leading to the fulfillment of the requirement on the pointing accuracy. To requirement can be met only with the less noisy sensor.

In order to verify the requirement it must be established the standard deviation and the mean value of the normal distribution. Moreover, ita can be declared that the requirements is met if $\mu + 3\sigma \leq 1 \cdot 10^{-8}$, which do not happens with the sensor laser sensor of the S/C (DWS S/C). Also for this requirement must be considered an improvement.
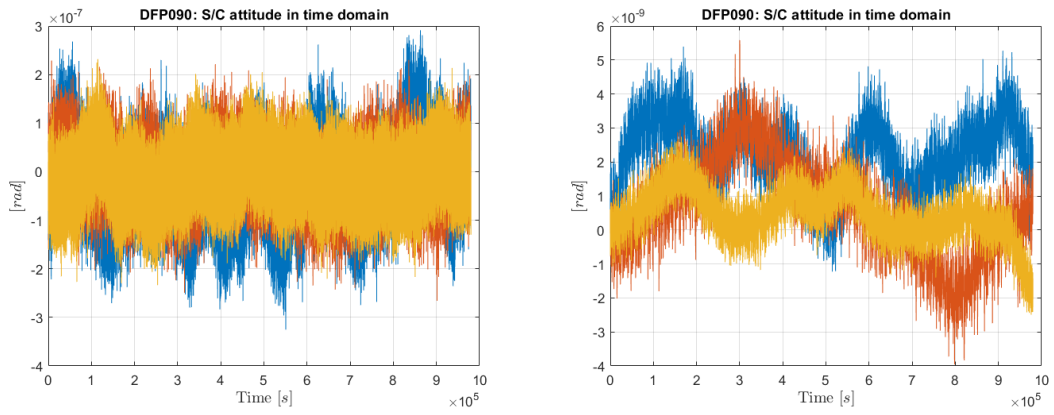
Figure 4.19.   Euler angles of the S/C attitude in the fine pointing maneuver with the DWS S/C sensing noise (left) and with the DWS TM sensing noise (right).
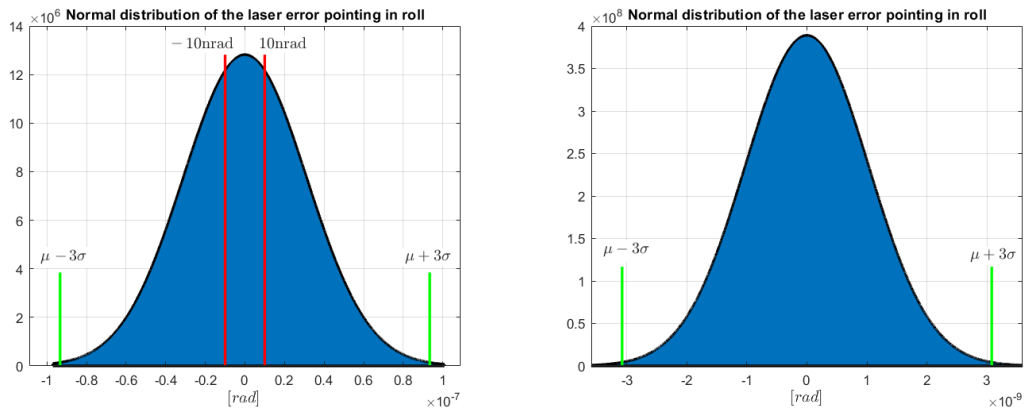

Figure 4.20.   Normal distribution of laser pointing error with the DWS S/C sensing noise (left) and with the DWS TM sensing noise (right).

Chapter 5

Conclusion

In this thesis, after a focus on the LISA science mission, we have pointed out from a system-level perspective the peculiar aspects of the mission. In these terms, we highlighted the main factors that must be taken into account in order to perform all the phases of the mission and enable proper science measurements. This preliminary study can be considered as a critical review in terms of science performance requirements which in accordance with the science measurement are given as spectral densities. Moreover, we had the possibility to consider the LISA science goal as a consequent improvement of the past LISA Pathfinder mission. Exploiting the LPF heritage and the input given by ESA, we presented the modeling of the LISA systems and its in-orbit environment. At this regard, the study is led with the aim of a proper characterization of every kind of disturbance acting on the mission, whereas internal or external. Nevertheless, was part of our intent to present a former modeling of the sensors and actuators involved in the mission. A peculiarity of the sensors stays in the different type of sensed source, e.g. the GRS and the IFO sense the same physical variable in two different ways. In turn, the actuation systems involved exploit different type of physical phenomena. As a matter of fact, besides the mere understanding of the LISA mission disturbance, great effort was made in order to develop proper mission and science simulator and simulation models able to reproduce the effects of the disturbance scenario, thus supporting an effective controller design and implementation. In addiction, a detailed set of nonlinear equation representing the LISA dynamics was reported and discussed. Preliminary prototyping in Simulink$^{©}$ simulation environment is implemented. In the control design phase we dealt with the many aspect related to the LISA control problem. Starting from a loop-shaping approach we were able to identify the main control constraints in the LISA system. As a matter of fact, a discussion on the LISA system is presented and exploited in order to simplify the control design of a global plant in three distinct loops. The definition of three

different loops enabled the possibility to control the single S/C attitude system. Besides the differences of the three loops in terms of plant, actuators and sensors, we can prove that the control design approach is applicable to every plant. A preliminary quaternion feedback attitude controller is implemented for a simple S/C slew maneuver. The results are used to evaluate the correctness of the simulation environment and to observe the performance of a preliminary controller. Then, considering the S/C operating mode we took into account the science requirements in order to support a correct control design. At this point, sensors and actuators characterization turned to be a key point of the control design. Actually, the studied plant is a nonlinear MIMO system that must be controlled within requirements. The control system effectiveness and results are firstly proved in terms of stability. Some of the closed-loop control loop specifications are then discussed. In the end, many simulation results of the S/C attitude control loop are presented and discussed. In general the impact of actuator and sensor noise has been highlighted in time and frequency domain. As a result, the improvement requested for these subsystem can be considered to be confirmed by other study on the system.

5.0.1 Future work

Starting from the results obtained for the S/C attitude control, the control design of the TM suspension loop and DF loop shall be conducted. A more complex control design shall be taken into account, e.g., H_∞. The possibility to use an observer to provide better results shall be considered. In general, shall be carried out a trade-off on different control system architectures and advanced, robust control system design methodologies to preliminary prototype the drag free control system.

Appendix A

Derivation of the linear equations

S/C rotation model

The angular velocity and acceleration of the S/C wrt CF are given by

$$\omega_S = \omega_{SI} - T_C^S \omega_C$$
$$\dot{\omega}_S = \dot{\omega}_{SI} - \dot{T}_C^S \omega_C - T_C^S \dot{\omega}_C = \alpha_{SI} + \omega_S \times T_C^S \omega_C - T_C^S \alpha_C$$
$$\cong \alpha_{SI} + T_C^S \alpha_C.$$

The angular acceleration $\alpha_{SI} \equiv \dot{\omega}_{SI}$ is obtained from the Euler equation

$$\dot{\omega}_{SI} = \Lambda(\omega_{SI}) + J_S^{-1} \left(\mathbf{M}_T + \mathbf{D}_S - \sum_{i=1,2} \left(T_{Oi}^S \mathbf{M}_{Ei} + \mathbf{b}_i \times T_{Oi}^S \mathbf{F}_{Ei} \right) \right)$$

$$\cong J_S^{-1} \left(\mathbf{M}_T + \mathbf{D}_S - \sum_{i=1,2} \left(\bar{T}_{Oi}^S \mathbf{M}_{Ei} + \bar{\mathbf{b}}_i \times \bar{T}_{Oi}^S \mathbf{F}_{Ei} \right) \right)$$

Including $T_C^S \alpha_C$ in the disturbance term, we obtain

$$\dot{\omega}_S = J_S^{-1} \left(\mathbf{M}_T + \mathbf{D}_{SL} - \sum_{i=1,2} \left(\bar{T}_{Oi}^S \mathbf{M}_{Ei} + \bar{\mathbf{b}}_i \times \bar{T}_{Oi}^S \mathbf{F}_{Ei} \right) \right).$$

TM translation model

Relative acceleration in IF → relative acceleration in OF

The equation for the jth TM is

$$\ddot{\mathbf{r}}_{Mj} = \mathbf{a}_{Rj} - \Omega(\omega_{Oj})\mathbf{r}_{Mj} - 2\omega_{Oj} \times \dot{\mathbf{r}}_{Mj} \cong \mathbf{a}_{Rj}$$

where $\mathbf{a}_{Rj} \doteq T_I^{Oj} \ddot{\mathbf{r}}_{Mj}^I$.

Absolute acceleration in IF → relative acceleration in IF

The equation for the jth TM is

$$\mathbf{a}_{Rj} \doteq T_I^{Oj} \ddot{\mathbf{r}}_{Mj}^I = \mathbf{a}_{Nj} - T_S^{Oj}\Omega(\omega_{SI})\mathbf{b}_{Sj} - \Omega(\omega_{Oj})\mathbf{b}_M$$

$$\cong \mathbf{a}_{Nj} - \Omega(\omega_{Oj})\mathbf{b}_M$$

where $\mathbf{a}_{Nj} \doteq T_I^{Oj}\Delta\ddot{\mathbf{r}}_{Ij}$.

Newton's laws

The equation for the jth TM is

$$\mathbf{a}_{Nj} \doteq T_I^{Oj}\Delta\ddot{\mathbf{r}}_{Ij} = \mathbf{u}_{bj} + S_{Mj}\mathbf{r}_{Mj} + m_M^{-1}(\mathbf{F}_{Ej} + \mathbf{d}_{Mj}) - m_S^{-1}T_S^{Oj}(\mathbf{F}_T + \mathbf{d}_S) + m_S^{-1}\sum_{i=1,2}T_{Oi}^{Oj}\mathbf{F}_{Ei}$$

$$\cong \mathbf{u}_{bj} + S_{Mj}\mathbf{r}_{Mj} + m_M^{-1}(\mathbf{F}_{Ej} + \mathbf{d}_{Mj}) - m_S^{-1}\bar{T}_S^{Oj}(\mathbf{F}_T + \mathbf{d}_S) + m_S^{-1}\sum_{i=1,2}\bar{T}_{Oi}^{Oj}\mathbf{F}_{Ei}.$$

Merging the equations

We can merge all the TM translation equations as follows:

$$\ddot{\mathbf{r}}_{Mj} = \mathbf{a}_{Rj} = \mathbf{a}_{Nj} - \Omega(\omega_{Oj})\mathbf{b}_M$$

$$= -\Omega(\omega_{Oj})\mathbf{b}_M + \mathbf{u}_{bj} + S_{Mj}\mathbf{r}_{Mj} + m_M^{-1}(\mathbf{F}_{Ej} + \mathbf{d}_{Mj}) - m_S^{-1}\bar{T}_S^{Oj}(\mathbf{F}_T + \mathbf{d}_S) + m_S^{-1}\sum_{i=1,2}\bar{T}_{Oi}^{Oj}\mathbf{F}_{Ei}.$$

Including $-\Omega(\omega_{Oj})\mathbf{b}_M + \mathbf{u}_{bj}$ in the disturbance term $\mathbf{d}_{MLj}$, we obtain

$$\ddot{\mathbf{r}}_{Mj} = S_{Mj}\mathbf{r}_{Mj} + m_M^{-1}(\mathbf{F}_{Ej} + \mathbf{d}_{MLj}) - m_S^{-1}\bar{T}_S^{Oj}(\mathbf{F}_T + \mathbf{d}_S) + m_S^{-1}\sum_{i=1,2}\bar{T}_{Oi}^{Oj}\mathbf{F}_{Ei}.$$

TM rotation model

The angular velocity and acceleration of the TM wrt OF are given by

$$\omega_{Mj} = \omega_{MIj} - T_{Oj}^{Mj}\omega_{\gamma j} - T_S^{Mj}\omega_{SI}$$

$$\dot{\omega}_{Mj} = \dot{\omega}_{MIj} - \dot{T}_{Oj}^{Mj}\omega_{\gamma j} - T_{Oj}^{Mj}\alpha_{\gamma j} - \dot{T}_S^{Mj}\omega_{SI} - T_S^{Mj}\dot{\omega}_{SI}$$

$$= \alpha_{MIj} + \omega_{Mj}\times T_{Oj}^{Mj}\omega_{\gamma j} - T_{Oj}^{Mj}\alpha_{\gamma j} + \left(T_{Oj}^{Mj}\omega_{\gamma j} + \omega_{Mj}\right)\times T_S^{Mj}\omega_{SI} - T_S^{Mj}\alpha_{SI}$$

$$\cong \alpha_{MIj} - \bar{T}_{Oj}^{Mj}\alpha_{\gamma j} - \bar{T}_S^{Mj}\alpha_{SI}$$

The angular acceleration $\alpha_{MIj} \equiv \dot{\omega}_{MIj}$ is obtained from the Euler equation

$$\alpha_{MIj} = \Lambda(\omega_{MIj}) + S_{Rj}\boldsymbol{\theta}_{Mj} + J_M^{-1}\left(T_{Oj}^{Mj}\mathbf{M}_{Ej} + \mathbf{D}_{Mj}\right)$$

$$\cong S_{Rj}\boldsymbol{\theta}_{Mj} + J_M^{-1}\left(\bar{T}_{Oj}^{Mj}\mathbf{M}_{Ej} + \mathbf{D}_{Mj}\right)$$

$$\cong 2S_{Rj}\mathbf{q}_{Mj} + J_M^{-1}\left(\bar{T}_{Oj}^{Mj}\mathbf{M}_{Ej} + \mathbf{D}_{Mj}\right).$$

where the relation $\boldsymbol{\theta} \cong 2\mathbf{q}$ has been used. Including $\bar{T}_S^{Mj}\alpha_{SI}$ and $\bar{T}_{Oj}^{Mj}\alpha_{\gamma j}$ in the disturbance term, we obtain

$$\dot{\omega}_{Mj} = 2S_{Rj}\mathbf{q}_{Mj} + J_M^{-1}\left(\bar{T}_{Oj}^{Mj}\mathbf{M}_{Ej} + \mathbf{D}_{Mj}\right).$$

Appendix B

Welch approximation

Modeling stochastic signals is of interest in a wide range of applications, even more is a central part of LISA-like missions. The success of the entire mission is based on the necessity to identify and reject all the disturbances acting on a delicate and complex system and to all his part. Additionally, the frequency content of noise input to a system must be carefully modelled. In the LISA requirements it is specified by a power spectral density (PSD [u/Hz]) or better by his squared root (RPSD) i.e., amplitude spectral density (ASD [u/sqrt(Hz)]). If a linear time invariant (LTI) system model is considered, the PSD can be applied in the frequency domain by multiplying the PSD with the squared transfer function of the model. This can be easily proven and used as in [51]. If a nonlinear model has to be simulated in the time domain, a suitable filter transfer function must be derived from the PSD.

SISO block diagram with noise-shape filters Filtering operation is performed by an estimator filter,$H_f(f)$ designed to shape the output PSD:

$$S_{yy}(f) = |H_f(f)|^2 S_{xx}(f)$$

Where $S_x x(f)$ is the PSD of a white noise. A proposed approach to design the filter starts with the definition of the $S_{yy}(f)$, which is given, and then perform an estimation to obtain $H_f(f)$. This filter $H_f(f)$ defines a mapping in the frequency domain between the white noise input vector $w(t)$ and the colored noise output vector $r(t)$:

$$R(f) = H_f(f)W(f)$$

where R(f) and W(f) are the Fourier transforms (FTs) of $r(t)$ and $w(t)$. White noise is defined by its flat PSD of $W(f) = 1$. If the filter $H(f)$ is applied to white noise, the PSD of the colored noise is thus simply

$$S_{yy}(f) = |R(f)|^2 = |H_f(f)|^2$$

In order to shape colored noise to a given PSD, the required filter is hence constrained by :

$$|H_f(f)|^2 = S_{yy}(f)$$

In practice, the filter is typically applied by fitting a rational transfer function on $S_{yy}(f)$ which is then simulated as an additional linear block in the model.

Two methods can be used in order to define an adequate noise-shape filter:

Transfer function design: In a transfer function written in the zero-pole form, every zero z_k and every pole p_l is either a real number or two zeros (or poles) are each a complex conjugate pair. A necessary condition to express $H_f(s)$ in a state space representation is that H(s) is proper, i.e., the number of poles n_p is greater than or equal to the number of zeros n_z. If the real part of all poles and zeros is negative, a transfer function is called minimum phase. In addition to the cited constraint, $H_f(s)$ must be proper and minimum phase, in order to be realizable by a state space system. Finally, the approximation of a given PSD with a rational transfer function can be done placing poles and zeros in the right bandwidth

Least-square design: Because a suitable transfer function $H_f(s)$ cannot be analytically computed from a given PSD in general, a least squares fit is performed. Simply, one can build a system of minimization of the argument which is function of the given PSD and the required filter. The coefficients a_k and b_l of the filter are chosen as decision variables because they are real numbers and independent from each other. In order to ensure that the filter is proper, $n_z = n_p - 1$ is chosen. An optimization should be performed. Finally, the minimum phase requirement is fulfilled by a subordinate step. To that end, the zeros z_k and poles p_l of the optimal solution are computed. Afterwards, the real part of every pole/zero is mirrored into the left half plane.

Simulink$^{©}$ contains a continuous band-limited white noise block and a random noise generator which ask noise power, sample time and seed. Actually, noise power and sample time are correlated and a trade off between these quantities must be done in order to implement a white noise with unity average power spectral density while running the needed simulation. The choice of the sampling time must be discussed. A short noise sampling time creates a white noise with a high limiting frequency (theorically a white noise has no limiting freq but in Simulink$^{©}$, of course, it has a limited bandwidth). As a consequence of the small sample time, the computational cost of the simulation will increase making difficult to reach big time of simulation, which is for the LISA case mandatory. The slow behavior of the GW constraints the all simulation. As a matter of fact, one can proceed to a down sampling of the RPSD [9].

Moreover, the verification of frequency-domain requirements has been made exploiting the Welch approximation. The Average periodogram method wants to estimate a generic periodogram from some data $x[n]$ with $n = 0,1,..,L-1$ by taking the DFTF of the sequence. In general we can say that if $L \rightarrow \infty$ we have that the energy of the estimated periodogram tends to the real one, and so the variance of the estimated periodogram behaves like square of the target SD. The Welch approximation performs a multiple averaging of periodograms in order to reduce the variance error of the estimation. Is proven that if we average k independent variables we can reduce the variance by a factor of $1/k$. Taking a data sequence $x[m]$ with $m = 0,1,...Q-1$ and dividing it into segments of length L, we can operate the Welch estimation. Every subsegment, called window, is used to compute a periodogram and the segments can be overlapped. Moreover the single periodogram can be obtain with different characteristics, depending by the type of data set. However, we can say that with a large number of collected samples we can obtain a good variance reduction and a good bias reduction by overlapping the data. Moreover, the resolution and the dynamic range performances are related with the choice of the window, [57] [58] [59].

Bibliography

[1] ESA, "The Gravitational Universe", 03 October 2017, `http://sci.esa.int/jump.cfm?oid=58543`.

[2] Einstein, A *Näherungsweise Integration der Feldgleichungen der Gravitation* Sitzungsberichte der Königlich Preussischen Akademie der Wissenschaften Berlin, (June 1916), part 1: 688–696.

[3] Einstein, A., *Über Gravitationswellen*, Sitzungsberichte der Königlich Preussischen Akademie der Wissenschaften Berlin, (1918), part 1: 154–167.

[4] Abbott, B. P., *et. al., Observation of Gravitational Waves from a Binary Black Hole Merger*, LIGO Scientific Collaboration and Virgo Collaboration, PRL 116, 061102 (2016).

[5] Heinzel, G., *et. al., Interferometry for the LISA Technology Package aboard SMART-2* Class. QuantumGrav. 20 S153–61, 2003.

[6] Schleicher, A., *et al., In-Orbit Performance of the LISA Pathfinder Drag Free and Attitude Control System*, Proceedings of the 10th International ESA Conference on Guidance Navigation & Control Systems, 29 May – 2 June 2017, Salzburg, Austria, 2017

[7] Armano, M., *et al., Sub-Femto-g Free Fall for Space-Based Gravitational Wave Observatories: LISA Pathfinder Results* American Physical Society, 116, 231101 (2016)

[8] ESA, *LISA CDF Final Presentation*

[9] Gath, F. P., *et al., Drag free and attitude control system design for the LISA science mode* AIAA Guid., Nav. and Control Conf. and Exhibit (Hilton Head, South Carolina, 20-23 August 2007) (AIAA) p 2007-6731.

[10] Cirillo, F., *Controller design for the acquisition phase of the LISA mission using a Kalman filter*, Uni Pisa (2007) etd-06202007-101808

[11] P. Amaro-Seoane, et al, *LISA Laser Interferometer Space Antenna: a proposal in response to ESA call for L3 mission concepts*,2017.

[12] ESA, *Statement of Work: Appendix 1*, ESA ITT 1-9100/17/NL/CRS, 2017.

[13] Appendix 1 to ESA ITT 1-9100/17/NL/CRS

[14] Jennrich, O., *LISA technology and instrumentation* Class. Quantum Grav. arXiv:0906.2901v1 [astro-ph.IM] 16 Jun 2009

[15] Ke-Xun Sun *et al., LISA Gravitational Reference Sensors* 2007 J. Phys.: Conf. Ser. 60 272

[16] John W. Conklin, *Drift mode accelerometry for spaceborne gravity measurements* 2 July 2015, Springer-Verlag Berlin Heidelberg 2015

[17] Allen, G. *et al., A Gravitational reference sensor for advanced drag-free satellites* Poster presented at 17th IFAC Symposium on Automatic Control in Aerospace, June 25-29, 2007, Toulouse, France

[18] Yanzheng Bai, *et al., Research and Development of Electrostatic Accelerometers for Space Science Missions at HUST.* 23 August 2017, MDPI Journal

[19] Dolesi, R.,*et al., Gravitational sensor for LISA and its technology demonstration mission* Classical and Quantum Gravity. 20. S99. 10.1088/0264-9381/20/10/312.

[20] Cavalleri, A., *et al., Progress in the development of a position sensor for LISA drag-free control* Classical and Quantum Gravity, 2001, 18 4133

[21] Armano, M.,*et al., Charge-induced force-noise on free-falling test masses: results from LISA Pathfinder* arXiv:1702.04633v1 [astro-ph.IM] 15 Feb 2017

[22] John W Conklin *et al., Mass properties measurement for drag-free test masses* 2009 J. Phys.: Conf. Ser. 154 012019.

[23] Montemurro, F. *et al., Control Design of the Test Mass Release Mode for the LISA Pathfinder Mission* , AIP Conf. Proc, 873, 583 (2006)

[24] Zanoni, C., *et al.,Summary of the results of the LISA-Pathfinder Test Mass release* 2015 J. Phys.: Conf. Ser. 610 012022

[25] Armano, M., *et al., The LISA Path nder Mission* Journal of Physics: Conference Series 610 (2015) 012005

[26] Grynagrier, A., *et al., Identification of Dynamic Parameters for a One-Axis Drag-Free Gradiometer* IEEE Transactions on Aerospace and Electronic Systems VOL. 49, NO. 1 JANUARY 2013

[27] Nappo, F., *et al., Experience and design drivers for the Inertial Sensor on the LISA Pathfinder mission* AIP Conf. Proc., 873, 539 (2006)

[28] Vitale, S., *et al., Space-borne Gravitational Wave Observatories* arXiv:1404.3136v1 [gr-qc] 11 Apr 2014

[29] Carmain, A., *et al., Space Technology 7 Disturbance Reduction System Precision Control Flight Validation* 0-7803-9546-8/06/20.00 2006 IEEE

[30] Gath, P. F.,*et al., LISA Mission and System architectures and performances* 2009 J. Phys.: Conf. Ser. 154 012013

[31] Fichter, W., *et al., Drag-Free Control Design with Cubic Test Masses* Astrophysics and Space Science Library, vol 349. Springer, Berlin, Heidelber

[32] Lennart Wissel and LPF collaboration *LISA Pathfinder: Understanding DWS noise performance for the LISA mission* 2017 J. Phys.: Conf. Ser. 840 012044

[33] Shaddock, D. A., An overview of the Laser Intererometer Space Antenna Publ.Astron.Soc.Austral.26:128-132,2009

[34] Giulicchi, L., *et al., Attitude and orbit control systems for the LISA Pathfinder mission* Aerospace Science and Technology 24 (2013) 283–294

[35] Molina, M., *et al., Leonardo – Finmeccanica Cold Gas Micropropulsion in-orbit performances: LISA Pathfinder and Microscope* IAC-16-C4,6,2,x35412

[36] Morris, G. E., *et al., Design of a Cold-Gas Micropropulsion system for LISA Pathfinder* JPC July 14-17, 2013.

[37] Ferraioli, L., *et al., Quantitative Analysis of LISA Path
nder Test Mass Noise* arXiv:1111.3320v1 [gr-qc] 14 Nov 2011

[38] Warren, C., *Managing disturbance sources on LISA Pathfinder* AIP J. 873 682-688 (2006)

[39] Piper, G. E. *et al., On the Control Design of the Disturbance Reduction System for the Lisa Mission* AIAA Guidance, Navigation, and Control Conference and Exhibit.

[40] Hyde, T. T., *et al., Precision Pointing for the Laser interferometry space antenna mission,*Guidance, Navigation and Control Division, Greenbelt, MD 20771 AAS 03-066

[41] Antonucci, F., *et al., From laboratory experiments to LISA Pathfinder: achieving LISA geodesic motion.* (2011)

[42] Giusteri, R. and on behalf of the LPF collaboration *The free-fall mode experiment on LISA Pathfinder: first results* J. Phys.: Conf. Ser. 840 012005 (2017)

[43] Merkovitz S. M., *et al., Self-gravity modelling for LISA* Class. Quantum Grav. 22 S395-S402 (2005)

[44] LISA Pathfinder Collaboration *LISA Pathfinder closed-loop analysis: a model breakdown of the in-loop observables* 2017 J. Phys.: Conf. Ser. 840 012038

[45] LISA Pathfinder Collaboration, *LISA Pathfinder Platform Stability and Drag-free Performance*

[46] Dispense del Corso *Spacecraft Attitude Dynamics and Control*

[47] Canuto, E., *et al., Spacecraft Dynamics and Control: The Embedded Model Approach.* Butterworth-Heinemann (Elsevier), 2018.

[48] Fichter, W., *et al., Closed Loop Performance and Limitations of the LISA Pathfinder Drag-Free Control System*, AIAA Guidance, Navigation and Control Conference and Exhibit, Guidance, Navigation, and Control and Co-located Conference.

[49] Fichter, W., *et al., LISA Pathfinder Drag-Free Control and System Implications*, Classical and Quantum Gravity, 22, 10, s139-s148, (2005)

[50] Fichter, W., *et al.: Control tasks and functional architecture of the LISA Pathfinder drag-free system*, In: Danesy, D. (ed.) Proceedings of the 6th ESA Conference on Guidance, Navigation, and Control Systems, vol. SP-606, ESA Publications Division (2006).

[51] Gath, P., *et al. Drag Free and Attitude Control System Design for the LISA Pathfinder Mission*, AIAA Guidance, Navigation, and Control Conference and Exhibit, Guidance, Navigation, and Control and Co-located Conferences, ()

[52] Armano, M., *et al., Free-flight experiments in LISA Pathfinder* 2015 J. Phys.: Conf. Ser. 610 012006

[53] Wu S-F., Fertin D. *QFT based drag-free and attitude controller design/tuning* ESA Conference on Guidance, Navigation and Control Systems, Loutraki, Greece, 17-20 October 2005 (ESA SP-606, January 2006)

[54] Wu S-F., Fertin D. *Spacecraft drag-free attitude control system design with Quantitative Feedback Theory* Acta Astronautica 62 (2008) 668 – 682

[55] Saage, R., *et al., Closed-Loop Specifications for Spacecraft Control Under Micro-propulsion Constraints* Journal of Guidance, Control, and DynamicsVol. 35, No. 5, September–October 2012

[56] Armano, M., *et al., The LISA Pathfi nder Mission* Journal of Physics: Conference Series 610 (2015) 012005

[57] Tröbs, M. and Heinzel, G. *Improved spectrum estimation from digitized time series on a logarithmic frequency axis. Measurement, Vol. 39, No. 2, pp. 120–129, 2006.*

[58] Carrettoni, M. and Cremonesi, O. Generation of Noise Time Series with arbitrary Power Spectrum arXiv:1006.3289

[59] Andreas Klöckner, Andreas Knoblach, and Andreas Heckmann. *How to shape noise spectra for continuous system simulation. 11th International Modelica Conference, no 118 in Linköping Electronic Conference Proceedings, pages 411–418, Versailles, France.*